Development and Implementation of Water-Leaf Targets for Laser-Ion Acceleration at CALA

—First Demonstration of a 20 MeV, 0.1 Hz Proton Source

Lianren He

München 2025

Development and Implementation of Water-Leaf Targets for Laser-Ion Acceleration at CALA

—First Demonstration of a 20 MeV, 0.1 Hz Proton Source

DISSERTATION

an der Fakultät für Physik der

Ludwig-Maximilians-Universität München

vorgelegt von

Lianren He

geboren in Liaoning, China

München, den 14. January 2025

Erstgutachter: Prof. Dr. Jörg Schreiber
Zweitgutachter: Prof. Dr. Jianhui Bin
Tag der mündlichen Prüfung: 25. March 2025

Zusammenfassung

Die lasergetriebene Ionenbeschleunigung hat aufgrund ihres Potenzials, kompakte Protonenquellen mit hoher Flussdichte für vielfältige wissenschaftliche und industrielle Anwendungen bereitzustellen, erhebliche Aufmerksamkeit erlangt. Herausforderungen bei der Erzielung eines langfristigen, stabilen, reproduzierbaren und hochfrequenten Protonenstrahls haben jedoch den Übergang von Machbarkeitsstudien zu praktischen Anwendungen eingeschränkt. Diese Dissertation adressiert diese Herausforderungen durch die Entwicklung und experimentelle Demonstration eines Wasserfilm-Targets, das in die Laser-Ionen-Beschleunigungsstation des Center for Advanced Laser Applications (CALA), die sogenannte LION-Kammer, integriert wurde.

Das Wasserfilm-Target-System zeigte einen stabilen Betrieb unter Vakuumbedingungen ($1,0 \times 10^{-4}$ bis $1,0 \times 10^{-3}$ mbar) über Zeiträume von mehr als 10 Stunden. Die präzise Positionskontrolle des Systems ermöglichte eine systematische Optimierung wichtiger experimenteller Parameter, darunter axiale Bewegungen entlang des Laserstrahls, vertikale Anpassungen zur Variation der Targetdicke (im Bereich von 2 µm bis 20 µm) sowie Korrekturen von Rotationsfehlausrichtungen zwischen den einzelnen Laserschüssen.

Experimentelle Untersuchungen mit dem ATLAS-3000-Lasersystem, das 27-fs-Pulse mit Energien von bis zu 10 J (entsprechend einer Spitzenleistung von 300 TW) liefert, zeigten die Effizienz des Wasserfilms für die Protonenbeschleunigung. Es wurden maximale Protonenenergien von bis zu 30 MeV erreicht, wobei Skalierungsgesetze darauf hinweisen, dass Protonenenergien von über 60 MeV möglich sind, wenn die volle Laserenergie von 60 J auf das Ziel fokussiert wird.

Ein bedeutender Erfolg war die reproduzierbare Erzeugung hochfrequenter Protonenbündel über 400 Schüsse mit einer Wiederholfrequenz von 0,1 Hz. Die Experimente zeigten einen stabilen Betrieb mit Protonenenergien von bis zu 30 MeV (im Mittel 22 MeV) bei 10 J Laserenergie auf dem Target, was die Bereitschaft des Systems für praktische Anwendungen unterstreicht.

Darüber hinaus untersuchte die Dissertation den Einfluss der Laserpolarisation auf die Protonenbeschleunigung. Modulationen im Protonenspektrum wurden vor allem mit zirkluarer Polarisation beobachtet und sind vermutlich auf die Präsenz von Ionen unterschiedlicher Ladungszustände während der Strahlungsdruck-dominierten Phase

zurckzuführen. Die Ergebnisse liefern neue Einblicke in die komplexen Dynamiken der lasergetriebenen Ionenbeschleunigung und eröffnen Wege für weitere Untersuchungen zur Manipulation und Optimierung der Ionen-Verteilungen.

Abstract

Laser-driven ion acceleration has garnered significant attention for its potential to generate compact, high-flux proton sources suitable for diverse scientific and industrial applications. However, challenges in achieving long-term, stable, reproducible, and high-repetition-rate proton bunches have limited its transition from proof-of-principle demonstrations to practical applications. This thesis addresses these challenges through the development and experimental demonstration of water-leaf targets, which has been integrated into the laser-ion acceleration end station of the Center for Advanced Laser Applications (CALA), known as the LION chamber.

The water-leaf target system demonstrated sustained operation in vacuum conditions (1.0×10^{-4} to 1.0×10^{-3} mbar) for durations exceeding 10 hours. The system's precise positional control enabled systematic optimization of key experimental parameters, including axial movements along the laser beam, vertical adjustments for target thickness variation (ranging from 2 µm to 20 µm), and corrections for rotational misalignments between shots.

Experimental investigations conducted with the ATLAS-3000 laser system, delivering 27 fs pulses with energies of up to 10 J (corresponding to 300 TW peak power), revealed the water-leaf target's capability for efficient proton acceleration. The results demonstrated maximum proton energies of up to 30 MeV, with scaling laws predicting proton energies exceeding 60 MeV using the full 60 J ATLAS-3000 laser energy on target, assuming consistent target parameters.

A significant achievement was the reproducible, high-repetition-rate generation of proton bunches, recorded over 400 shots at 0.1 Hz. The experiments demonstrated stable operation, producing proton energies up to 30 MeV (average 22 MeV) at 10 J laser energy on target—highlighting the system's stability and repeatability for practical applications.

Furthermore, the thesis explored the influence of laser pulse polarization on proton acceleration. Modulations in proton spectra were observed repeatedly and more consistently with circular polarization. This hints at the presence of ions with different charge states during radiation-pressure-assisted acceleration. These findings provide novel insights into the complex dynamics of laser-driven ion acceleration and open pathways for further investigation into spectrum manipulation and optimization.

Contents

List of Figures

List of Tables

Abbreviations

ADK Ammosov-Delone-Kraino

ADU Analog-to-Digital Units

ATI Above-Threshold Ionization

ATLAS Advanced Titanium: sapphire LASer

BOA Break-Out Afterburner

BS Beam Splitter

BSI Barrier Suppression Ionization

CALA Centre for Advanced Laser Applications

CE Coulomb Explosion

CMOS Complementary Metal-Oxide-Semiconductor

CP Circular Polarization

CPA Chirped Pulse Amplification

CSA Collisionless Shock Acceleration

CV Coefficient of Variation

CW Continuous Wave

EMP ElectroMagnetic Pulse

FROG Frequency Resolved Optical Gating

FWHM Full Width at Half-Maximum

HB Hole Boring

HDR High Dynamic Range

HHG High Harmonic Generation

HPLC High Performance Liquid Chromatography

IP image plate

IQR InterQuartile Range

KLM Kerr Lens Mode-locking

LBD Laser-Beamline Delivery

LDR Low Dynamic Range

LG Laguerre Gaussian

LION Laser-driven ION

LP Linear Polarization

LS Light Sail

MPI MultiPhoton Ionization

ND Neutral Density

OAP Off-Axis Parabolic

OPCPA Optical Parametri Chirped Pulse Amplification

OPE Oxygen Penetration Energy

PIC Particle-In-Cell

PMQ Permanent Magnet Quadrupole

PPE Proton Penetration Energy

PPT Perelomov-Popov-Terent'ev

pv Pixel Value

PW PetaWatt

QED Quantum ElectroDynamics

QIS Quantitative Ion Spectrometry

RIT Relativistic Induced Transparency

RPA Radiation Pressure Acceleration

SDF Signal Distribution Function

SRSI Self-Referenced Spectral Interferometry

TCC Target-Chamber-Center

TI Tunnel Ionization

TNSA Target Normal Sheath Acceleration

TPS Thomson Parabola Spectrometer

TW TeraWatt

WASP Wide Angle SPectrometer

WLT Water Leaf Target

WP Wave Plate

ZS Zentrale Steuerung

Chapter 1

Introduction

1.1 History and current status of laser-driven ion acceleration

Laser-driven ion acceleration has emerged as a promising field at the intersection of high-power laser physics and plasma physics, offering the potential to create compact, high-energy particle sources with unique characteristics. The concept of plasma-based particle acceleration was first proposed by Veksler in the 1950s [1]. The experimental journey of laser-driven ion acceleration began in the 1960s with the advent of high-power lasers [2].

During the 1970s, these plasma expansion studies were primarily motivated by investigations into laser-plasma interactions and energetic ion energy loss for inertial confinement fusion [3]. Early experiments in the 1980s, utilizing relatively low laser intensities (below $\sim 10^{15}$ W/cm^2) and long pulse duration in the nanosecond or picosecond regime, produced ions characterized by large emittance angles and broadband energy spectra, typically with kinetic energies on the order of ~ 100 keV/u [4,5]. These initial studies laid the groundwork for subsequent advancements in the field of laser-driven ion acceleration.

The field experienced a revolutionary leap forward in the mid-1980s with the development of chirped pulse amplification (CPA) by Strickland and Mourou [6]. This groundbreaking technique enabled the generation of ultra-short, high-intensity laser pulses, dramatically expanding the possibilities for laser-plasma interactions. The CPA breakthrough was further complemented by two critical advancements in laser technology: the invention of the Kerr lens mode-locking (KLM) technique [7, 8] and the discovery of titanium-doped sapphire (Ti:sapphire) as a laser medium [9].

The synergy of these innovations paved the way for multi-terawatt or even multi-petawatt table-top laser systems and have made it possible to achieve laser intensities exceeding 10^{21} W/cm^2 in global development work [10, 11], with the potential to reach

extreme intensities beyond 10^{23} W/cm^2 in the future [12, 13], as shown in Fig. 1.1, opening up a new era in the study of relativistic laser-plasma interactions. The term "relativistic" marks the fact that electrons in the laser focus are accelerated close to the velocity of light within one laser period. This happens for light intensities I_L exceeding 10^{18} W/cm^2 for common laser wavelengths λ_l of about 1 µm. The corresponding intensity for the relativistic motion of protons in the laser field exceeds 5×10^{24} W/cm^2.

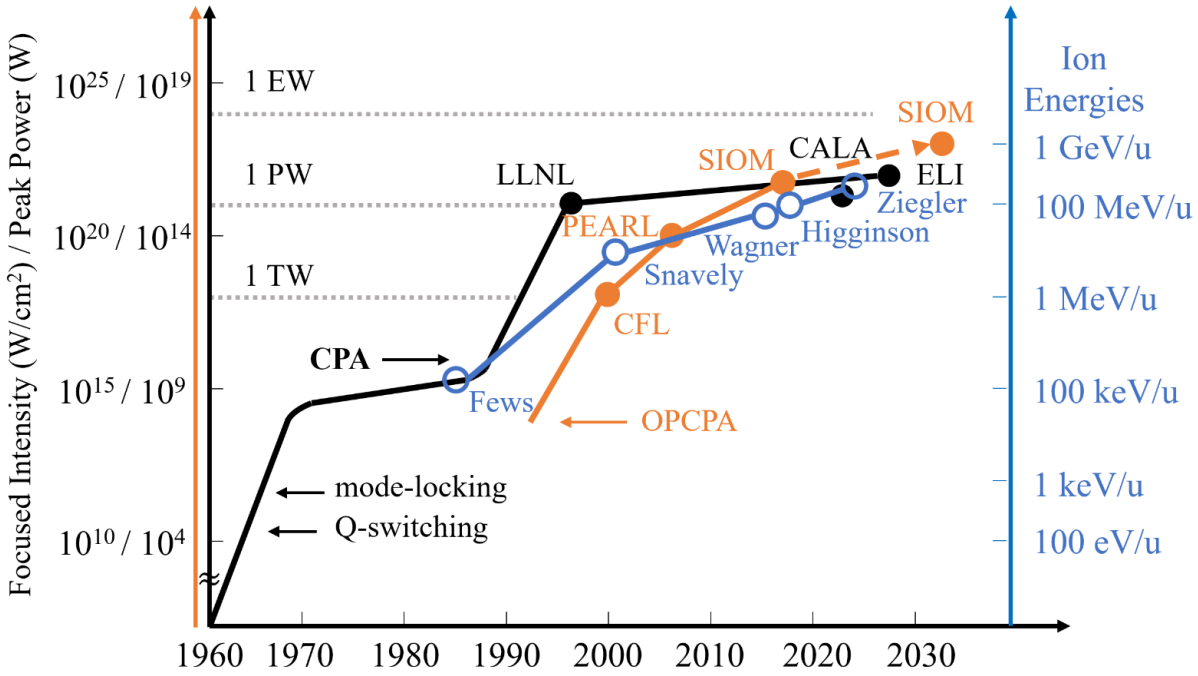

Figure 1.1: History of high intensity/power laser pulses. The black solid line represents the development of laser-focused intensity or peak power based on CPA, while the orange solid line represents Optical Parametric CPA (OPCPA) [14], both corresponding to the left axis. Assuming a 100 μm^2 focal spot size, there is a six-order magnitude difference between laser-focused intensity and peak power. The blue solid line depicts experimentally achieved maximum ion energy versus year [15–19] (right axis, nonlinear scale). The figure is adapted from [20].

The advent of relativistic laser intensities drastically transformed the landscape of laser-driven ion acceleration. In 1994, Fews et al. demonstrated ion emission exceeding 1 MeV using a marginally relativistic laser system (2×10^{18} W/cm^2) [15], marking a significant advancement in the field. The early 2000s witnessed several research groups achieving proton beams with energies in the tens of MeV range and conversion efficiencies up to a few percent [16, 21–23]. A notable milestone was reached when highly energetic proton beams up to 58 MeV were observed by irradiating solid-density foils with the first

petawatt laser [16]. This record was subsequently surpassed in the 2010s, with maximum proton energies approaching 100 MeV experimentally achieved [17, 18].

Laser-driven ion acceleration currently stands at a critical juncture in its development. Recent experiments have demonstrated remarkable progress, achieving maximum proton energies of up to 150 MeV through the irradiation of solid-density plastic foil targets with ultrashort laser pulses from a repetitive petawatt laser system [19]. These advancements have been realized through a cascade of different acceleration mechanisms. Laser-driven ion beams exhibit a unique set of characteristics that distinguish them from those produced by conventional accelerators. These properties include a small source size and ultra-low emittance [24], ultra-short pulse durations on the order of picoseconds [25], high peak currents, and high particle energies. Motivated by these exceptional properties, a robust research field has evolved, focusing on both theoretical and experimental investigations of laser-driven ion acceleration [26–29].

This novel type of particle acceleration broadens the application spectrum of conventional sources in science, technology, energy, and medicine [28]. Such applications can include neutron sources [30, 31], material science [32–34], inertial fusion energy [35, 36], and radiation biology [37–42]. Of particular interest is the potential exploitation of the FLASH effect, which involves delivering radiation doses over extremely short time scales [43]. This approach could offer significant advantages in radiation therapy but requires more investigation. Recent oncological studies using laser-accelerated protons on mice samples have marked a new milestone in the field [40], demonstrating the feasibility of using laser-driven ion sources for radiation therapy. However, it is important to note that while these advancements are promising, the commercial application of laser-driven ion acceleration in clinical settings is likely still several years away.

Despite significant progress in laser-driven ion acceleration, numerous challenges persist, necessitating further research and development. Key areas requiring investigation include improving beam quality, enhancing shot-to-shot stability, scaling to higher energies and efficiencies, and transitioning from single-shot experiments to high-repetition-rate operation [44, 45]. The advent of petawatt (PW) class lasers capable of operating at high repetition rates has opened new avenues for laser-driven proton acceleration. These systems can deliver laser pulses with peak power beyond 1 PW, with pulse durations in the femtosecond range, at repetition rates of 1 Hz or higher [10]. Building upon foundational developments, recent research has focused on addressing these critical challenges, particularly the need for high-repetition-rate target solutions compatible with advanced PW laser systems [46, 47]. This shift towards high-repetition-rate operation is crucial

for transitioning laser-driven proton acceleration from proof-of-principle experiments to practical applications. However, the full potential of these laser systems can only be realized with the development of suitable target technologies that can keep pace with the laser repetition rate while maintaining consistent and optimal conditions for proton acceleration.

To achieve these goals, different strategies have regained interest over the past years, for example, liquid crystal films [48], pre-positioned foils [49], renewable tape drives [50], or cryogenic jets [51, 52]. Liquid jets [53] and in particular, liquid leaf targets, which can support high-repetition-rate operation while maintaining optimal conditions for ion acceleration, are meanwhile broadly tested and introduced in many systems [54–60]. The versatility and effectiveness of liquid targets have been demonstrated across a wide range of experimental setups, from tabletop systems to large-scale facilities. The integration of these advanced target technologies with state-of-the-art laser systems is paving the way for a new generation of laser-driven ion accelerators. These developments hold promise for bridging the gap between proof-of-principle experiments and practical applications in various fields, including medical physics, materials science, and fundamental research.

1.2 Choice of water-leaf target

Among the diverse array of high-repetition-rate targets under investigation, water-leaf targets have emerged as a particularly promising candidate due to their unique combination of advantageous properties. These targets offer several distinct benefits that make them well-suited for advanced laser-driven ion acceleration experiments:

1. **Continuous operation:** The self-replenishing nature of water-leaf targets facilitates uninterrupted operation at high repetition rates, aligning well with the capabilities of advanced petawatt laser systems [61].

2. **Debris mitigation:** Unlike solid targets, water-leaf targets generate less debris during laser interaction, significantly reducing the risk of damage to sensitive optical components and maintaining a cleaner experimental environment [62].

3. **Thickness control:** The fluid nature of water-leaf targets allows for precise and dynamic control over target thickness, enabling the exploration of a wide range of experimental parameters [55].

4. **High hydrogen content:** Water provides an abundant source of protons, potentially leading to more efficient acceleration and higher beam currents [63].

5. **Cost-effectiveness:** Water-leaf targets can be produced and maintained at a fraction of the cost of traditional solid foil targets, making them economically viable for large-scale, high-repetition-rate experiments [51].

1.3 Thesis overview

This thesis aims to advance the field of laser-driven ion acceleration by developing and implementing a high-repetition-rate target solution compatible with advanced PW laser systems. The primary objective is to generate reproducible, high-repetition-rate proton bunches, addressing a critical need in the transition from proof-of-principle experiments to practical applications. A key component of this research is the development and optimization of a prototype high-repetition-rate water-leaf target system, specifically designed for laser-driven ion acceleration experiments. By integrating advanced laser techniques with water-leaf targets, this work demonstrates the feasibility of a compact proton source utilizing a PW laser system. This approach shows promising potential for diverse applications of ultrashort laser-driven ion bunches. Furthermore, the underlying physics governing laser-driven ion sources is of fundamental importance to this research. Consequently, experimental campaigns were conducted to investigate these physical processes, forming a major focus of this thesis. These investigations not only contribute to the understanding of laser-plasma interactions but also provide valuable insights for future applications. The structure of this thesis is as follows:

Chapter 2 presents the key theoretical concepts essential for understanding laser-driven ion acceleration. It begins with an introduction to laser field basics and then examines single electron dynamics in relativistic laser fields. The chapter proceeds to discuss ionization processes and laser-plasma interactions, which are fundamental to the formation and behavior of plasmas in intense laser fields. Finally, it provides an overview of the main mechanisms of laser-driven ion acceleration.

Chapter 3 examines liquid leaf targets, focusing on their development, basic principles, and current challenges in laser-driven ion acceleration experiments. It begins with a historical overview, tracing the evolution of liquid leaf targets from industrial applications to their use in laser-plasma physics. The chapter then explores the fundamental physics of water-leaf targets. Methods or setups for generating water-leaf targets are described, along with techniques for measuring their thickness, which is crucial for experimental

control. Finally, it addresses current challenges in implementing and operating water-leaf targets, such as evaporation and freezing issues, and presents ongoing research efforts to overcome these obstacles.

Chapter 4 outlines the experimental methods and apparatus utilized in this study. It begins with a description of the ATLAS-3000 high-power laser system, followed by a detailed account of the Laser-driven ION acceleration (LION) experimental chamber. Additionally, ion diagnostics used in the experiments are discussed.

Chapter 5 reports a systematic investigation of laser-driven proton acceleration using water-leaf targets. The effects of various experimental parameters on proton bunches characteristics are analyzed in detail. This includes a laser energy scan to establish the relationship between laser energy and maximum proton energy, along with focus/defocus scans to optimize laser-target interaction. A target thickness scan is performed to identify the optimal parameters for efficient acceleration. Additionally, shot-to-shot variations in proton bunch characteristics are assessed to evaluate process stability and reproducibility. The results have been submitted for publication. The chapter also explores the influence of laser pulse polarization on proton acceleration, comparing the outcomes of linearly and circularly polarized pulses, with these results currently in preparation for publication.

Chapter 6 discusses the experimental results. It outlines strategies for optimal proton acceleration, discusses current limitations and proposes improvements. Using derived scaling laws, an extrapolation suggests the potential for generating proton bunches exceeding 60 MeV. The chapter examines possible causes of shot-to-shot variations, providing insights into laser-plasma interaction dynamics. Finally, it explores methods for spectrum manipulation and mono-energetic ion bunch generation.

Chapter 7 summarizes the key findings of this work and outlines potential directions for future research.

Chapter 2

Theoretical Background

This chapter provides an overview of laser-plasma interaction theory, focusing on concepts essential to understanding the experimental work presented in this thesis. The content of this chapter draws primarily from the seminal works of P. Gibbon, A. Macchi, and W. Kruer [64–66].

2.1 Electromagnetic wave

Laser light is fundamentally an electromagnetic wave that can be fully described within the framework of Maxwell's equations [67]:

$$\textbf{Gauss's law: } \nabla \cdot \vec{E} = \frac{\rho}{\varepsilon_0}, \tag{2.1}$$

$$\textbf{Gauss's law for magnetism: } \nabla \cdot \vec{B} = 0, \tag{2.2}$$

$$\textbf{Faraday's law: } \nabla \times \vec{E} = -\frac{\partial \vec{B}}{\partial t}, \tag{2.3}$$

$$\textbf{Ampere - Maxwell law: } \nabla \times \vec{B} = \mu_0 \vec{j} + \mu_0 \varepsilon_0 \frac{\partial \vec{E}}{\partial t}, \tag{2.4}$$

where $\vec{E}$ and $\vec{B}$ are the electric and magnetic fields, respectively. ρ is the charge density, $\vec{j}$ denotes the current density, and ε_0 and μ_0 are the permittivity and the permeability of the vacuum, respectively. It is important to note that all units in this thesis are given in the SI system unless otherwise specified.

In a vacuum, where there are no charges ($\rho = 0$) and no currents ($\vec{j} = 0$), Maxwell's equations can be simplified. By taking the curl ($\nabla\times$) of the curl equations, and applying

the curl of the curl identity, the wave equations are derived:

$$\begin{aligned} \frac{1}{c^2}\frac{\partial^2 \vec{E}}{\partial t^2} - \nabla^2 \vec{E} = 0, \\ \frac{1}{c^2}\frac{\partial^2 \vec{B}}{\partial t^2} - \nabla^2 \vec{B} = 0. \end{aligned} \tag{2.5}$$

Equation 2.5 describes the propagation of an electromagnetic wave with the speed of light, defined as $c = 1/\sqrt{\mu_0 \varepsilon_0}$. The most fundamental solution to the wave equation is given by a plane wave propagating along the z direction:

$$\begin{aligned} \vec{E}(z,t) = \vec{E}_0 \cos(k_0 z - \omega_0 t + \phi_0), \\ \vec{B}(z,t) = \vec{B}_0 \cos(k_0 z - \omega_0 t + \phi_0), \end{aligned} \tag{2.6}$$

where k_0 is the wavenumber, ω_0 is the angular frequency, with a relationship of $k_0 = \omega_0/c$, and ϕ_0 is the initial phase. Faraday's law, $\nabla \times \vec{E} = -\partial \vec{B}/\partial t$, indicates that $\vec{E}$ and $\vec{B}$ are perpendicular, and have the relationship:

$$E_0 = cB_0, \tag{2.7}$$

where $E_0 = |\vec{E}_0|$ and $B_0 = |\vec{B}_0|$ are the field amplitudes for linear polarized waves. Such waves have a directional energy flux, described by the Poynting vector, defined as:

$$\vec{S} = \frac{1}{\mu_0} \vec{E} \times \vec{B}. \tag{2.8}$$

The intensity of the laser light I_0 is defined as the time-averaged magnitude of the Poynting vector:

$$I_0 = < \vec{S} > = \frac{\varepsilon_0 c {E_0}^2}{2}. \tag{2.9}$$

As electromagnetic waves also carry momentum, the radiation pressure can be calculated by considering the transfer of this momentum to a surface. For a plane wave incident on a surface, the potential radiation pressure P_{rad} is given by:

$$P_{rad} = \frac{< \vec{S} >}{c} = \frac{I_0}{c}. \tag{2.10}$$

Note that for a perfectly reflecting surface, the momentum transfer is twice the initial momentum of the electromagnetic wave, as the wave reverses direction upon reflection. This results in a radiation pressure of $P_{rad} = 2I_0/c$ on a perfect mirror.

In the following section, the dimensionless laser amplitude $a_0 = eE_0/m_e c\omega_0$ will be introduced. The value $a_0 = 1$ defines the relativistic threshold. The corresponding amplitudes of the electric field and magnetic field are given by:

$$\begin{aligned} E_0\ [\mathrm{V/m}] &= \frac{3.2 \times 10^{12}}{\lambda\,[\mu m]} a_0, \\ B_0\ [\mathrm{T}] &= \frac{1.07 \times 10^{4}}{\lambda\,[\mu m]} a_0. \end{aligned} \tag{2.11}$$

The corresponding laser intensity can be written in terms of a_0 as:

$$I_0 = \zeta \frac{1.37 \times 10^{18} W/cm^2}{\lambda^2[\mu m^2]} a_0^2, \tag{2.12}$$

where λ is the laser wavelength in units of μ m, ζ is the polarization correction coefficient. $\zeta = 1$ for linear polarization (LP) and $\zeta = 2$ for circular polarization (CP).

Plane waves are often used to model laser pulse propagation and its effects in plasmas. However, in many realistic scenarios, this approach is often an approximation that neglects spatial and temporal dependencies of amplitudes. The intensity distribution in the focal plane, commonly referred to as the laser focus, is a crucial element in laser-driven ion acceleration. Although the spatial distribution of many flat-top laser systems is more accurately described by a sinc function, a Gaussian distribution is widely used for approximations due to its mathematical simplicity. The peak intensity of the laser pulse can be estimated by assuming a perfect Gaussian profile in both space and time:

$$I_0 = \frac{0.83 E_L}{t_{FWHM} \cdot d_{FWHM}^2} \tag{2.13}$$

where E_L, t_{FWHM}, and d_{FWHM} are the energy, the full-width half-maximum (FWHM) duration, and the FWHM focal spot size of the laser pulse intensity distribution, respectively. It is noteworthy that this estimation tends to overestimate the peak intensity of the actual laser beam profile by a factor of 1.5 [68] due to non-gaussian distribution and the detection limit inherent in the low-dynamic-range images of focus profiles.

2.2 Single electron motion in electromagnetic field

To establish a foundational understanding of laser-matter interactions, it is helpful to begin by considering the motion of a single free electron in an electromagnetic wave

propagating through a vacuum. In accordance with the conventional treatment of Maxwell's equations, self-radiation is typically neglected in electromagnetic analyses. This approach focuses solely on its response to the electromagnetic field, disregarding the radiation emitted due to the electron's acceleration. Then the dynamics of the electron's motion are described by the Lorentz force equation:

$$\frac{d\vec{p}}{dt} = -e\left(\vec{E} + \vec{v} \times \vec{B}\right), \tag{2.14}$$

where $\vec{p} = \gamma m_e \vec{v}$ is the relativistic electron momentum, with the Lorentz factor $\gamma = (1 - v^2/c^2)^{-1/2} = (1 + p^2/m_e^2 c^2)^{1/2}$. An electron initially at rest will begin oscillating along the electric field, resulting in a "quiver motion" in the direction of the electric field with a maximum quiver velocity $v_{max,qv} = eE_0/m_e\omega_0$. A second acceleration arises from the $\vec{v} \times \vec{B}$ component of the Lorentz force, which points in the laser propagation direction. From Eq. 2.7, the ratio of the amplitude of $\vec{v} \times \vec{B}$ force to the electric force can be expressed as $v_{max,qv}/c$. This ratio also defines the dimensionless vector potential a_0, an important parameter frequently used in high-intensity laser physics instead of the amplitude of the electric or magnetic field:

$$a_0 \equiv \frac{eE_0}{m_e c \omega_0}. \tag{2.15}$$

For $a_0 << 1$, $v_{max,qv} << c$ and the $\vec{v} \times \vec{B}$ force can be neglected. The electron mainly oscillates in the plane of the electric field. On the other hand, when $a_0 >> 1$, the maximum quiver velocity $v_{max,qv}$ approaches the speed of light c. In this relativistic regime, the magnetic force becomes dominant, and the electron is significantly pushed in the direction of laser propagation.

To obtain the exact solution of the motion of an electron in an electromagnetic field, the energy equation should be taken into account:

$$\frac{d}{dt}\left(\gamma m c^2\right) = -e(\vec{v} \cdot \vec{E}). \tag{2.16}$$

The electromagnetic fields can be expressed in terms of a vector potential $\vec{A}$ and a scalar potential Φ:

$$\begin{aligned} \vec{E} &= -\frac{\partial \vec{A}}{\partial t} - \nabla\Phi, \\ \vec{B} &= \nabla \times \vec{A}. \end{aligned} \tag{2.17}$$

Assume a plane wave propagating along the z direction, which can be represented by the wave vector:

$$\vec{A} = (\delta a_0 \cos\phi, \sqrt{1-\delta^2} a_0 \sin\phi, 0), \tag{2.18}$$

where $\phi = \omega_0 t - kz$ is the phase of the wave and δ is a polarization parameter such that $\delta = \pm 1, 0$ for a LP wave and $\pm 1/\sqrt{2}$ for a CP wave. For the sake of simplicity, all variables are normalized in relativistic units as follows: $t \to \omega_0 t, z \to kz, \vec{v} \to \vec{v}/c, \vec{p} \to \vec{p}/mc,$ and $\vec{A} \to e\vec{A}/mc^2$. Using the relation in Eq. 2.17, two equations for the momentum conservation are given by Eq. 2.14 and Eq. 2.16:

$$\begin{aligned} \vec{p}_\perp - \vec{A} &= \vec{p}_{\perp 0}, \\ \gamma - p_\parallel &= \alpha. \end{aligned} \tag{2.19}$$

The subscript $\perp$ and $\parallel$ here denote the transversal and longitudinal dimensions, respectively. The vector $\vec{p}_{\perp 0}$ stands for the constant of motion indicating the initial perpendicular momentum of the electron. For simplicity, $\vec{p}_{\perp 0} = 0$ is chosen. Additionally, the symbol α serves as another constant of motion. Using the identity $\gamma^2 - p_\parallel^2 - p_\perp^2 = 1$, the relationship between the parallel and perpendicular momenta is given by:

$$p_\parallel = \frac{1 - \alpha^2 + p_\perp^2}{2\alpha}. \tag{2.20}$$

Assuming the electron is initially at rest in the laboratory frame (i.e., $p_\parallel = p_\perp = 0$ at $t = 0$), this leads to the following momenta equations with $\alpha = 1$ calculated from Eq. 2.20:

$$\begin{aligned} p_x &= \delta a_0 \cos\phi, \\ p_y &= (1-\delta^2)^{1/2} a_0 \sin\phi, \\ p_z &= \frac{a_0^2}{4}\left[1 + (2\delta^2 - 1)\cos 2\phi\right]. \end{aligned} \tag{2.21}$$

With the help of the relation:

$$\begin{aligned} \vec{p} &= \gamma \frac{d\vec{r}}{dt} = \gamma \frac{d\phi}{dt}\frac{d\vec{r}}{d\phi} \\ &= \gamma\left(\frac{\partial\phi}{\partial t} + \frac{p_x}{\gamma}\frac{\partial\phi}{\partial x}\right)\frac{d\vec{r}}{d\phi} \\ &= \alpha \frac{d\vec{r}}{d\phi} \end{aligned} \tag{2.22}$$

The trajectory of an electron in the laboratory frame, valid for arbitrary polarization δ, can be expressed as:

$$\begin{aligned} x &= \delta a_0 \sin\phi, \\ y &= -\sqrt{(1-\delta^2)}a_0 \cos\phi, \\ z &= \frac{1}{4}a_0^2\left[\phi + \frac{2\delta^2-1}{2}\sin 2\phi\right]. \end{aligned} \tag{2.23}$$

For an LP wave, Eq. 2.21 and Eq. 2.23 describe two distinct types of motion of the electron, as shown in Fig. 2.1(a), (c), and (d).

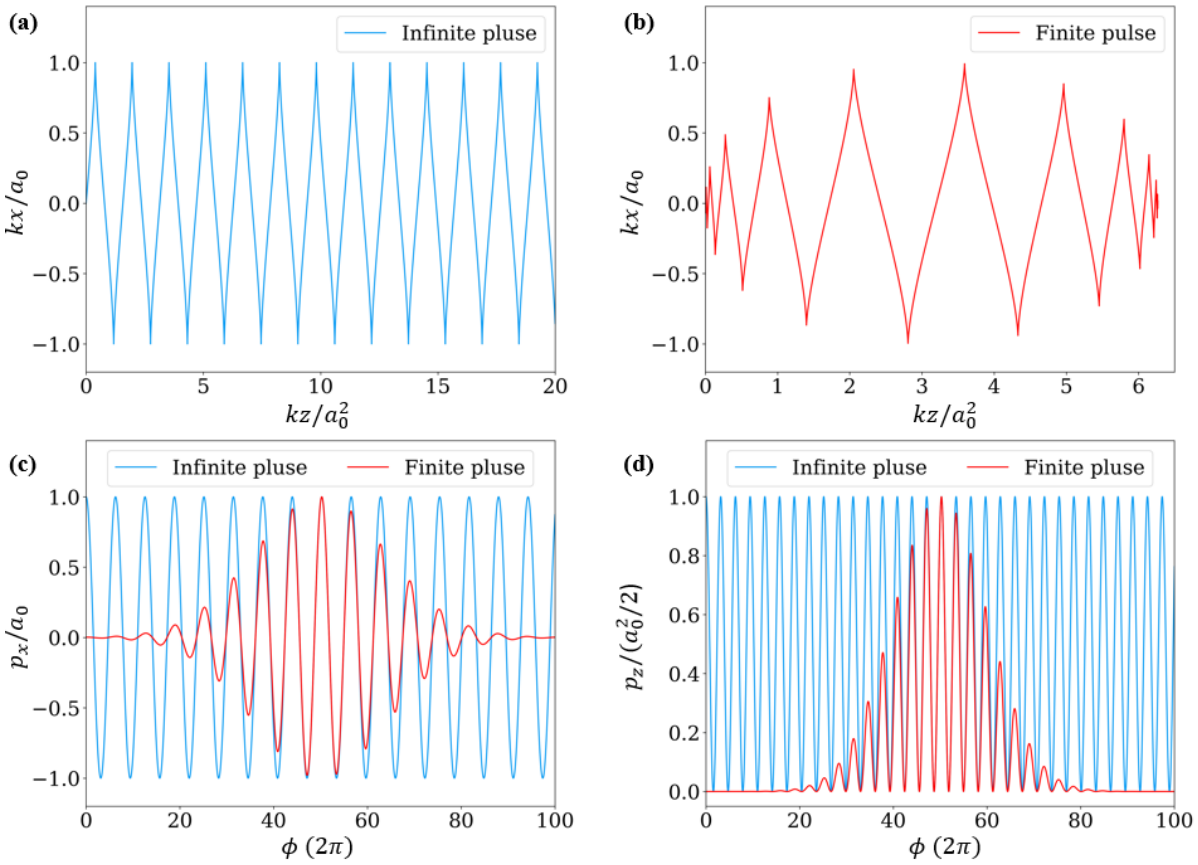

Figure 2.1: Single electron trajectories in LP plane waves. (a) Infinite pulse, $a_0 = 10$. (b) Finite pulse, $a_0(t) = a_0 \exp(-(t-50)/\tau_0)^2$ with $a_0 = 10$, and $\tau_0 = 20$. (c) and (d) show the corresponding transverse and longitudinal momentum.

The transverse motion oscillates at the laser frequency ω_0, its amplitude scaling linearly with a_0. In contrast, the longitudinal motion scales with a_0^2 and consists of two +components: an oscillatory component at double the frequency ($2\omega_0$) and a linear term ϕ, which leads to a net drift in the forward direction. The average velocity of this forward

drift is given by:

$$\frac{v_d}{c} =< \frac{p_\parallel}{\gamma} >= \frac{a_0^2}{4+a_0^2}. \tag{2.24}$$

A continuous wave laser with large a_0 is unrealistic. Considering a finite pulse duration instead, such as one with a temporally Gaussian profile described by $a_0(t) = a_0 \exp(-(t - t_p)/\tau_0)^2$ with $a_0 = 10$, $\tau_0 = 20$, and peak intensity at $t_p = 50$, the single electron motion can be calculated numerically. The results are illustrated in Fig. 2.1(b), showing the electron oscillates more prominently in the longitudinal direction as $a_0(t)$ increases.

For circularly polarized light, the longitudinal oscillating component at 2ϕ vanishes identically. The resulting electron trajectory is helicoidal, characterized by circular motion in the transverse plane with radius $a_0/\sqrt{2}$ and momentum $p_\perp = a_0/\sqrt{2}$, and a drift motion v_d in the longitudinal direction. The comparison of the electron motions in an infinite and a finite pulse is illustrated in Fig. 2.2.

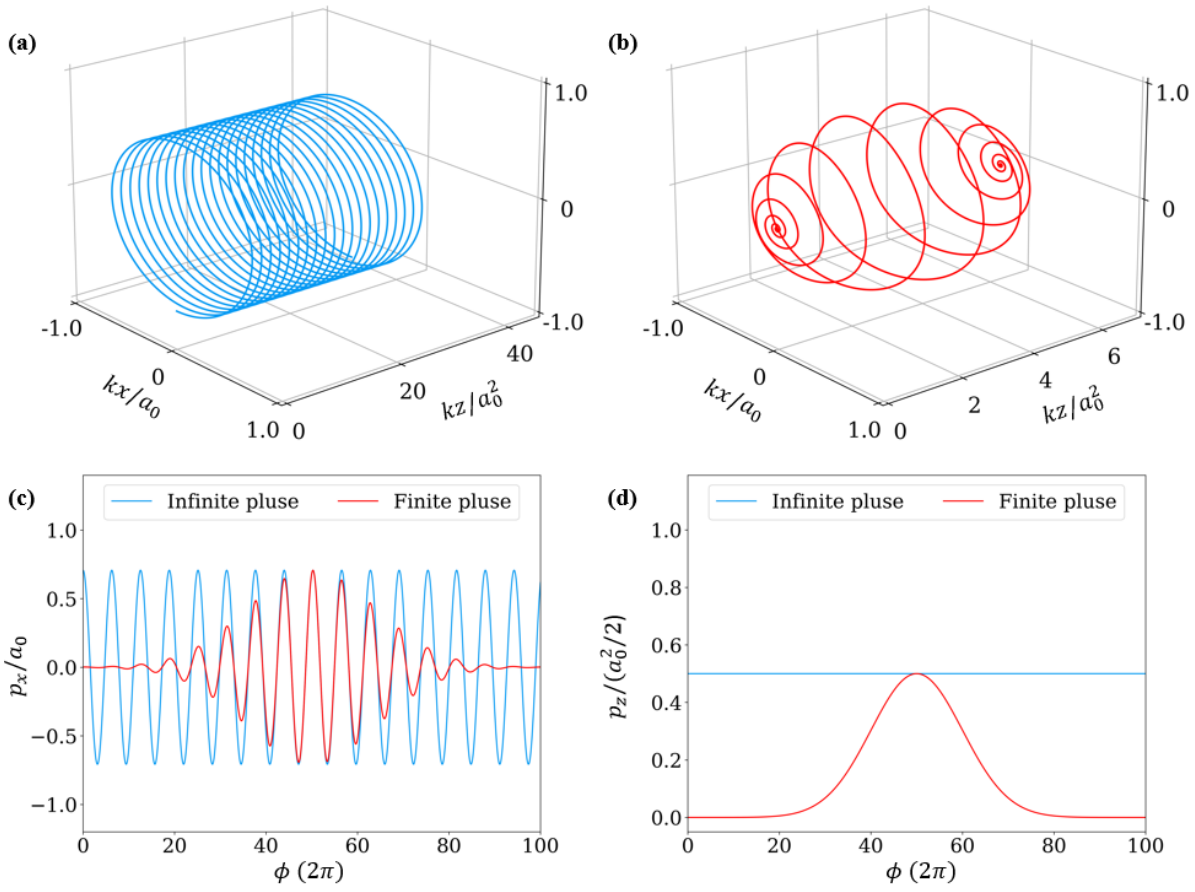

Figure 2.2: Single electron trajectories in CP plane waves. (a) Infinite pulse, $a_0 = 10$. (b) Finite pulse, $a_0(t) = a_0 \exp(-(t - 50)/\tau_0)^2$ with $a_0 = 10$, and $\tau_0 = 20$. (c) and (d) show the corresponding transverse and longitudinal momentum.

Since the electron drifts along z, transforming to a reference frame moving with a velocity $V_z = v_d$ allows for a simplified analysis of the electron's motion. In this frame, for LP plane wave, the electron's trajectory describes a distinctive "figure of eight" pattern, as illustrated in Fig. 2.3(a). This figure-eight trajectory can be expressed in the following form:

$$16z^2 = x^2(\frac{a_0^2}{\gamma_0^2} - x^2), \tag{2.25}$$

where $\gamma_0 \equiv \sqrt{1 + a_0^2/2} = \alpha$ is the motion constant in reference frame. In the extreme intensity limit ($a_0 >> 1$), $\gamma_0 \approx a_0/\sqrt{2}$. Under these conditions, the trajectory is bounded by $|z|_{max} = 1/4$ and $|x|_{max} = 1/\sqrt{2}$. For circular polarization, the orbit becomes a closed circle in the reference frame with a radius approaching 1 for $a_0 = 10$, as shown in Fig. 2.3(b).

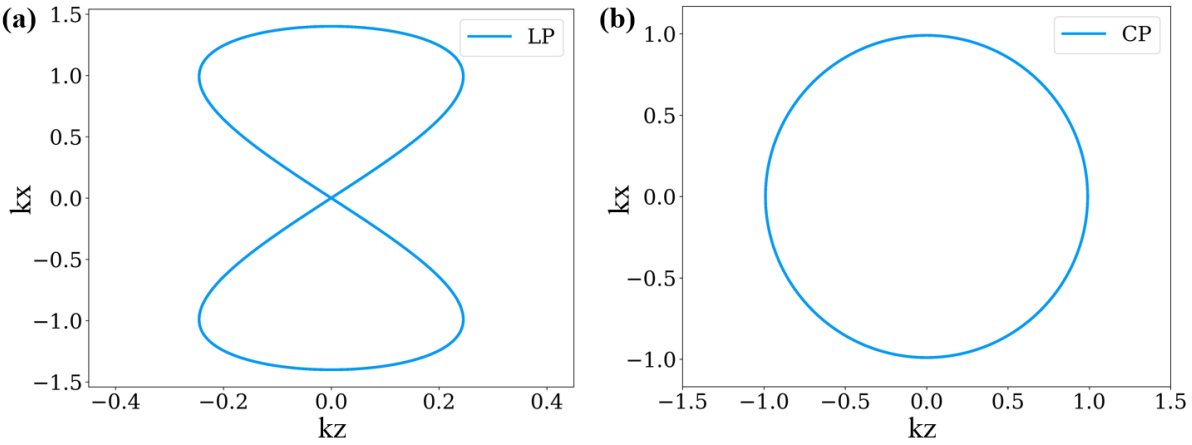

Figure 2.3: Electron motion in monochromatic plane waves ($a_0 = 10$) in the reference frame. (a) "Universal" figure-of-eight curve for LP (Eq. 2.25). (b) Closed circular orbit for CP.

An important observation from Fig. 2.1 and Fig. 2.2 is that once the laser field has overtaken the electron, the electron returns to rest, though it may end up in a different position. According to the Lawson-Woodward theorem [69, 70], an electron would gain no net energy from a plane wave even when pulsed. However, energy gain becomes possible when one of the initial conditions is violated. In high-intensity lasers, this occurs due to the tight focusing of the beam, which disrupts the assumption of an infinite transverse interaction region.

This tight focusing introduces strong radial intensity gradients across a few wavelengths. As a result, electrons near the beam center encounter stronger fields during the first half of the laser oscillation and weaker fields during the second half. This asymmetry imparts

a net velocity to the electrons, causing them to move outward once the pulse has passed. This phenomenon is in first-order described by the ponderomotive force, which can be expressed as:

$$\begin{aligned}\vec{F} &\equiv -\frac{e^2}{2m_e\omega_L^2}\vec{\nabla}\langle\vec{E}^2(\vec{r},t)\rangle \\ &= -\frac{e^2}{4m_e\omega_L^2}\vec{\nabla}\vec{E}^2(\vec{r})\end{aligned} \tag{2.26}$$

2.3 Plasma generation via ionization

In laser-plasma experiments, ionization initiates the transition from matter to plasma when the laser pulse interacts with the target. While the photon energy of the Ti:sapphire laser used in this work (1.55 eV for $\lambda = 800$ nm) is typically insufficient to directly ionize most materials (ionization potentials $\sim$ 5-15 eV), the extreme electric fields at the laser focus ($\geq 10^{12}$ V/m) enable alternative ionization mechanisms. These mechanisms include multi-photon ionization, field ionization, and collisional ionization. As a result of these processes, free electrons are generated, initiating plasma formation. This plasma then interacts with the subsequent portions of the laser pulse, leading to various energy absorption mechanisms and ultimately driving the ion acceleration process.

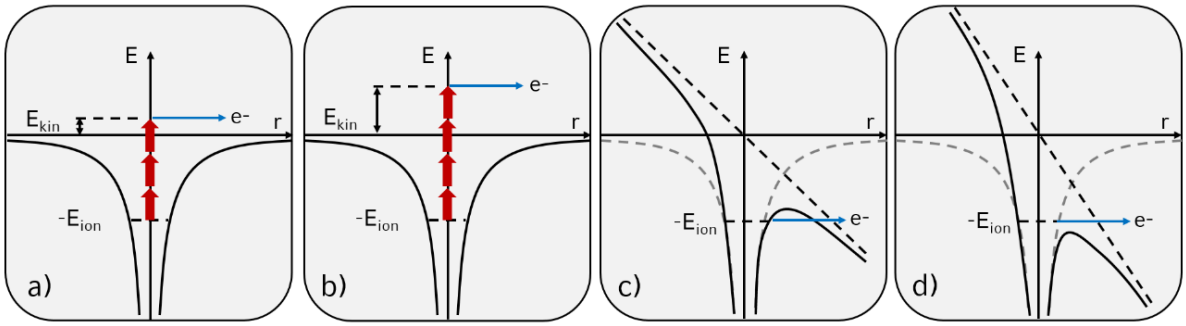

Figure 2.4: Different ionization mechanisms depending on the interaction between the laser field and the atomic potential. (a) Multiphoton ionization. (b) Above-threshold ionization. (c) Tunnel ionization. (d) Barrier suppression ionization. Reprinted with permission from [71].

2.3.1 Multiphoton ionization

Unlike single-photon ionization, Multiphoton Ionization (MPI) occurs when an atom or molecule absorbs multiple photons simultaneously or sequentially to overcome its ionization energy (E_{ion}) [72–75]. The minimum number of photons required is determined

by the condition $n_{min} \cdot E_{ph} > E_{ion}$, where E_{ph} is the energy of each photon. Any excess energy from this interaction is transferred as kinetic energy to the free electron, as shown in Fig. 2.4(a). The rate of ionization in MPI can be expressed as $w_n = \sigma_n \cdot I^n$, where σ_n is the n-photon absorption cross-section, and I is the laser intensity [76]. In cases where more photons than the minimum required are absorbed a phenomenon known as Above-Threshold Ionization (ATI) occurs [77], where the electron gains additional kinetic energy, as illustrated in Fig. 2.4(b). This results in an electron energy spectrum with distinct peaks, each separated by the photon energy [78]. These processes assume that the laser intensity remains low enough that the atomic Coulomb potential is not significantly distorted, allowing the photons to interact without perturbing the atomic structure too strongly.

2.3.2 Field ionization

As the laser intensity increases, the atomic binding potential is significantly altered by the electric field produced by the laser. This alteration can be approximated by combining the atomic potential, ϕ_{atom}, with the linear potential induced by the laser field, ϕ_L. Mathematically, this can be understood by considering simplified total potential:

$$\phi(x) = \phi_{atom}(x) + \phi_L(x) = -\frac{Ze}{4\pi\varepsilon_0 x} - Ex, \tag{2.27}$$

where E denotes the electric field strength of the laser. This modification in the potential leads to the phenomenon known as Tunnel Ionization (TI), where electrons are able to quantum mechanically tunnel through the reduced potential barrier, as illustrated in Fig. 2.4(c) [79, 80]. The ionization rates associated with TI can be calculated using several models, such as the Keldysh approach [79], the widely adopted Perelomov-Popov-Terent'ev (PPT) model [81], and the more sophisticated Ammosov-Delone-Krainov (ADK) model [82], which offers a detailed description of tunnel ionization rates in the quasi-static approximation.

Remarkably, the nature of MPI and TI is essentially similar, as demonstrated by Keldysh [79]. The general formula for the ionization probability in these processes can be expressed as:

$$w_K = Q(\gamma, I_0, \omega) \exp[-\xi(\gamma, I_0, \omega)], \tag{2.28}$$

where $Q(\gamma, I_0, \omega)$ is a preexponential factor and $\xi(\gamma, I_0, \omega)$ is given by:

$$\xi(\gamma, I_0, \omega) = \frac{2}{\hbar\omega} I_0 \left(1 + \frac{1}{2\gamma^2}\right) \left[\sinh^{-1}\gamma - \gamma \frac{(1+\gamma^2)^{1/2}}{1+2\gamma^2}\right]. \tag{2.29}$$

Here, $\gamma = \omega_L/\omega_K = \omega_L \tau_K$ is defined as Keldysh parameter with τ_K being tunneling time [79]. The Keldysh time τ_K can be derived by calculating the classical time required for a point particle to traverse a potential barrier of width $d = E_{ion}/eE$ under a constant acceleration $a = Ee/m$, resulting in $\tau_K = \sqrt{2d/a} = \sqrt{2E_{ion}m_e}/eE$.

The multifaceted nature of the Keldysh parameter is further illustrated by its alternative interpretation:

$$\gamma^2 = \frac{E_{ion}}{\frac{e^2E^2}{2m\omega_L^2}} = \frac{E_{ion}}{2U_p}, \tag{2.30}$$

where U_p is the ponderomotive energy. This formulation connects the tunneling time to the duration needed for an electron to acquire a ponderomotive energy equal to the ionization potential [83]. It is noteworthy that four widely used definitions of tunneling time exist, categorized as either "probability dependent" or "phase dependent": the Larmor time [84, 85], the Büttiker-Landauer time [86], the Eisenbud-Wigner time [87], and the Pollack-Miller time [88].

Equation 2.28 and Equation 2.29 transition into the standard tunnel effect formula at low frequencies and strong fields ($\omega_L << \omega_t$) and describes multi-photon absorption at higher frequencies ($\omega_L >> \omega_t$). In other words, the Keldysh parameter γ distinguishes between different ionization mechanisms. When $\gamma >> 1$, MPI dominates, where ionization occurs through the simultaneous absorption of multiple photons. In contrast, when $\gamma << 1$, TI becomes the primary process, allowing electrons to tunnel through the suppressed potential barrier. The transition point at $\gamma \approx 1$ represents an intermediate regime where both processes contribute significantly to the ionization process.

As laser intensity increases further, the potential barrier can be sufficiently suppressed such that the local maximum of the modified Coulomb potential drops below the ionization potential of the atom. This process is referred to as Barrier Suppression Ionization (BSI) [89]. The critical electric field strength E_{BSI} for BSI can be determined by setting the ionization potential E_{ion}/e equal to the potential at the local maximum x_{max} of Eq. 2.27:

$$\begin{aligned} x_{max} &= \sqrt{\frac{Ze}{4\pi\varepsilon_0 E_{BSI}}}, \\ E_{BSI} &= \frac{\pi\varepsilon_0}{Ze^3} E_{ion}^2. \end{aligned} \tag{2.31}$$

The corresponding laser intensity for BSI directly follows Eq. 2.9. For hydrogen, with an ionization energy of $E_{ion} = 13.6$ eV, BSI is achieved at an intensity of $I \approx 1.4{\times}10^{14}\,\mathrm{W/cm^2}$. In comparison, for the carbon ion C^{4+} with an ionization energy of $E_{ion} = 64.5$ eV, the intensity required for BSI is around $I \approx 4.3 \times 10^{15}\,\mathrm{W/cm^2}$.

2.3.3 Collisional ionization

Collisional ionization is a fundamental process in plasma physics where free electrons with sufficient kinetic energy collide with atoms or ions, causing the ejection of bound electrons. This mechanism plays a crucial role in determining the ionization state and overall behavior of plasmas, particularly in high-density environments such as laser-induced plasmas, stellar atmospheres, and fusion experiments.

The rate of collisional ionization is typically expressed as:

$$w = n_e \langle \sigma_i v_e \rangle, \tag{2.32}$$

where n_e is the free electron density, v_e is the electron velocity, and σ_i is the ionization cross-section. For electrons with kinetic energy significantly exceeding the ionization energy ($E_{kin} >> E_{ion}$), the ionization cross-section can be approximated using the Lotz empirical formula [90, 91]:

$$\sigma_i = a_i q_i \frac{ln\left(E_{kin}/E_{ion}\right)}{E_{kin} E_{ion}}, \tag{2.33}$$

where a_i is an empirical constant and q_i is the number of electrons present in the outer shell of the ion. For electrons following a Maxwellian energy distribution with average kinetic energy $k_B T_e$, the thermal ionization rate can be expressed as [92]:

$$w_{thermal} = \frac{n_e a_i q_i}{E_{ion}\sqrt{k_B T_e}} \int_{E_{ion}/k_B T_e}^{+\infty} \frac{e^{-x}}{x} dx. \tag{2.34}$$

This expression accounts only for collisions initiated by electrons with sufficient thermal energy to cause ionization. However, it is also essential to consider the kinetic energy contributions from the oscillation of electrons influenced by the laser field. Following the approach outlined in [92], and substituting $v_e\left(t\right) = eE_0/(m_e\omega)sin(\omega t)$, the average ionization rate over a complete laser cycle can be formulated as:

$$w_{laser} = \frac{n_e a_i q_i}{\pi E_{ion}\sqrt{m_e U_p}} \int_{E_{ion}}^{2U_p} \frac{ln\left(E_{kin}/E_{ion}\right)}{2E_{kin}} \frac{1}{\sqrt{1 - \frac{E_{kin}}{2U_p}}} dE_{kin}, \tag{2.35}$$

where U_p is the ponderomotive energy. When a sufficient number of electrons are released from the target and effectively heated, collisional ionization can lead to high charge states at laser intensities considerably lower than those required for field ionization [93].

2.4 Basics of plasma

Having introduced the primary mechanisms through which matter can be ionized by high-intensity laser interactions, the resulting phenomena in plasmas can now be described. Plasma, often referred to as the fourth state of matter, is an ionized medium composed of free electrons, ions, and neutral particles. It is characterized by collective behavior and quasi-neutrality, where the electron and ion densities are approximately equal on macroscopic scales [94]. Plasma is prevalent throughout the universe, comprising over 99% of visible matter, and plays a crucial role in various natural phenomena and technological applications [95].

A key parameter in plasma physics is the Debye length (λ_D), which characterizes the distance over which charge separation effects are screened:

$$\lambda_D = \sqrt{\frac{\epsilon_0 k_B T_e}{n_e e^2}}, \tag{2.36}$$

where ϵ_0 is the vacuum permittivity, k_B is the Boltzmann constant, T_e is the electron temperature, and n_e is the electron density. The Debye length is fundamental to understanding plasma behavior, as it defines the scale over which collective effects dominate individual particle interactions. For simplification, the collisional behavior is ignored and plasma is considered collisionless for the following analysis.

Another important parameter is the plasma frequency (ω_p), which represents the natural oscillation frequency of electrons in response to charge separation when subjected to external perturbations, such as a laser interacting with the plasma. It is given by the expression:

$$\omega_{p,e} = \sqrt{\frac{n_e e^2}{\epsilon_0 m_e}} = \frac{v_e}{\lambda_D}. \tag{2.37}$$

The influence of the ions can typically be neglected in plasma dynamics due to their larger mass compared to electrons. Therefore, the analysis can be simplified by setting $\omega_p \equiv \omega_{p,e}$ to represent the plasma frequency solely for electrons in the following sections. The dispersion relation of an electromagnetic wave with wave number $k_L = 2\pi/\lambda$ propagating

through a collisionless plasma can be expressed as:

$$\omega_L^2 = \omega_p^2 + k_L^2 c^2 \tag{2.38}$$

From the dispersion relation provided, both the phase velocity v_p and group velocity v_g of the laser propagating in the plasma follow:

$$\begin{aligned} v_p &= \frac{\omega_L}{k_L} = \frac{c}{\eta}, \\ v_g &= \frac{d\omega_L}{dk_L} = c\eta, \end{aligned} \tag{2.39}$$

where $\eta = \sqrt{1 - \omega_p^2/\omega_L^2} = \sqrt{1 - n_e/\gamma n_c}$ is the refraction index. When $\omega_L = \omega_p$, the group velocity of the laser pulse becomes zero ($v_g = 0$), indicating that the electromagnetic wave cannot propagate further into the plasma. This condition represents the point of reflection for the incident laser light and defines the critical density n_c:

$$n_c = \frac{\epsilon_0 \gamma m_e \omega_L^2}{e^2} = \langle\gamma\rangle \cdot \frac{1.1 \times 10^{21} cm^{-3}}{\lambda^2\,[\mu m^2]}, \tag{2.40}$$

where $\langle\gamma\rangle = \gamma_0 = \sqrt{1 + a_0^2/2}$ is the average Lorentz factor typically employed for representing relativistic motion of plasma electrons.

The critical density (n_c) divides plasmas into two categories. In the case of underdense plasma ($n_e < n_c$), the laser pulse can propagate through the plasma. Conversely, in overdense plasma ($n_e > n_c$), the laser pulse is reflected at the critical surface where $n_e = n_c$. Within this region, the laser pulse becomes evanescent, indicating that the electric field's strength diminishes exponentially. This decay is characterized by the skin depth (l_s), which represents the distance over which the electric field reduces to $1/e$ of its initial value. The skin depth for a collisionless, step-like plasma can be expressed mathematically as:

$$l_s = \frac{c}{\omega_L \,\mathrm{Im}(\eta)} = \lambda_L \left[2\pi \sqrt{\frac{n_e}{\gamma n_c} - 1}\right]^{-1}. \tag{2.41}$$

For highly overdense plasma, where $\omega_p >> \omega_L$, the skin depth can be approximated as $l_s \approx c/\omega_p$.

Under typical conditions, an overdense plasma is considered opaque to laser pulses. However, at very high laser intensities (e.g., $I > 10^{18}\mathrm{W/cm}^2$ for a wavelength of 1 µm), relativistic effects become significant. The effective critical density increases due to the relativistic mass increase of osillating electrons, allowing the laser to penetrate deeper into

the plasma. Consequently, the initially opaque plasma can suddenly become transparent when $n_e/\gamma n_c \leq 1$. This phenomenon is referred to as relativistic-induced transparency, because γ depends on the laser-field strength that induces electron motion.

2.5 Laser absorption in plasma

In laser-plasma interactions for ion acceleration, the laser primarily interacts with electrons due to their much lower mass compared to ions. Even at the highest achievable laser intensities (up to approximately $10^{23}\mathrm{W/cm}^2$), the laser field is insufficient to directly accelerate ions to significant energies. Instead, the laser energy is first transferred to the electrons. As these electrons are driven forward by the laser, they create a strong electrostatic field due to charge separation. This electrostatic field, which can be comparable in strength to the laser field itself, acts on the ions, thereby facilitating their acceleration. Consequently, understanding how the laser energy is transferred to the electrons is essential for determining the overall efficiency of ion acceleration. The following sections will briefly outline several key absorption mechanisms, with a more detailed discussion available in [96].

2.5.1 Inverse bremsstrahlung

Inverse bremsstrahlung is a fundamental collisional absorption mechanism in laser-plasma interactions, particularly relevant at low laser intensity ($I \leq 10^{15}\mathrm{w/cm}^2$). This process involves two sequential processes. First, electrons oscillate under the influence of the laser field. Subsequently, the quiver energy is transferred to the plasma through collisions with ions, resulting in effective plasma heating. The electron-ion collision frequency for inverse bremsstrahlung (ν_{ei}) in a plasma can be expressed as [66]:

$$\nu_{ei} \propto \frac{n_e Z}{T_e^{3/2}}. \tag{2.42}$$

The absorption of laser energy via inverse bremsstrahlung is more significant in plasma with high densities, high atomic numbers (Z), and low electron temperature. However, as the laser intensity increases, the electron temperature also rises, leading to a decrease in the efficiency of inverse bremsstrahlung. At higher intensities, where electron temperatures become substantial, collisionless absorption mechanisms start to dominate the heating process. A discussion of these mechanisms will follow in the subsequent sections.

2.5.2 Resonance absorption

Resonant absorption occurs when the frequency of the incident laser pulse matches the local frequency of a plasma ($\omega_L = \omega_p$), typically at a specific layer within an inhomogeneous plasma where $n_e = n_c$. As the laser cannot reach n_c except for normal incidence, this process involves the tunneling of the electromagnetic wave to the critical density surface, where it excites electron plasma waves. These waves subsequently decay, transferring their energy to the plasma electrons. It is governed by collective effect (collisionless), allowing for efficient conversion of laser energy into plasma energy, particularly for obliquely incident p-polarized light.

The efficiency of resonant absorption depends on several parameters, including the angle of incidence, plasma density scale length, and laser intensity [97]. For optimal absorption, the component of the laser electric field parallel to the density gradient should be maximized, which occurs at a specific angle of incidence. The resonant absorption process can be mathematically described using the following expression for the fractional absorption f_A:

$$f_A \approx \frac{\phi^2(\tau)}{2}, \tag{2.43}$$

where $\phi(\tau) \approx 2.3\tau e^{-2\tau^3/3}$ is the characteristic function for the efficiency of resonance absorption and $\tau = (\omega L/c)^{1/3} sin\theta$ is defined by the plasma density scale length L and the angle of incidence θ.

2.5.3 Vacuum/Brunel heating

Vacuum heating, also known as the Brunel effect, is particularly relevant for high-intensity, short-pulse lasers incident on steep plasma density gradients. This process, first described by Brunel [98], occurs when electrons at the plasma-vacuum interface are directly driven by the laser field. During one half-cycle of the laser field, electrons are pulled from the plasma into the vacuum. As the field reverses in the next half-cycle, these electrons are accelerated back into the plasma. Upon re-entering the plasma, the electrons are shielded from the laser field and continue to propagate deeper into the target, gaining energy from the laser in the process.

The efficiency of vacuum heating depends on several parameters, including the laser intensity, angle of incidence, and plasma density gradient. For p-polarized light at oblique incidence, the fractional absorption f_{vh} due to vacuum heating can be approximated

by [64]:

$$f_{vh} = \frac{4}{\pi} \frac{\sin^3 \theta}{\cos \theta} a_0 \tag{2.44}$$

Vacuum heating becomes particularly important when the electron excursion length in the laser field is comparable to or exceeds the plasma scale length. This condition is often met in experiments using high-contrast, ultra-short pulse lasers interacting with solid targets.

2.5.4 Relativistic j x B heating

The $\mathbf{j} \times \mathbf{B}$ heating mechanism arises from the oscillating component of the ponderomotive force (Eq. 2.26) exerted by the laser field on the electrons. In the relativistic regime ($a_0 \gg 1$), the magnetic field of the laser becomes significant, and the Lorentz force $\mathbf{v} \times \mathbf{B}$ induces a notable dominating longitudinal oscillation at twice the laser frequency ($2\omega_L$) for LP laser pulses. Unlike resonance absorption and vacuum heating, this mechanism works regardless of polarization (except for circular) and achieves maximum absorption at normal incidence.

2.6 Laser-driven ion acceleration

As mentioned earlier, it is not feasible to directly accelerate ions via the laser field with current laser intensities. Most ion acceleration mechanisms investigated so far are driven by charge separation between fast-moving electrons and ions. Various mechanisms have been proposed based on different laser and target parameters, including Coulomb Explosion (CE) [99], Collisionless Shock Acceleration (CSA) [100–102], Magnetic Vortex Acceleration [103–105], Breakout Afterburner (BOA) [106–109], Relativistic Induced Transparency (RIT) [110–113], and several other processes. For a more detailed overview, refer to existing review articles [26–28]. The following sections will focus on the ion acceleration mechanisms most relevant to the investigations presented in this thesis.

2.6.1 Target normal sheath acceleration

Target Normal Sheath Acceleration (TNSA) is a fundamental mechanism in laser-driven ion acceleration, first described by [114,115]. This process has become the most extensively studied and reliable method for generating energetic ion beams using high-intensity lasers. TNSA occurs when an ultra-intense, short-pulse laser interacts with a thin solid target,

typically a few micrometers in thickness. A simplified schematic of this mechanism is shown in Fig. 2.5. The laser prepulse ionizes and heats the front surface of the target, creating a pre-plasma. The main pulse then interacts with this plasma at the critical surface. Through various absorption mechanisms previously discussed, the laser energy is partially transferred to electrons, which are heated to relativistic temperatures. These hot electrons propagate through the target, with some escaping from the rear surface. As electrons leave the target, a strong electrostatic sheath field is established at the rear surface, typically on the order of MV/µm or TV/m. This intense field ionizes atoms at the target rear and accelerates the resulting ions, predominantly protons due to their high charge-to-mass ratio, in the direction normal to the target surface. Ion bunches generated from TNSA are commonly characterized by broad, exponential-like energy spectra.

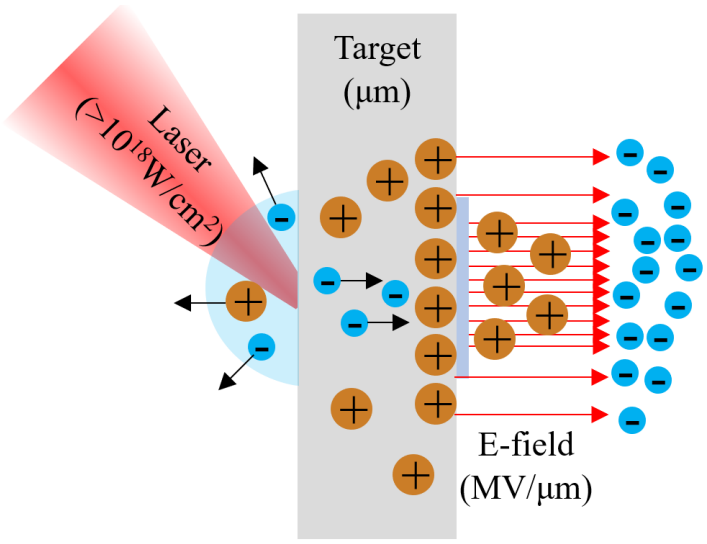

Figure 2.5: Schematic of TNSA mechanism.

The electric field responsible for ion acceleration at the rear surface of the target in the TNSA mechanism can be estimated by:

$$E_{acc} = \sqrt{\frac{2}{e_N}} \frac{k_B T_e}{e\lambda_D}, \tag{2.45}$$

where $e_N \approx 2.71828$ is Euler's number, $k_B T_e$ is electron thermal energy, and λ_D represents Debye length. This field drives the ions, and the maximum ion energy (E_{max}) can be

approximated using the model of freely expanding plasma as described by Mora [116]:

$$E_{max} = 2Zk_BT_e[\ln(\tau + \sqrt{\tau^2 + 1})]^2, \tag{2.46}$$

where Z is the ion charge state and $\tau = 0.43\omega_{pi}\tau_L$ with $\omega_{pi} = \sqrt{n_{e0}Ze^2/m_i\epsilon_0}$ being ion plasma frequency. The electron thermal energy k_BT_e, widely accepted to be equal to the ponderomotive energy U_p, scales with $(I_0\lambda^2)^{1/2}$. The hot electron energy can be written as:

$$k_BT_e = U_p = m_ec^2[\sqrt{1 + a_0^2} - 1]. \tag{2.47}$$

In an alternative approach, the TNSA mechanism can be described in terms of laser absorption by electrons [117]. This model simplifies the analysis by bypassing the complexities associated with electron heating during laser-plasma interactions. The maximum ion energy E_{max} can be determined, accounting for the finite acceleration time, and is given by:

$$\begin{aligned} E_{max} &= X^2E_{i,\infty}, \\ \frac{\tau_L}{\tau_0} &= X[1 + \frac{1}{2(1 - X^2)}] + \frac{1}{4}\ln\frac{1 + X}{1 - X}. \end{aligned} \tag{2.48}$$

Here $E_{i,\infty} = 2Zm_ec^2\sqrt{\eta P_L/P_R}$ represents the maximum achievable ion energy, assuming an infinitely long acceleration time. In this expression, P_L is the laser power, and $P_R = m_e^2c^5/e^2 = 8.71$ GW is the relativistic power unit. The characteristic acceleration time is given by $\tau_0 = B/v_{i,\infty}$, where $B = r_L + d \cdot tan\theta$ represents the radius of the electron bunch on the target's rear surface, with r_L being the radius of the laser, d the target thickness, and θ the half-angle of the electron propagation through the target. The factor $X = tanh(\tau_L/2\tau_0)$, while not mathematically correct, provides a close approximation to the exact solution. This model differs from Eq. 2.46 and shows no explicit dependence on laser intensity I_0, but both models describe maximum energy quite well.

2.6.2 Radiation pressure acceleration

The concept of Radiation Pressure Acceleration (RPA) was first proposed theoretically by Esirkepov et al. in 2004 [118], building upon earlier ideas of light pressure propulsion for interstellar travel [119]. RPA is an advanced mechanism for laser-driven ion acceleration that has gained significant attention due to its potential for generating high-energy, quasi-monoenergetic ion bunches with high conversion efficiency.

However, the extremely high laser intensities required for RPA ($I_0 > 10^{23}$ W/cm^2)

and the necessity for a sharply defined (non-Gaussian) laser front present significant experimental challenges. This limitation persisted until it was realized that using a CP laser pulse could help mitigate these stringent requirements [120]. As discussed in Sections 2.2 and 2.5.4, CP eliminates the oscillating component of the $\mathbf{j} \times \mathbf{B}$ force, which significantly suppresses electron heating. Consequently, the ion acceleration mechanism driven by TNSA is diminished, allowing RPA to become the dominant process at much lower laser intensities. RPA can be categorized into two principal regimes: Hole-Boring (HB) [120, 121] and Light Sail (LS) [122, 123].

Hole-Boring RPA (HB-RPA) is applicable to thick targets. In this regime, when a Circular Polarization (CP) laser pulse irradiates the target's front surface, the steady ponderomotive force "softly" pushes electrons into the target. These electrons accumulate in a compressed layer, creating a charge-separation region and generating a localized spike in the electrostatic field that restrains them. This electrostatic field subsequently accelerates ions, eventually catching up with the compressed electron layer [120, 124]. The process is analogous to the way a laser pulse pushes plasma forward via radiation pressure, reflecting ions from the plasma surface at velocities up to twice the recession velocity, a phenomenon known as shock acceleration.

In the non-relativistic case, the acceleration time τ_i and the maximum ion velocity $v_{max,HB} = 2v_{i,HB}$ were derived by Macchi et al. [120] as follows:

$$\tau_i \simeq \frac{1}{\omega_L a_0}\sqrt{\frac{A}{Z}\frac{m_i}{m_e}} \quad \text{and} \quad \frac{v_{i,HB}}{c} = \sqrt{\frac{Z}{A}\frac{m_e}{m_i}\frac{n_c}{n_e}}a_0, \tag{2.49}$$

where $v_{i,HB}$, ω_L, and a_0 represent ion velocity of HB-RPA, laser frequency, and dimensionless laser amplitude, respectively; m_i and m_e are the mass of ion and electron; n_e and n_c are electron density and critical density.

The analysis was further expanded to the relativistic regime by Robinson et al. [125]:

$$\frac{v_{i,HB}}{c} = \frac{\sqrt{\Xi}}{1+\sqrt{\Xi}} \quad \text{and} \quad E_{max} = m_{\mathrm{i}}c^2\left[\frac{2\Xi}{1+2\sqrt{\Xi}}\right], \tag{2.50}$$

where $\Xi = I_0/\rho c^3$ is a dimensionless parameter and $\rho = m_i n_i$ represents the mass density of the plasma.

As long as the laser does not end, the HB mechanism persistently accelerates ions through a repetitive process. This acceleration continues until all adjacent ions attain the same velocity $v_{max,HB}$ as reflected by the HB front when the compression layer reaches the target's initial rear surface. Once the entire ion mass has been set into motion, the

acceleration transitions to a subsequent stage known as Light Sail (LS) acceleration. In this phase, the entire target behaves as a plasma slab that is propelled by radiation pressure, achieving nearly uniform maximum velocity.

Light Sail RPA (LS-RPA) is relevant for ultrathin targets, where the thickness $d << \lambda$ or thin enough so that the hole boring phase is very short. In this regime, the radiation pressure can propel all electrons within the irradiated area of the target to velocities approaching the speed of light, while the ions remain relatively stationary. This results in the formation of a strong electrostatic field due to charge separation. Such a powerful electrostatic field is capable of accelerating the ions to relativistic energies within a single laser cycle, provided the laser intensity is extremely high, specifically greater than $I_0 > 10^{23}$ W/cm^2. In this scenario, the target effectively moves together with the laser pulse, resembling the dynamics of a light sail moving at relativistic speed.

The transition between HB-RPA and LS-RPA is influenced by both the target thickness and the laser parameters. LS-RPA is optimized when the areal density of the target aligns with the intensity of the laser pulse, which can be expressed mathematically as:

$$a_0 = \pi \frac{n_e}{n_c} \frac{d}{\lambda}. \tag{2.51}$$

In terms of maximum velocity $v_{max,LS}$, two cases can be considered: the non-relativistic and the ultrarelativistic. For the non-relativistic case, the maximum velocity derived from momentum conservation is given by [126]:

$$\frac{v_{max,LS}}{c} \approx \frac{2 I_0 \tau_L}{\sigma c^2}. \tag{2.52}$$

where σ is the areal density. In contrast, for the ultrarelativistic case [118, 127], where $(\tau_{acc} \to \infty)$, the maximum velocity can be expressed as:

$$\frac{v_{max,LS}}{c} \approx \left(\frac{Z a_0^2}{\sigma} \frac{m_e}{m_i} \frac{c \tau_{acc}}{\lambda} \right)^{1/3}. \tag{2.53}$$

Consequently, RPA demonstrates a favorable scaling of ion energy with respect to laser intensity, characterized by $E_{max} \propto I_0^{\alpha}$ where $1/3 \leq \alpha \leq 2$. This scaling has the potential to surpass the performance of other acceleration mechanisms at high intensities. Recent experimental investigations have demonstrated partial RPA features, such as peaked ion energy spectra [126, 128], circular polarization enhancement [129, 130], and rapid scaling [131].

Chapter 3

High repetition rate water-leaf target for laser-driven ion acceleration

This chapter introduces high repetition rate water-leaf targets, also known as liquid sheets, based on colliding jets. It covers the historical development, underlying physics, experimental setup, characterization methods, and challenges associated with the water-leaf target system.

3.1 History of liquid leaf targets

The evolution of liquid leaf targets can be traced through a series of scientific advancements spanning several decades. Initial investigations into thin liquid leaves were primarily motivated by industrial applications. In 1954, Dombrowski and Fraser's pioneering study provided crucial insights into the disintegration dynamics of liquid leaves [132], laying the foundation for their use in pesticide spraying. By the 1980s, research into fuel injection systems began to highlight the role of liquid leaves, with Naber and Reitz examining how these leaves impact spray-wall impingement processes [133]. In 1989, Watanabe et al. introduced liquid leaf jets to dye laser technology [134], expanding the use of these leaves for laser applications. Further theoretical advancements were made in 2007, when Clanet and Villermaux analyzed water bell physics providing insights into liquid leaf dynamics [135].

By the early 2000s, liquid targets had entered laser-plasma research, demonstrated by Thoss et al. for high-repetition-rate plasma generation [53]. This foundation supported the development of liquid leaf targets for laser-driven ion acceleration, which took a significant step forward in 2015 when Ekimova et al. studied liquid targets for MeV-scale ion acceleration [54]. In recent years, liquid leaf targets have become common in ion acceleration experiments, as seen in studies by Morrison et al. [55] and subsequent studies by Puyuelo et al. [56] and others [57, 60].

These studies have demonstrated the effectiveness of liquid leaf targets for high repetition rate operation, a key requirement for advancing research in laser-plasma physics. Ongoing research aims to further optimize these targets for practical applications such as neutron production and medical physics while addressing technical challenges such as stability and vibration control. This evolution highlights the transformation of liquid leaf targets from industrial tools to important components of advanced laser-plasma physics experiments, emphasizing their potential to drive high-repetition-rate laser-driven ion acceleration.

3.2 Fundamentals of water-leaf target

There are several methods available for generating water-leaf targets, each with unique benefits. For this thesis study, the colliding jets technique was selected. This section will focus on the fundamentals of this method, with the reasons for choosing the colliding jets technique discussed in a later section.

3.2.1 Dimensionless numbers analysis

Analyzing various dimensionless numbers provides valuable insights into liquid behavior. When two identical, high-Reynolds-number laminar fluid jets collide at high speeds with negligible gravitational effects, the dynamics are mainly influenced by fluid inertia and surface tension. Therefore, the Reynolds number and the Weber number are fundamental for understanding the dynamics of liquid-leaf targets. The Reynolds number, defined as the ratio of inertial to viscous forces, is given by:

$$\mathrm{Re} = \frac{\rho u L}{\mu} = \frac{u L}{\nu}, \tag{3.1}$$

where ρ represents the density of the liquid, u is the velocity of the liquid, L is a characteristic length, μ denotes the dynamic viscosity of the liquid, and $\nu = \mu/\rho$ is the kinematic viscosity. The Reynolds number is often used to predict whether a liquid flow is likely to be laminar or turbulent, with a critical threshold of around 2000. For thin liquid-leaf targets, the Reynolds number mainly indicates the likelihood of capillary waves forming on the liquid-leaf's surface. These waves can have a strong impact on the stability or breakup of the liquid-leaf targets.

The Weber number is defined as the ratio of fluid's inertia compared to its surface

tension, expressed by:

$$\mathrm{We} = \frac{\rho u^2 L}{\sigma}, \tag{3.2}$$

where σ is the surface tension of the liquid. The Weber number is crucial for understanding the formation and stability of the liquid leaf. It characterizes the balance between the inertial forces driving the liquid leaf's expansion and the surface tension forces resisting this expansion. Higher Weber numbers indicate that inertial forces dominate over surface tension, which can lead to the disintegration of the liquid-leaf target as surface tension is unable to maintain the leaf's integrity.

3.2.2 Governing equations

When two identical laminar liquid jets collide at an oblique angle 2α, they form a liquid leaf that lies in a plane perpendicular to the incidence plane of the jets. The liquid within this leaf spreads radially from the collision point at a relatively uniform speed, creating a leaf-like shape. The surface tension's curvature force acts perpendicularly to the edges of the fluid leaf, restricting its lateral spread. Additionally, this curvature force causes the leaf to retract and eventually close, forming the apex of the initial link. As fluid gathers at the leaf's edges, it forms thick rims that define the fluid leaf's boundaries. When these rims converge at the apex, they produce a new thin leaf in a plane perpendicular to the first leaf. This process continues, generating successively smaller, mutually orthogonal leaves until the chain disintegrates into droplets and spray. An example of this multi-leaf generation is shown in Fig. 3.1.

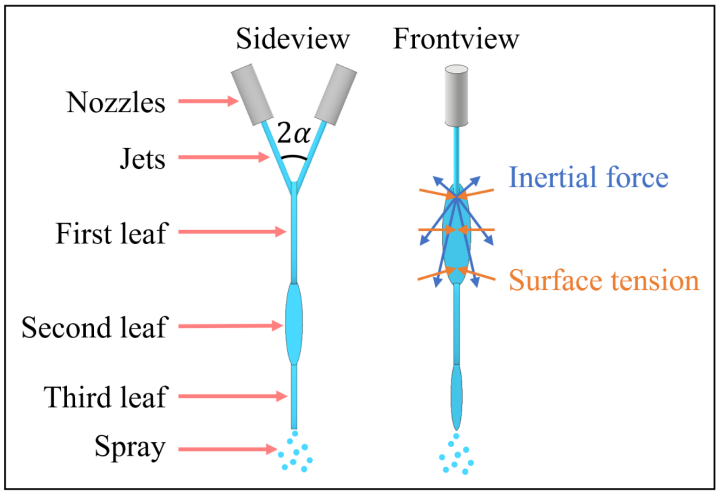

Figure 3.1: Schematic of multi-leaf target. The front view is oriented in the direction normal to the target surface.

To determine the shape of the liquid leaf and the characteristics of the rim, the analysis by Bremond et al. [136] is followed. Figure 3.2(a) illustrates the coordinate system for analyzing the thin liquid leaf bounded by a rim, which is generated by two identical jets colliding at a full angle of 2α. Figure 3.2(b) presents a schematic of the control volume for the leaf and its bounding rim. Both figures are adapted from Figure 4 of Bremond et al. [136].

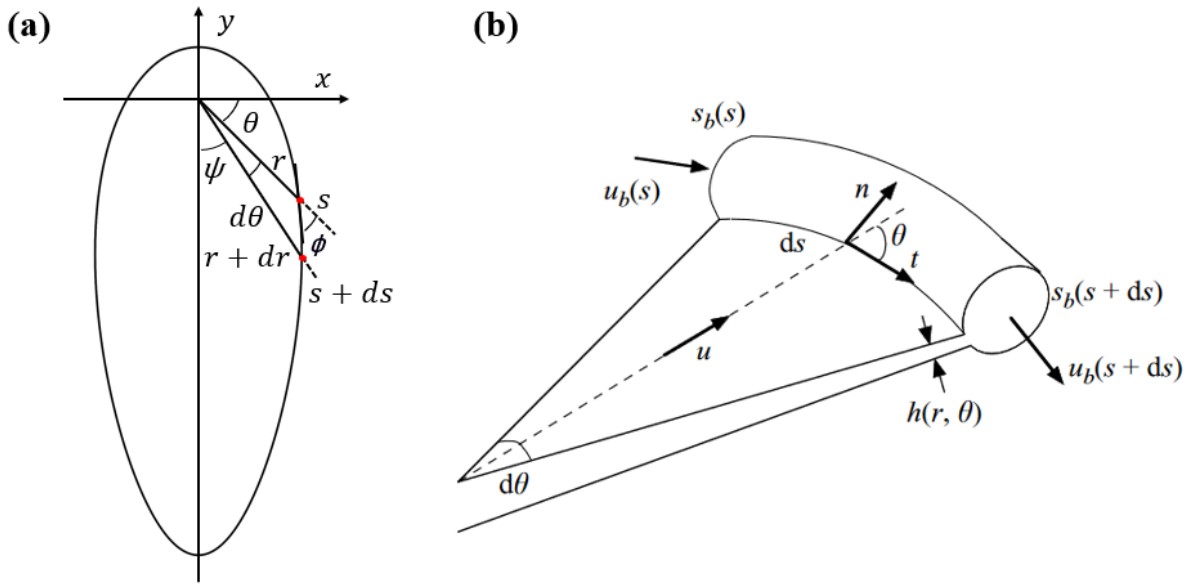

Figure 3.2: (a) Coordinate system used for analyzing the liquid leaf created by the collision of two identical impinging jets. (b) Schematic diagram depicting the differential control volume assumed for deriving mass and momentum conservation equations. The figure is adapted with permission from [136].

First, given that the edge is stationary, mass conservation must be maintained in each segment of the rim. Specifically, the flux exiting a segment of the arc ds must equal the flux entering that segment from the leaf. This conservation principle can be expressed mathematically as:

$$\rho \frac{\mathrm{d}(u_b s_b)}{\mathrm{d}s} = \rho u h \sin\phi, \tag{3.3}$$

where ρ is the density of the liquid, u_b represents the velocity of the fluid along the centerline of the rim, s_b denotes the cross-sectional area of the rim, u is the velocity along the streamline intersecting ds, h is the thickness of the leaf just before the rim, and ϕ is the angle between the direction of a radius r and the direction of the tangent to the

curve at a specific point s. The geometric relationship of ϕ can be expressed as:

$$\sin\phi = r\frac{\mathrm{d}\theta}{\mathrm{d}s}, \quad \tan\phi = r\frac{\mathrm{d}\theta}{\mathrm{d}r}. \tag{3.4}$$

The conservation of momentum for a rim can be expressed in terms of components tangential and normal to the rim. The tangential component of the momentum conservation for the rim is given by:

$$\rho\frac{\mathrm{d}\left(u_b^2 s_b\right)}{\mathrm{d}s} = \rho u^2 h\sin\phi\cos\phi. \tag{3.5}$$

Similarly, the normal component of the momentum conservation for the rim is described by:

$$\rho u_b^2 s_b(\mathrm{d}\theta + \mathrm{d}\phi) = 2\sigma\ \mathrm{d}s - \rho u^2 h\sin^2\phi\ \mathrm{d}s. \tag{3.6}$$

By substituting Eq. 3.4 into Eq. 3.3, Eq. 3.5, and Eq. 3.6, a corresponding set of differential equations can be derived. These equations describe the shape and profile of the rims of the leaf and can be expressed as follows:

$$\begin{aligned}
\frac{d(s_\mathrm{b}u_\mathrm{b})}{d\theta} &= uF(\theta,\alpha)\\
\frac{d(s_\mathrm{b}u_\mathrm{b}^2)}{d\theta} &= u^2\cos\phi F(\theta,\alpha)\\
s_\mathrm{b}u_\mathrm{b}^2\left(\frac{d\phi}{d\theta}+1\right)\sin\phi &= \frac{2\sigma r}{\rho} - u^2\sin^2\phi F(\theta,\alpha)\\
\frac{dr}{d\theta} &= \frac{r}{\tan\phi},
\end{aligned} \tag{3.7}$$

where $h = F(\theta,\alpha)/r$ is inspired by Taylor [137]. To generalize the analysis, characteristic length and velocity scales are introduced: a characteristic length scale d_j representing the diameter of the interacting jets and a characteristic velocity scale u_j denoting the velocity of the fluid within the leaf. By normalizing the governing equations with respect to these characteristic scales, dimensionless forms are obtained:

$$\begin{aligned}
\frac{\mathrm{d}(\tilde{u}_b\tilde{s}_b)}{\mathrm{d}\theta} &= F(\theta,\alpha),\\
\frac{\mathrm{d}\left(\tilde{u}_b^2\tilde{s}_b\right)}{\mathrm{d}\theta} &= \cos\phi F(\theta,\alpha),\\
\tilde{u}_b^2\tilde{s}_b\left(1+\frac{\mathrm{d}\phi}{\mathrm{d}\theta}\right)\sin\phi &= \frac{2\tilde{r}}{We} - \sin^2\phi\ F(\theta,\alpha),\\
\frac{\mathrm{d}\tilde{r}}{\tilde{r}} &= \frac{\mathrm{d}\theta}{\tan\phi},
\end{aligned} \tag{3.8}$$

where the tilde notation indicates dimensionless variables and $We = \rho d_j u_j^2/\sigma$ represents the jet Weber number. These dimensionless equations can be solved numerically to obtain the shape and profile of the leaf's rims, provided that reasonable physical assumptions are applied [138, 139].

3.2.3 Thickness distribution of liquid leaf

The thickness of the liquid leaf is a critical parameter for various applications, prompting extensive experimental [137, 140, 141] and numerical [142, 143] research aimed at characterizing and developing accurate predictive models. These studies indicate that the liquid leaf thickness h is influenced by several factors, including the collision angle of the jets 2α, the jet diameter d_j, the jet velocity u_j, fluid viscosity μ, fluid density ρ, and azimuthal angle of leaf ψ.

Ranz [144] was the first to study the dynamics of a liquid leaf and derive an analytical expression for its thickness by considering an ideal leaf formed by the collision of two identical oblique jets. His approach assumed negligible mechanical energy loss and complete conversion of kinetic energy into surface energy. By applying mass and momentum conservation equations, Ranz derived the following expression for the film thickness:

$$h = \frac{d_j^2}{4r}(1 + 2\cos\psi\cos\alpha). \tag{3.9}$$

A limitation of Ranz's equation became apparent when analyzing collision angles less than 60°. For these smaller angles, the equation predicted nonphysical negative values for liquid leaf thickness for $\psi = 180°$. This inconsistency highlighted the need for further refinement of the model to accurately describe the leaf thickness across all collision angles.

Miller [145] subsequently identified that Ranz's theory did not account for the backward flow in the leaf. By incorporating this consideration, Miller derived an analytical solution for leaf thickness:

$$h = \frac{d_j^2}{4r}\left(\frac{\sin^2\alpha}{1 - 2\cos\psi\cos\alpha + \cos^2\alpha}\right), \tag{3.10}$$

which was validated against experimental results across all collision angles [145].

Later, Hasson and Peck [146] criticized Miller's expression for its low accuracy and proposed a new theoretical model:

$$h = \frac{d_j^2}{4r}\frac{\sin^3\alpha}{(1 - \cos\psi\cos\alpha)^2}. \tag{3.11}$$

They assumed that the liquid leaf had a constant elliptical shape, the flow was inviscid, and the liquid velocity remained constant across the leaf. Their theoretical expression showed good agreement with the experimental results of Miller and Taylor.

However, Ibrahim and Przekwas [147] later argued that assuming an elliptical shape for the leaf was not valid, claiming that Hasson and Peck's analysis could not be used to accurately determine the leaf shape. Instead, they proposed a free and unbounded leaf shape while retaining the assumption of constant fluid velocity along the streamline. Adopting a semi-empirical approach, the initial thickness of the leaf at the point of jet impact was determined based on an experimentally derived expression for the thickness of a liquid leaf formed by a single jet impinging on a wall, as proposed by Naber and Reitz [133]:

$$h_i = \frac{d}{2}\left(\frac{\beta \sin\theta}{\mathrm{e}^{\beta}-1}\right)\mathrm{e}^{\beta(1-\psi/\pi)}, \tag{3.12}$$

where β is a parameter determined from mass and momentum conservation [147]:

$$\cos\alpha = (\frac{e^{\beta}+1}{e^{\beta}-1})\frac{1}{1+(\pi/\beta)^2}. \tag{3.13}$$

From this, the expression for the leaf thickness at a radial position r is derived as:

$$h = \frac{h_i d}{2r\sin\theta} = \frac{d_j^2}{4r}\left(\frac{\beta}{\mathrm{e}^{\beta}-1}\right)\mathrm{e}^{\beta(1-\psi/\pi)}, \tag{3.14}$$

Bush and Hasha [148] further refined Ibrahim and Przekwas's leaf shape assumption by modeling the leaf as a thin, leaf-shaped structure bounded by a thick, stable rim. Their experimental and theoretical work demonstrated that describing the leaf in bounded form yields more convincing results. Yang et al. [149] expanded on Bush and Hasha's ideas by conducting a series of experiments on the characteristics of leaves produced by colliding jets containing a viscous fluid. Their findings revealed that several geometric and hydrodynamic parameters, including the impingement angle, Weber number, and Reynolds number, significantly affect leaf thickness. Kebriaee et al. [139] also presented an improved experimental model for two-jet impingement systems, incorporating the minimum energy principle. Notably, their comprehensive analysis led to the conclusion that Hasson and Peck's expression [146] provides the most accurate prediction for liquid leaf thickness and shape. Figure 3.3 shows the predicted leaf thickness along its vertical central axis ($\psi = 0°$) using Equations 3.9, 3.10, 3.11, and 3.14, for a colliding full angle of $2\alpha = 45°$. The parameter $\beta = 2.8$ was determined numerically by solving Eq. 3.13.

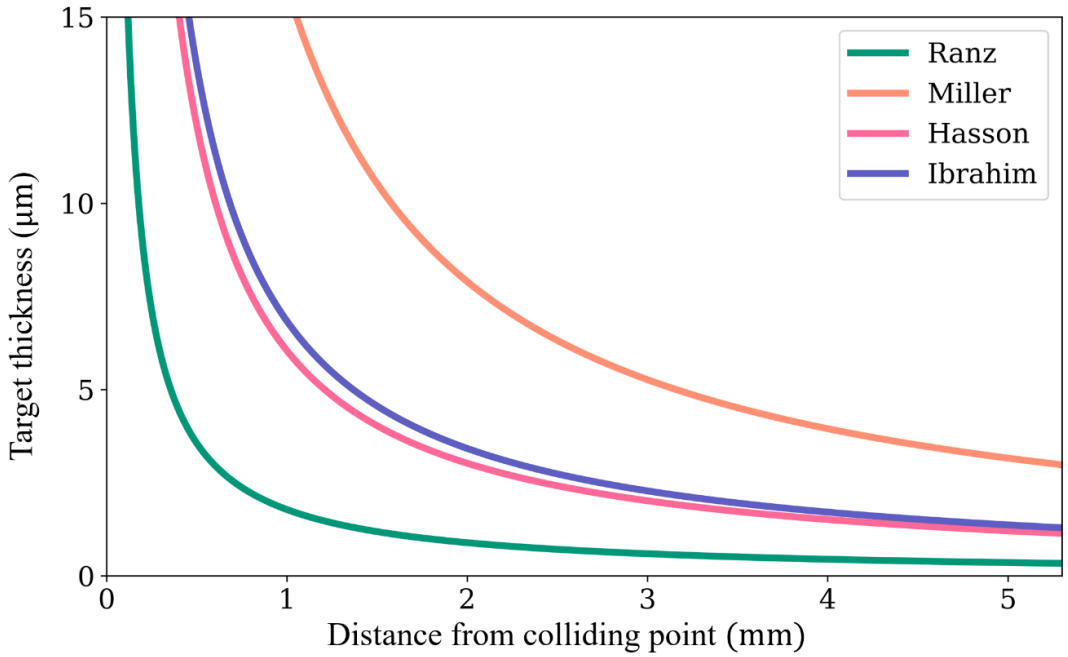

Figure 3.3: Prediction of target thickness using different models. The colliding full angle is $2\alpha = 45°$, the azimuthal angle of the leaf is $\psi = 0°$, and the parameter $\beta = 2.8$.

3.2.4 Breakup and instability

Extensive research on liquid leaf jets over the years has been largely attributed to their tendency to break up into liquid droplets. This disintegration allows the leaf to cover a wide area with relatively uniform droplet distribution, making it beneficial for applications such as pesticide spraying and jet fuel injection. However, in the current application, a stable thin leaf target is needed within a vacuum chamber, ideally without droplet formation. Understanding the mechanisms of jet breakup into droplets is hence essential for designing jets that avoid this behavior.

Depending on the Reynolds number and Weber number of the liquid jet, as well as the angle between the jets, different spray pattern regimes emerge. Bush and Hasha [148] developed a Re-We map outlining seven distinct regimes: oscillating streams, leaves with disintegrating rims, fluid chains, fishbones, spluttering chains, disintegrating leaves, and violent flapping. The precise mechanisms driving the breakup of liquid leaves formed by the impingement of two identical jets are not fully understood, and several theories have been proposed. Figure 3.4 presents a gallery of these liquid leaf patterns.

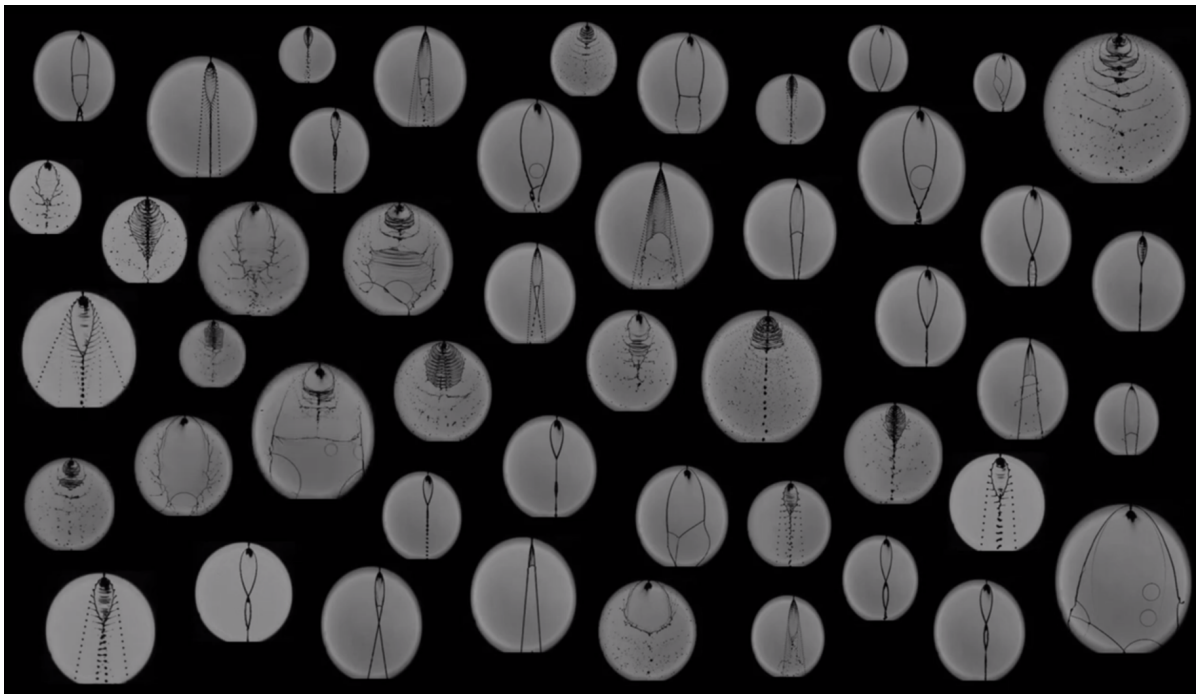

Figure 3.4: Gallery of all kinds of liquid leaves. This figure is adapted from a video by Sina Kashanj and Azadeh Kebriaee [150], retrieved from *https://gfm.aps.org/meetings/dfd-2020/5f5c0684199e4c091e67bc8c*, and licensed under the *Creative Commons Attribution-NonCommercial 4.0 International License.*

Heidmann et al. [151] proposed that the liquid leaf from colliding jets disintegrates due to aerodynamic waves on the leaf surface, with impact waves originating from the collision point further contributing to the breakup. Dombrowski and Johns [152] suggested that breakup is driven by both aerodynamic and hydrodynamic instabilities, with aerodynamic instabilities predominating at higher jet velocities and bigger collision angles. Li and Ashgriz [153] identified two primary breakup scenarios based on capillary instability and Kelvin–Helmholtz instability. This brief literature review underscores the lack of a universally accepted breakup mechanism, with variations in regime maps due to the complexity of the multiphase flow resulting from the jet collisions.

To achieve a stable, smooth leaf with well-defined rims—critical for this study—the Weber number and Reynolds number must remain below specific thresholds. These dimensionless numbers are interrelated, as both are functions of characteristic length and velocity (Reynolds number varies linearly with velocity while Weber number varies quadratically). Additionally, the independent parameters, such as the fluid properties, are inherent to the liquids and are challenging to modify.

3.2.5 Evaporation in a vacuum

Ultra-high power or intensity laser experiments typically require a vacuum environment to eliminate the effects of non-linear interactions [154]. Simultaneously, high-repetition-rate operation demands the continuous renewal of water-leaf targets within the vacuum. However, maintaining water in such an environment is challenging due to its significant evaporation under low pressure, attributed to its high saturated vapor pressure (approximately 31.7 mbar at 25°C). This evaporation imposes a considerable load on the vacuum pumping system. Therefore, it is necessary to calculate the evaporation rate and determine the required pump speed to achieve and maintain a vacuum of at least 1.0×10^{-3} mbar before introducing water into the chamber.

The maximum rate of evaporation, as described by de Boer [155], is as follows: "If we now maintain the temperature of a liquid at a constant value and we take all the vapor away and keep taking it, preventing any molecule from returning to the liquid, we can immediately calculate how much liquid will evaporate per cm^2 and second. This is obviously the maximum rate of evaporation which we can ever attain at the chosen temperature." Building on this concept, Jones et al. [156] derived the maximum rate of water evaporation under the assumption that water molecules striking the surface are not reflected–a typical scenario in a vacuum environment:

$$V_{max} = 0.0583 \cdot P_s \cdot \sqrt{\frac{18}{T + 273.15}}, \tag{3.15}$$

where V_{max} is the maximum rate of evaporation of water in the unit of g/cm^2s, P_s is the saturated vapor pressure of water in Torr, and T is the temperature of water in ℃.

According to Antoine's equation, the saturated vapor pressure is given by:

$$lgP_s = A - \frac{B}{T + C}, \tag{3.16}$$

where the constants are $A = 8.10765$, $B = 1750.286$, and $C = 235.000$, applicable for water temperatures T ranging from 0°C to 60°C. Treating water vapor as an ideal gas, the relationship can be expressed as:

$$pV = nR(T_v + 273.15), \tag{3.17}$$

where p is water vapor pressure of background in Pa, V is the volume of vapor in m^3, n is amount of substance in mol, $R = 8.314$ is ideal gas constant, T_v is the vapor temperature

in ℃. Combining Eq. 3.15, Eq. 3.16, and Eq. 3.17, the volumetric evaporation rate of water in a vacuum can be expressed as:

$$V_{vacuum} = 0.02693 \cdot 10^{(8.10765 - \frac{1750.286}{T+235})} \cdot \sqrt{\frac{18}{T+273.15}} \cdot \frac{S(T_v + 273.15)}{p} \tag{3.18}$$

where S is the surface area of the water-leaf target. For example, with surface area of 0.0075 cm^2, a water temperature T of 20°C, and assuming a vapor temperature T_v of 10°C in the vacuum, the required pump speed to maintain a background pressure of 10^{-3} mbar ($p = 0.1Pa$) is calculated to be 2484 l/s. Given the pumping capacity of 2×2150 l/s in the experimental chamber, the expected vacuum level is approximately $p = nRT_g/V'_{pump} = 5.8 \times 10^{-4}$ mbar. This calculation closely aligns with real observations, where each jet flow rate is 3.0 ml/min and the resulting vacuum pressure ranges from 1.0×10^{-4} to 1.0×10^{-3} mbar, meeting the required vacuum conditions for laser-plasma interaction experiments.

3.3 Generation of water-leaf target

3.3.1 Why colliding jets?

There are various methods for generating water-leaf targets, such as 3D-printed nozzles [157], gas dynamic virtual nozzle [158], converging nozzle [159, 160], and colliding jets [54]. Below is a comparison of these methods, highlighting their respective advantages and limitations.

3D-printed nozzle

Galinis et al. [157] reported a 3D-printed nozzle fabricated using a two-photon polymerization method, capable of producing very smooth and flat leaves of micron thickness in both vacuum and ambient air. Figure 3.5 shows a schematic of the nozzle cross-section and a microscope image of the printed nozzle. This type of nozzle functions similarly to the more commonly utilized colliding jet nozzles. Both methods rely on transverse momentum transfer relative to the jet travel direction to generate a pressure gradient that spreads the liquid into a leaf, as depicted in Fig. 3.5(a). The single orifice design eliminates the need for precise alignment and reduces the risk of clogging by employing a larger nozzle aperture for similar flow rate colliding jets. However, the fixed geometry of the nozzle makes it challenging to adjust the dimensions of the target. Additionally, the

requirement for high resolution and the time-consuming nature of per-piece fabrication is a sickness that was intentionally avoided during the initial tests.

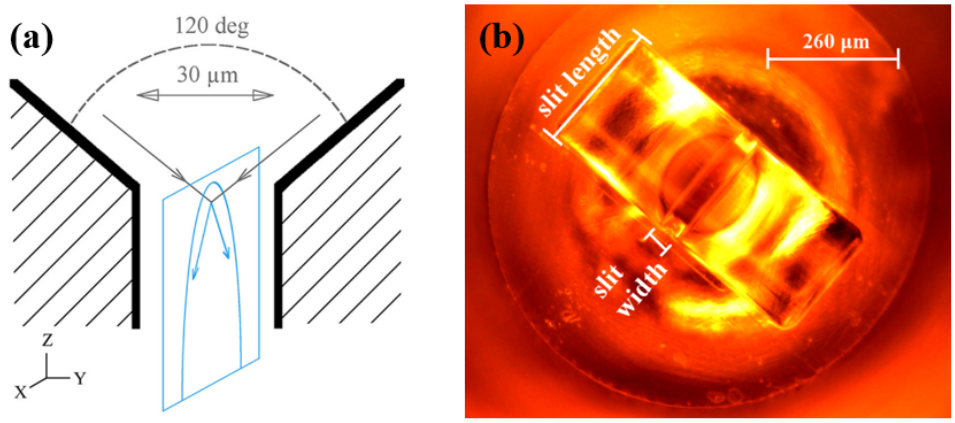

Figure 3.5: (a) Schematic of momentum conservation in a nozzle cross-section. (b) Microscope image of the nozzle with slit dimensions of 260µm × 30 µm. Reprinted from [157], with permission of AIP Publishing.

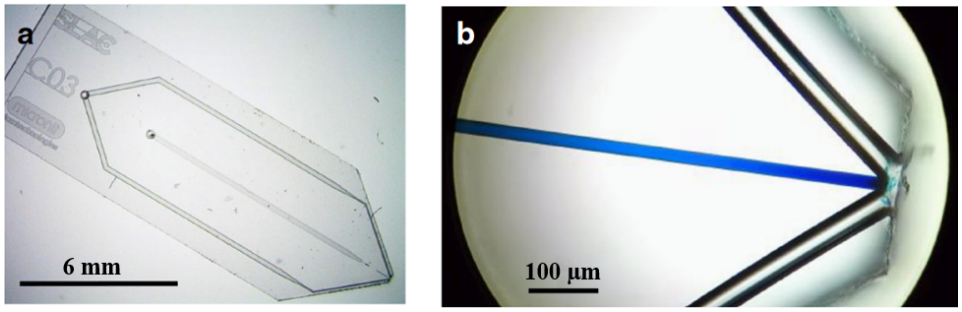

Figure 3.6: (a) Gas dynamic virtual nozzle on the chip. (b) Close-up of the nozzle tip with blue dye introduced into the liquid channel. The figure is copied with permission from Koralek et al. [158], retrieved from *https://www.nature.com/articles/s41467-018-03696-w*, and licensed under the *Creative Commons Attribution-NonCommercial 4.0 International License.*

Gas dynamic virtual nozzle

Koralek et al. [158] developed a gas dynamic virtual nozzle utilizing lithography to produce extremely thin leaves, with a minimum measurable thickness of 16 nm. This gas dynamic virtual nozzle, illustrated in Fig. 3.6, operates by injecting gas through channels set at a 45° angle to a liquid jet (as shown with blue dye in Fig. 3.6(b)). The gas imparts momentum to the liquid, forming it into a classic leaf-like shape. By adjusting the flow rates of both the gas and liquid, it is possible to fine-tune the leaf's thickness

and width-to-length ratios. The presence of gas surrounding the liquid helps maintain higher local pressure, which can enhance the leaf's stability within a vacuum environment. However, the requirement for gas introduces an additional load on the vacuum system, which can be a drawback. An advantage of this design is its flexibility. Liquid can be injected through the gas channels to create a configuration similar to colliding jets, offering greater versatility in leaf formation.

It is worth noting that the liquid leaf is generated at the exit of the chip nozzle regardless of the configuration used. The stability of the liquid leaf is highly dependent on the quality of the chip nozzle tip, which can be easily damaged during laser shots due to the short distance between the laser focus and the chip nozzle tip. Such damage can result in target freezing, which in turn terminates laser-plasma experiments.

Converging nozzle

Converging nozzles have been fabricated through multipart assembly [159] or isotropic etching of glass [160], as shown in Fig. 3.7 and Fig. 3.8, respectively. Converging nozzles function similarly to 3D-printed nozzles by channeling momentum flux perpendicular to the liquid flow, creating leaves that collapse and form orthogonal chains until breakup. The thickness of the exit orifice, which must remain non-zero for structural stability, significantly impacts the nozzle's performance. A longer straight section at the nozzle exit decreases the spanwise to streamwise momentum flux ratio, resulting in a narrower and thicker leaf. If the exit length becomes sufficiently extensive, the leaf transitions into a cylindrical form.

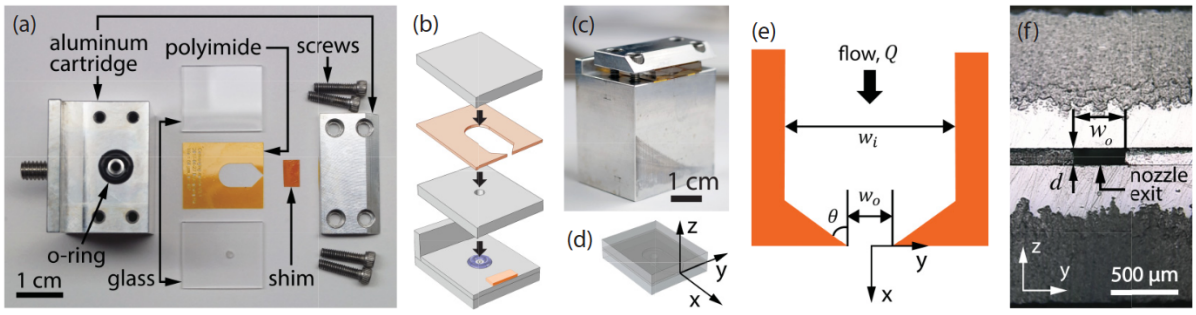

Figure 3.7: Converging nozzles from multipart assembly. (a) Disassembled device. (b) Exploded schematic view of the planar design and connection ports. (C) Fully assembled nozzle. (d) Top portion of assembly and Cartesian coordinates. (e) Microfluidic channel with key geometric parameters. (f) Optical micrograph of the outlet. Reprinted with permission from [159]. Copyright (2024) by the American Physical Society.

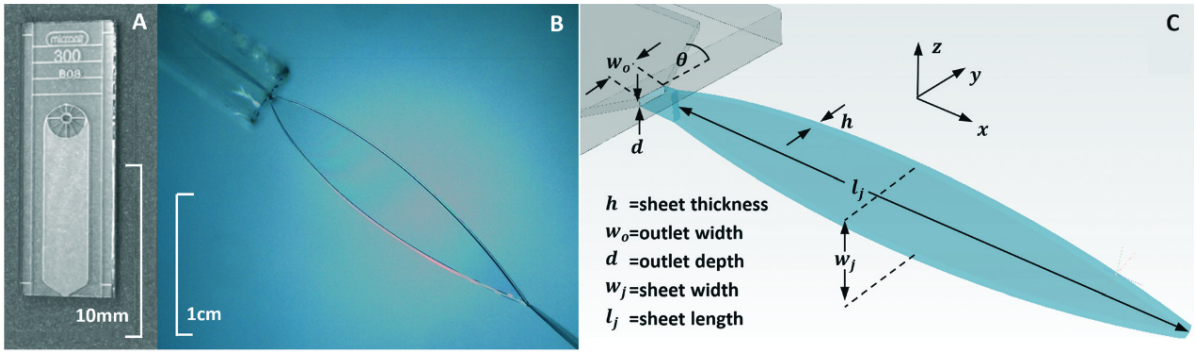

Figure 3.8: Converging nozzles from isotropically etched glass. **A** The converging nozzle's design includes a central inlet channel, positioned within the circular structure below the B08 label. The outlet, positioned at the bottom of the chip, is depicted in **B**, showing a schematic of a liquid leaf projected in a plane perpendicular to the channel. **C** In the xy plane, the converging nozzle's channel produces a leaf in the xz plane, oriented perpendicularly to the channel. The figure is copied with permission from Crissman et al. [160] and licensed under the *Creative Commons Attribution 3.0 Unported Licence.*

Ha et al. [159] and Crissman et al. [160] have both successfully produced sub-micrometer thickness targets using converging nozzles. Although lithography presents a more complex manufacturing process compared to multipart assembly, it provides highly repeatable structures across various sizes, making it ideal for large-scale production and reducing per-part costs significantly. This method, however, is less suited for producing individual prototypes compared to 3D printing, which excels at single-piece production but is less efficient for mass production.

Colliding jets

The colliding jets method, illustrated in Fig.3.9, is among the simplest and most cost-effective techniques to fabricate. It involves two cylindrical jets emerging from aligned tubes that collide, spreading the liquid into a leaf. This method has been extensively studied both experimentally [136,148] and theoretically [146,147,161]. Ekimova et al. [54] reported achieving sub-1 µm thick leaves using this geometry for the first time. In this configuration, the leaf can expand freely, resulting in a more rounded shape. However, challenges include precise alignment and the potential for fluctuations in leaf position or thickness due to pulsations in the liquid flow.

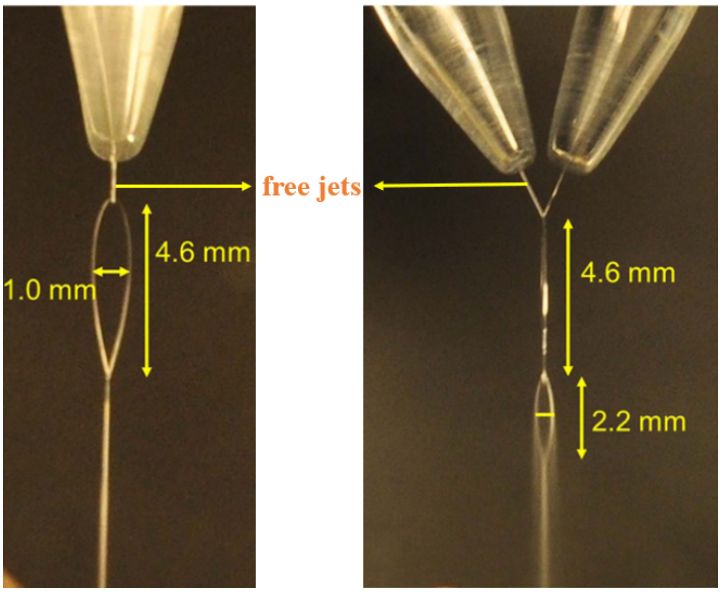

Figure 3.9: Colliding jets. The figure is copied with permission from Ekimova et al. [54] and licensed under the *Creative Commons Attribution 3.0 Unported Licence.*

Off-chip collision nozzle

An off-chip collision nozzle is a preferred approach as it ideally combines the advantages of chip nozzles and colliding jets. As shown in Fig. 3.10, this configuration features a pre-aligned geometry on the chip, eliminating the need for post-alignment, and the distance l from the collision point to the chip provides self-protection. While current photolithography techniques can meet the initial requirements, this type of nozzle is particularly sensitive to the quality of the tip, which can lead to instability in water leaf target generation. Hoffman et al. [162] noted that such nozzles are prone to failure, which impacts the consistency of the water leaf targets produced.

Figure 3.10: Schematic of an off-chip nozzle. The liquid channel is displayed in blue. The jets collide at an angle of 2α and a distance of l after exiting the chip.

Summary

The ability to position the jets freely reduces the risk of damage and maintains the integrity of the water-leaf targets, making it the superior choice for consistent and stable target generation in high-repetition-rate laser-driven ion acceleration. In summary, no single method for generating water-leaf targets is without drawbacks, each presenting unique advantages and limitations at present. The stability of the targets is a critical factor for high-repetition-rate proton source generation, particularly during laser-plasma interactions. Methods such as 3D-printed nozzles, gas dynamic virtual nozzles, and converging nozzles often generate targets close to the nozzle tip, making them vulnerable to damage during laser shots. This vulnerability can significantly impact the consistency and stability required for high-repetition-rate operations. Although Treffert et al. [57] employed the third consecutive leaf generated by a converging nozzle for laser-plasma experiments, this approach results in a thicker and smaller target, which is less ideal for ion acceleration. In contrast, the colliding jets method, owing to the large distances between targets and nozzles, has a good chance of avoiding laser damage to the nozzles. Despite the high alignment requirements of this method, which can be managed using one or two linear piezo stages (SLC-2445, SmarAct GmbH), it remained the most favorable option.

3.3.2 Why water?

Several liquids were evaluated for generating water-leaf targets, including ethylene glycol, aqueous glycerol at 64% volume fraction, isopropyl alcohol, and water. Table 3.1 details the physical properties of these liquids at 20°C. In general, high kinematic viscosity contributes to target stability, low surface tension results in larger targets, and low saturated vapor pressure is advantageous for maintaining vacuum conditions.

Liquids	Physical properties at 20°C		
	Kinematic viscosity (mm^2/s)	Surface tension (mN/m)	Vapor pressure (mmHg)
Water	1.0	72.8	17.5
Ethylene glycol	18.6	48.5	0.06
Isopropyl alcohol	3.0	21.4	32.4
Aqueous glycerol (64%)	18.3	68.3	12.2

Table 3.1: Physical properties of liquids

Isopropyl alcohol forms large and stable targets in ambient air but has a high saturated vapor pressure, making it unsuitable for vacuum environments. Aqueous glycerol (64% volume fraction) possesses a high kinematic viscosity similar to ethylene glycol, tending to generate stable targets. However, in vacuum conditions, it often forms bubbles on the catcher's surface, complicating drainage, and its vapor condenses within the chamber, leading to carbon contamination.

Ethylene glycol, characterized by low saturated vapor pressure, high kinematic viscosity, and relatively low surface tension, has been used for liquid-plasma interaction [55, 58, 154, 163]. Nevertheless, its carbon-based composition poses contamination concerns, eventually hindering long-term operation. Water, although less stable and having a higher evaporation rate, eliminates the issue of carbon-containing debris, making it suitable as a starting point in this study.

3.3.3 Setup

The water-leaf target is generated by the precise collision of two water jets. The water-leaf target system is composed of two primary components: the outside chamber and the inside chamber. Both components are designed to fulfill two critical requirements: producing a flat, stable liquid target with a thickness of just a few or sub micrometers and operating under high vacuum conditions (approximately 10^{-3} mbar). This section describes the final version of the system, excluding the extensive development process involved over the years.

Outside chamber

A schematic of the external chamber components is shown in Fig. 3.11. Central to the water-leaf target system is a High-Performance Liquid Chromatography (HPLC) pump (LC-40D, Shimadzu Deutschland GmbH). This pump features a parallel dual micro plunger (10 µl) design, which ensures low pulsation and a stable baseline. It operates at a maximum pressure of 440 bar, with flow rates ranging from 0.1 µl/min to 10 ml/min, and an accuracy of ±1% or ±2 µl/min. Clean water from the reservoir #1 is continuously fed into the pump through a filter with a pore size of 2 micrometers and then transported to a degasser (DGU-403, Shimadzu Deutschland GmbH). The degasser removes dissolved air from the water, minimizing the pulsation of water flow and ensuring the reproducibility of the injection volume.

The water flow is subsequently divided into two arms by a three-way connector, with

adjustment valves in each arm to fine-tune the flow resistance and ensure an equal flow rate in both arms. The water is then directed to the internal chamber via a vacuum feed-through and subsequently to the nozzles. To further minimize pulsation in the tubing and, consequently, in the water jets, a pulsation damping system is employed along with a set of 1/16-inch PEEK tubing, which has a decreasing inner diameter from 500 micrometers to 50 micrometers. Additionally, operating the HPLC pump at a pressure range of 100 to 200 bar helps minimize the pulsation.

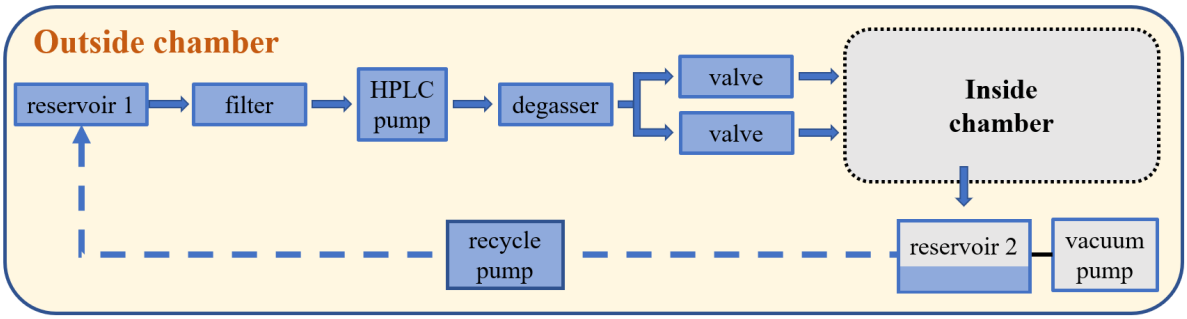

Figure 3.11: Schematic of the outside chamber components of the water-leaf target system. Arrows indicate the direction of water flow, with blue shading representing the water, gray shading denoting vacuum areas, and yellow shading representing air. The recycle pump, which allows for infinite operation, is not currently installed, as reservoir 2 provides more than 10 hours of operation, which is sufficient for the present experiments.

The reservoir #2 is designed to collect the water exiting the chamber. A vacuum pump evacuates this reservoir to ensure continuous and effective water collection. Maintaining the correct pressure inside the reservoir is crucial for proper water collection. Excessive pressure inside the reservoir can cause water backflow, leading to the freezing of the target. Conversely, if the pressure is too low, increased evaporation and heat loss can cause the formation of a thin ice tower in the reservoir, affecting long-term operation. To address these issues, experimental tests indicate that maintaining a pressure of a few mbar within the reservoir is optimal. The reservoir, with a volume of 2 liters, supports over 10 hours of operation at an injection rate of 3 ml/min, which is sufficient for current experimental campaigns. Theoretically, water collected in the reservoir can be emptied and refilled into the initial reservoir without interrupting the jet or vacuum operation by a recycle pump, allowing the system to operate indefinitely.

Alongside the water circuit components, electronic control devices were designed for remote computer operation, such as the power switch for the HPLC pump and heating and temperature control for the catcher.

Inside chamber

The water-leaf setup sits in the center of the LION experimental chamber. Laser pulses are directed from left to right between two supporting rods, with a movable microscope system on the right side for initial alignment between the laser focus and the target. Also on the right side, a permanent magnet quadrupole (PMQ) can be inserted to focus proton bunches. Integrating the new water-leaf target system into the existing components presented challenges, as a compact configuration was needed, for example focusing proton bunches at the energy of 10 MeV, requires a distance of only 40.5 mm from the proton source (the water leaf) to the entrance of the PMQ.

Figure 3.12(a) illustrates the water-leaf setup inside the chamber. Two nozzles are fixed at a few mm distance and a 45-degree colliding angle by a custom-designed holder. One nozzle is mounted on a motorized linear piezo stage, allowing precise alignment with the opposing nozzle. A top view of the water-leaf generation, perpendicular to the jet plane with no misalignment between the jets, is shown in Fig. 3.12(b). In contrast, slight misalignment of the jets results in rotation of the water leaf, as seen in Fig. 3.12(c). Below the water-leaf target, a heated catcher is positioned to remove water from the chamber through drain tubing. This catcher is mounted on a motorized 3-axis stage, ensuring precise alignment with the water-leaf target. The complete water-leaf target is aligned precisely with the ATLAS-3000 laser focal spot using a six-axis hexapod.

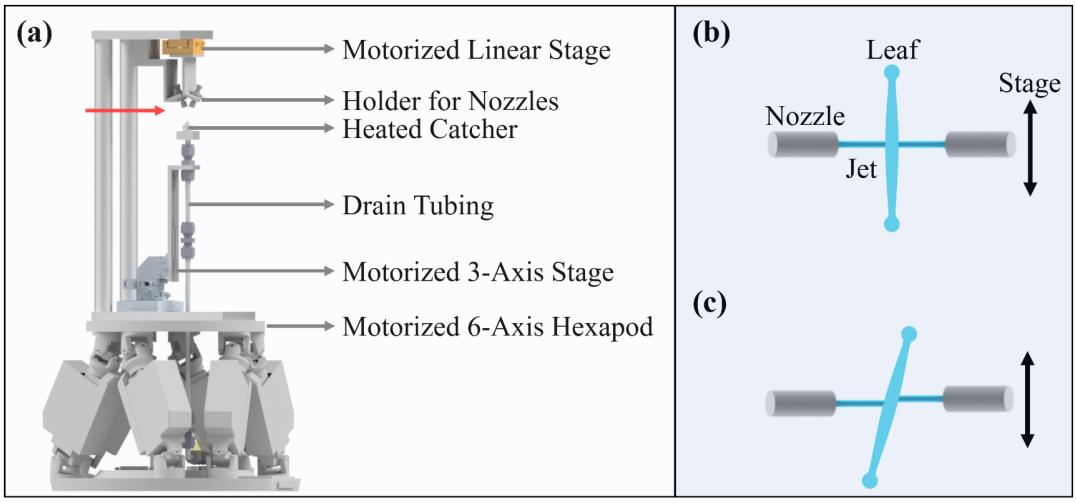

Figure 3.12: (a) Setup of water-leaf target system inside the chamber without tubing lines from HPLC pump. The red arrow indicates the laser propagation direction. (b) and (c) provide the top view of water-leaf generation with proper alignment and misalignment of the two jets, respectively.

Among the components, the catcher design is a creative approach that offers a much more compact solution. Inspired by 3D printing technology, it functions similarly to a "hotend", as shown in Fig. 3.13. This heated catcher assembly includes a nozzle with a changeable opening (with 0.6 mm currently in use), a 40W ceramic heater, a temperature sensor for feedback control, a connector for the drain tubing, and an aluminum block that integrates all components. Experience has shown that maintaining the catcher at temperatures between 100°C and 120°C is effective in preventing the water-leaf target from freezing.

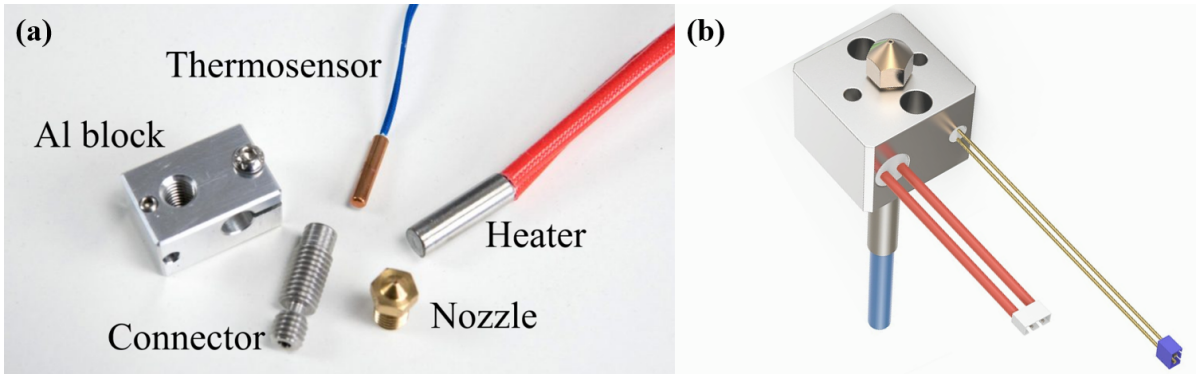

Figure 3.13: Design of the catcher inspired by 3D printing technology. (a) Disassembled view of the 3D printer hotend components. (b) Schematic showing the assembled hotend used as the heated catcher.

3.3.4 Water-leaf in LION chamber

Figure 3.14 displays a close view of the first water-leaf target in the LION chamber from the side and front. Two 50 µm in diameter water jets, each flowing at a rate of 1.5 ml/min, collide at a full angle of 45 degrees. The first water leaf measured approximately 1 mm in length and 0.3 mm in width, with a thickness ranging from 3 µm to 15 µm. This thickness profile will be explained in more detail in the next section. The red dot in Fig. 3.14(b) indicates the laser-target interaction point at a thickness of approximately 5 µm. Additionally, the catcher is maintained at a temperature between 100℃ and 120℃ to prevent the water-leaf target from freezing when operating in a vacuum.

In short, the water-leaf target system operated robustly in a vacuum for over 10 hours. In addition, the incorporation of the hexapod and linear stages provided a high degree of freedom to control the target's position prior to the next shot. This adaptability allowed for comprehensive scans of the target position, including movements along the laser axis, vertical adjustments (varying target thickness), and corrections for rotational variations

between shots. Such flexibility was crucial in identifying the optimal interaction position, achieving high proton energy, high particle yield, and stable operation.

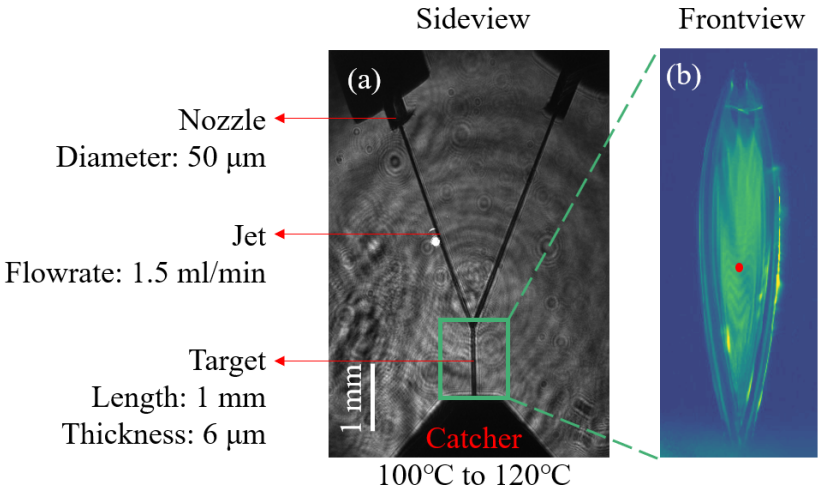

Figure 3.14: Shadowagraphy of water-leaf target in LION chamber. (a) Side view of the water-leaf target. (b) Zoomed-in front view.

3.4 Thickness measurement of water leaf target

Target thickness is a critical parameter in laser-driven ion acceleration, significantly influencing the maximum ion energy and acceleration mechanism. For water-leaf targets intended for proton acceleration with thicknesses of a few micrometers in a vacuum, implementing a thickness measurement system with appropriate resolution is essential. However, this is challenging due to the free-standing nature of water-leaf targets, which precludes contact measurements, and the presence of a thick rim that hinders side imaging techniques.

To address these challenges, white light reflection interferometry is employed for thickness measurement of the water-leaf target [134, 164]. This method involves directing white light onto the film at an angle θ, resulting in interference between reflections from the front and back surfaces. The interference pattern in the reflected light spectrum is then analyzed to determine the film thickness. The thickness h of the film is calculated using the following formula:

$$h = \left[\frac{2(n_1^2 - \sin^2\theta)^{1/2}}{\lambda_1} - \frac{2(n_2^2 - \sin^2\theta)^{1/2}}{\lambda_2} \right]^{-1}, \tag{3.19}$$

where λ_1 and λ_2 are the wavelength of any two adjacent peaks, and n_1 and n_2 are the refractive indices of the water leaf at λ_1 and λ_2, respectively.

In practice, the thickness of the water-leaf target was measured at multiple positions along the vertical central axis. The thickness profile was then fitted using the model proposed by Taylor [137], where thickness h is inversely proportional to the distance r from the colliding point:

$$h = \frac{K(\alpha, \psi)}{r + r_0}. \tag{3.20}$$

Here, $K(\alpha, \psi)$ is a geometry-related parameter dependent on the jets' collision half angle α and azimuthal angle ψ on the leaf. For a fixed experimental setup, $K(\alpha, \psi)$ remains constant and can be treated as a fitting parameter. The parameter r_0 serves as a free fitting parameter to adjust the actual distance from the colliding point, which is challenging to pinpoint precisely.

While theoretically only two measurements are required to determine the thickness, multiple measurements were conducted for enhanced precision. Figure 3.15 presents the results, with fitted values of $K(\alpha, \psi) = 3273 \pm 24$ and $r_0 = 627 \pm 6$ µm. The measured thicknesses range from 3 µm to 20 µm, depending on the vertical position. The associated error is within a few percent (up to 5%), primarily due to the 25 µm spot size of the white light source used on the water-leaf target.

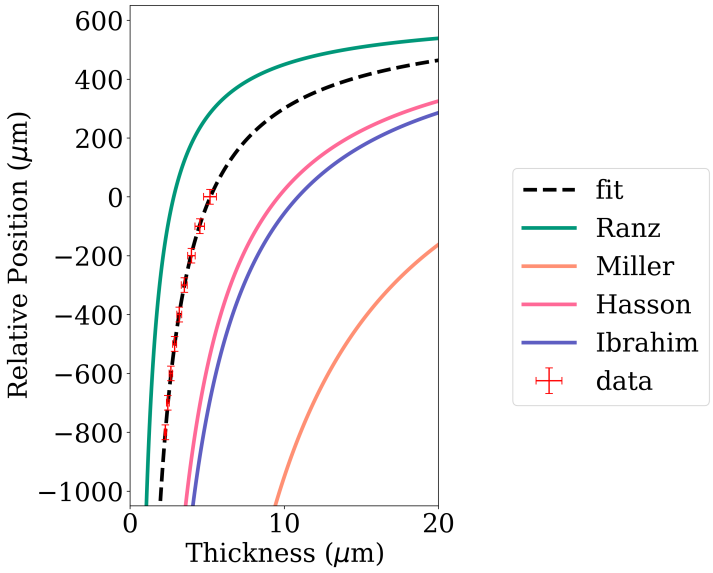

Figure 3.15: Comparison of theoretical predictions of thickness profiles along the vertical median axis of a waterleaf target with measured data recorded by M. Bachhammer.

Unfortunately, despite the Hasson and Pike expression being considered the most accurate theoretical prediction, the results deviate from all theoretical predictions discussed in Section 3.2.3. This discrepancy may be partly due to the data being recorded in a vacuum, which results in a thickness reduction of approximately 10% compared to measurements in air [165].

It is noteworthy that the initial focus of the study was on stabilizing the laser-plasma interaction and optimizing proton performance, rather than measuring thickness for every experimental campaign. According to the theoretical model, the thickness along the vertical central axis depends solely on the distance from the collision point, assuming a consistent setup, and should not exhibit significant day-to-day variations. Therefore, the thickness can be inferred from the profile shown in Fig. 3.15 with an estimated error of approximately ±25 µm in the relative position, leading to a total error of up to 10%.

3.5 Challenges and solutions

3.5.1 Evaporation

The water-leaf target system is designed to operate effectively within a background pressure range of 1.0×10^{-4} to 1.0×10^{-3} mbar, which is suitable for laser-plasma experiments. However, maintaining water in a vacuum environment presents significant challenges due to the high saturated vapor pressure of water, leading to considerable evaporation under low-pressure conditions. While this evaporation can be managed by the vacuum pumping system according to the calculation in section 3.2.5, it imposes a substantial load on the system's capacity.

According to Eq. 3.15 and Eq. 3.18, several strategies can be employed to mitigate evaporation: lowering the temperature of the injected water, increasing the background pressure, and reducing the surface area of the water leaf. Each approach, however, has limitations. Reducing the temperature of the injection water can lead to freezing while increasing the background pressure is not conducive to optimal laser-plasma interactions. A more practical solution involves minimizing the size of the water-leaf target by adjusting the flow rate, although this has disadvantages as well.

The setup employs a flow rate of 3 ml/min in total (each jet flowing at a rate of 1.5 ml/min) to produce a water-leaf target with dimensions of 1 mm in length and 0.3 mm in width. Positioning the catcher at the end of the first leaf significantly reduces water evaporation in a vacuum environment. While not currently implemented, the potential

incorporation of a liquid nitrogen-filled cold trap has been considered. Such a trap would act as a cryopump, effectively freezing water vapor onto its surface, potentially enhancing the vacuum level by one to two orders of magnitude. However, given that the current vacuum levels in the experimental chamber are sufficient for water-leaf target experiments, and considering the added complexity to the setup, the cold trap was not considered necessary. Its potential benefits are noted for future optimizations if required. These combined approaches ensure the stability of the water-leaf target while maintaining the requisite conditions for high-quality laser-plasma experiments.

3.5.2 Freezing

Managing liquids in high vacuum environments is particularly challenging due to the significant impact of these extreme conditions. Unlike solids and gases, liquids are especially unstable in high vacuum, as they are typically below the triple point on the phase diagram under these conditions. For instance, water, commonly used as a target material, faces the risk of freezing in vacuum conditions. As shown in Fig. 3.16, the triple point of water is at 0°C and 6.1 mbar, marked by the red dot at the intersection of the phase boundaries, indicating that liquid water cannot exist in equilibrium below approximately 6 mbar.

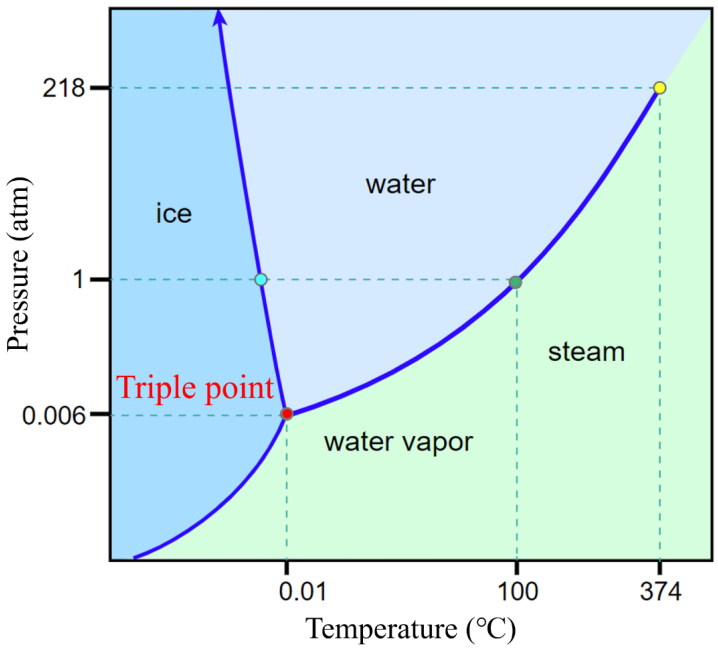

Figure 3.16: Phase diagram of water. The figure is adapted from [166] and accessed on 06/08/2024.

While cylindrical jets can maintain stability during transit through a vacuum chamber without requiring equilibrium conditions [167, 168], the high surface tension of water poses challenges for maintaining stable flat leaves (water-leaf targets). These flat leaves are susceptible to Rayleigh instabilities, which can lead to droplet formation [137]. This instability results in significant spray generation from the leaf rims, which tend to freeze in vacuum conditions, initiating a cascade of ice buildup. The freezing process can ultimately clog the nozzles, halting the operation of the water-leaf target in a vacuum. Resolving this issue typically requires venting the chamber and restarting the system, a process that can take 30 minutes to an hour.

Ensuring the stability of a water-leaf target in high vacuum environments requires precise control of various parameters to mitigate the risk of freezing and maintain continuous operation. A key strategy for achieving this is heating the catcher to prevent ice formation. As mentioned before, maintaining the catcher at temperatures between 100°C and 120°C proved highly effective in preventing the water-leaf target from freezing. Additionally, effectively guiding the water out of the chamber is crucial. A reservoir that maintains a pressure of a few mbar has proven to be optimal for this purpose. The combination of a heated catcher and the pressure-regulated reservoir significantly reduces the likelihood of freezing, ensuring stable operation unless unforeseen issues arise, such as misalignment of jets, heater malfunctions, or unexpected pulsations from the HPLC pump.

These measures contribute to the stability and reliability of the water-leaf target in high vacuum conditions, thereby facilitating successful laser-plasma interactions. However, laser shots incident on the leaf resulted in a detuning effect, which became more pronounced with increased laser energy but remained manageable. This detuning was monitored by tracking reflections from the target of a Continuous-Wave (CW) laser that shared the same optical path as the ATLAS-3000, allowing for adjustments to the nozzle position using linear stages to compensate. In addition, the detuning was partly attributed to flow dynamics, which was significantly suppressed by reducing the distance between the nozzles.

3.5.3 Vapor erosion

Another challenge is vapor erosion, which arises from the substantial water vapor generation due to evaporation in a vacuum environment. To protect sensitive beamline and laser optics from potential damage caused by this water vapor, an optical window made of TurboFilm (Baader Planetarium GmbH) with a thickness of 12 µm was installed

between the beamline and the experiment chamber. The thinness of the optical window ensures that the B-integral remains negligible, thereby maintaining the quality of the laser beam profile. However, due to its delicate nature, the installation process of the TurboFilm requires considerable care. Specifically, ensuring the flatness and tension of the film during installation necessitates the coordination of four hands to stretch the film and another two hands to screw the frame tightly. The optical window is strategically positioned at the entrance of the chamber before the 280 mm diameter laser beam is focused. In this configuration, there are no concerns regarding direct laser damage to the optical window or indirect debris damage from laser-target interaction.

Moreover, the vacuum pumping system, particularly the pre-pump, is not inherently designed to handle large quantities of water vapor. Thus, it is important to keep the pre-pump running continuously for self-cleaning, even after the experiment has ended. This practice helps to prevent water vapor from accumulating within the pump, ensuring efficient operation and longevity of the pump.

3.5.4 Electromagnetic pulse

The management of ElectroMagnetic Pulses (EMPs) presents a final challenge. EMPs generated during laser-plasma interactions can induce currents and voltages that disrupt the normal operation of electronic systems, potentially causing malfunctions or permanent damage. EMPs primarily impact systems near the laser-target interaction point, where the pulse strength is largest. This can interfere with motors, heating devices, temperature sensors for the catcher, as well as cameras and other remote-control devices essential for monitoring and adjusting experimental parameters.

To mitigate EMP effects, several protective strategies are implemented. Shielding sensitive electronics in conductive materials is highly effective; encasing components within conductive enclosures, such as Faraday cages, attenuates EMP fields and shields internal electronics. Figure 3.17 illustrates this approach with braided metal fabric and metal boxes protecting cables and devices from EMP influence. Filters such as ferrite cores on cables further block high-frequency EMPs, preventing them from entering and damaging sensitive components. Additionally, proper grounding of electronic systems further aids in dissipating EMP-induced currents safely into the ground, thereby reducing the potential for damage.

Maintaining a distance between sensitive equipment and the laser-target area also reduces EMP exposure. Using EMP-resistant electronic components enhances system robustness, ensuring reliable operation under high-intensity laser-plasma conditions.

Together, these strategies improve the resilience of the water-leaf target system, supporting continuous operation in high-EMP environments.

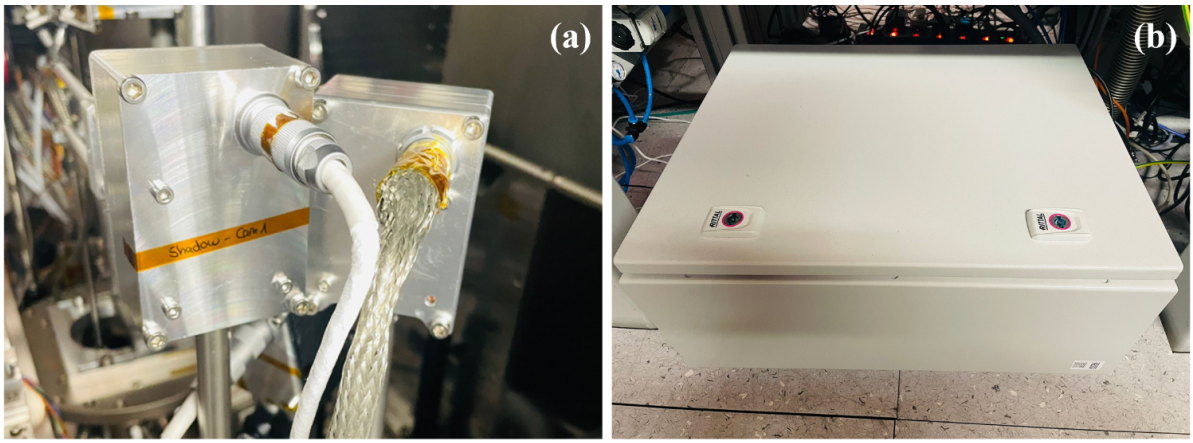

Figure 3.17: Examples of EMP protection shielding strategy. (a) Cameras housed in aluminum boxes, with the camera on the right additionally shielded by braided copper sleeving, while the left camera is unshielded. (b) Electrical cabinet providing enclosure and protection for sensitive electronics.

Chapter 4

Methods

In this chapter, the experimental methods and apparatus utilized in this study are introduced. The chapter begins with a description of the ATLAS-3000 high-power laser system. Following this, a detailed account of the LION experimental chamber is provided. Additionally, ion diagnostics used in the experiments are described.

4.1 ATLAS-3000 laser system

The Advanced Titanium: sapphire LASer (ATLAS) is located at the Centre for Advanced Laser Applications (CALA), Garching, Germany [169]. It is designed to deliver a final compressed energy of 60 J and a pulse duration of 20 fs, i.e., 3000 TW peak power with a 1 Hz repetition rate (the so-called ATLAS-3000). This makes it one of the most powerful PW laser systems globally. However, during the period of this thesis, the pulse energy on target was limited to below 10 J and a current pulse duration of 27 fs (300 TeraWatt–TW), which applied to all experiments discussed in Chapter 5.

4.1.1 Laser setup

A schematic layout of the ATLAS-3000 laser system is shown in Fig. 4.1. The system's frontend comprises an actively mode-locked Ti: sapphire oscillator, generating 20 fs pulses at an 80 MHz repetition rate, with each pulse carrying a few nanojoules of energy. These pulses are subsequently directed through a Pockels cell operating at 10 Hz for pulse selection, before entering a multi-pass amplifier, designated as the 'Booster'.This stage enhances the laser pulse contrast on the nanosecond timescale [170], raising the energy to 250 µJ after passage through a saturable absorber. Following this initial amplification, the pulses undergo temporal stretching to a duration of 800 ps in the main stretcher.

To compensate for higher-order dispersion and ensure optimal pulse compression after amplification, a DAZZLER acousto-optic programmable dispersive filter [171] is

implemented at the stretcher's exit. The stretched pulses are then amplified in a regenerative amplifier, referred to as 'Regen' [172], which serves to stabilize energy fluctuations from preceding stages. Within the regenerative cavity, a MAZZLER acousto-optic programmable gain control filter [173] is employed to maintain uniform amplification across a broad spectral range, thereby mitigating gain narrowing effects.

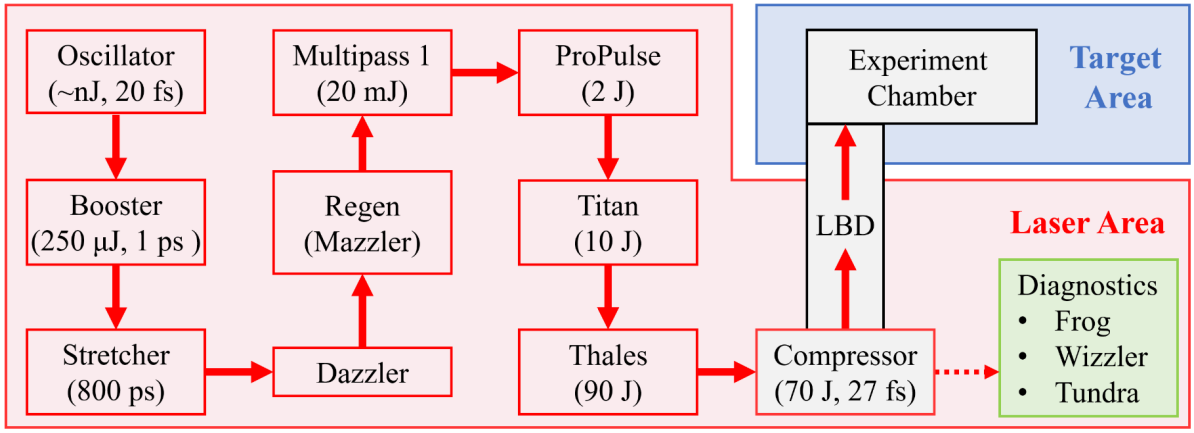

Figure 4.1: Schematic representation of the ATLAS-3000 laser system's primary components. The diagram is color-coded to delineate distinct functional areas: red denotes the laser generation and amplification stages; blue indicates the target interaction region; green represents the laser diagnostics section; and gray signifies the vacuum beamline, including the Laser-Beamline Delivery (LBD) system.

Subsequent amplification stages consist of a series of multi-pass amplifiers, including 'Multipass 1', 'ProPulse', 'Titan', and 'Thales.' This amplification chain culminates in a pre-compression pulse energy of 90 J at a 1 Hz repetition rate.

The amplified pulses are subsequently directed into a vacuum chamber housing a grating compressor, where they are temporally compressed to a duration of currently 27 fs (FWHM), centered at a wavelength of 800 nm. This compression process results in a final pulse energy of up to 70 J, representing a significant portion of the pre-compression energy. Following compression, the beam can be directed either to diagnostics outside the vacuum for comprehensive pulse characterization (detailed in Section 4.1.2) or delivered into the experimental chamber (described in Section 4.2) via the Laser Beamline Delivery (LBD) system. For a more comprehensive description of the ATLAS system, readers are referred to [169].

The ATLAS-3000 system is engineered to support a diverse array of scientific applications, leveraging its high-power, ultra-short pulse capabilities. These applications span

multiple scientific research domains, including research in radiobiology and radiation oncology, generation of ultra-low emittance electron beams for high-brightness X-ray sources, investigations into nuclear processes, and studies in high-field Quantum Electro-Dynamics (QED). Within this broad scientific landscape, the focus of this thesis is on LION acceleration utilizing water-leaf targets at CALA.

4.1.2 Laser diagnostics

Following pulse compression, the laser pulses are directed out of the vacuum chamber for diagnostic analysis. At this stage, a Wizzler device from Fastlite [174], which utilizes Self-Referenced Spectral Interferometry (SRSI) technology, is used to measure the group delay of the pulse's spectral components. This information is fed back to the Dazzler (located in the stretcher) to optimize the spectral phase and achieve minimal pulse duration. The final pulse duration is measured using a Grenouille from Swamp Optics [175], a simplified implementation of Frequency-Resolved Optical Gating (FROG). Figure 4.2 presents a representative measurement of an ATLAS-3000 pulse, with an FWHM duration of 28 fs, obtained from both the Wizzler and Grenouille diagnostics.

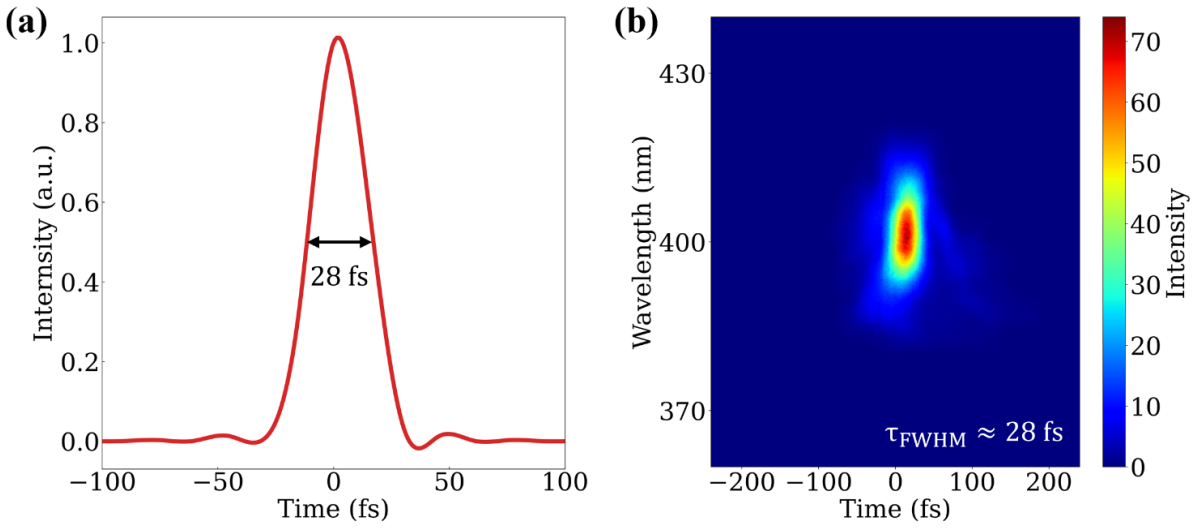

Figure 4.2: Pulse duration of the ATLAS-3000 laser pulse recorded from (a) Wizzler and (b) Grenouille - second harmonic generation (SHG) map.

To evaluate the temporal contrast of the laser pulse, which is critical for high-intensity laser-plasma interactions, a commercial third-order autocorrelator, TUNDRA from Ultrafast Innovations [176] is employed. This instrument enables the measurement of

pulse contrast over a dynamic range spanning 11 orders of magnitude, with a temporal window extending to 2 ns pre-pulse delay. Figure 4.3 illustrates a typical autocorrelation curve for the ATLAS-3000, normalized to the peak intensity achieved during current experimental campaigns. The combination of these advanced diagnostic tools allows for comprehensive characterization and optimization of the laser pulse parameters, ensuring the delivery of high-quality, ultra-short pulses for subsequent experiments.

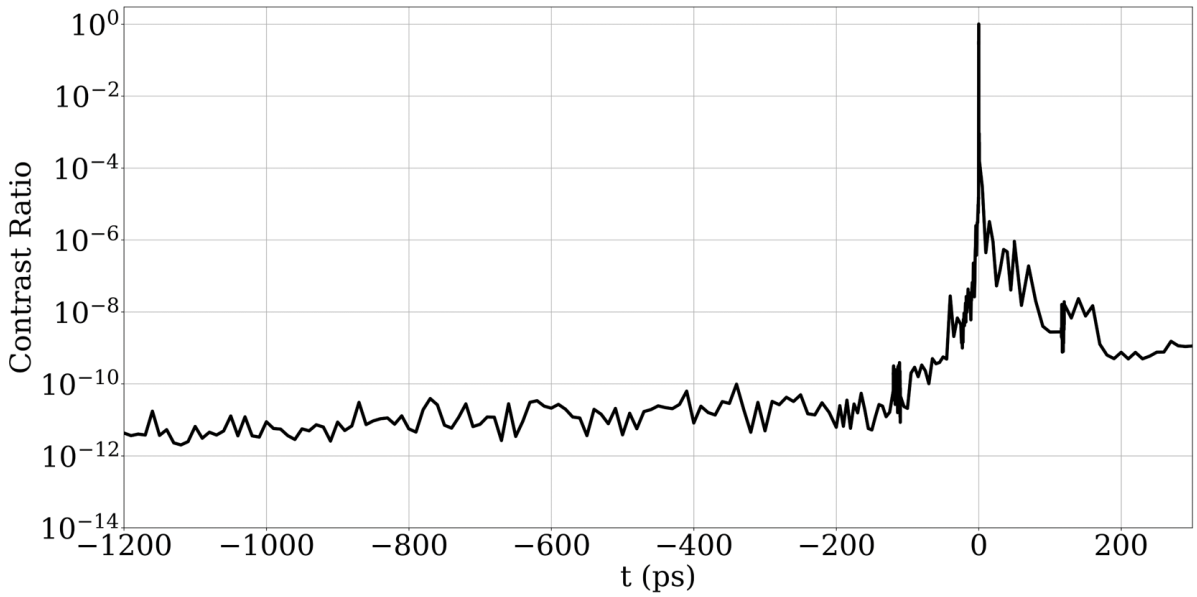

Figure 4.3: Third order scanning autocorrelation (TUNDRA, Ultrafast Innovations) of the ATLAS laser system on 2023.05.05.

4.2 LION chamber

4.2.1 Overview

Figure 4.4 presents a schematic representation of the LION chamber configuration, depicting a subset of the key components for clarity. The high-intensity laser pulses generated by the ATLAS-3000 system are directed to the LION chamber via the LBD system, which maintains beam quality and alignment from the laser source to the interaction region. The measured transmission efficiency from the compressor to the laser focus is approximately 60%.

Upon entering the LION chamber, the laser beam undergoes two reflections via high-reflectivity tower mirrors before being focused onto a Water-Leaf Target (WLT) at an oblique incident angle of 6.8°. The focusing is achieved using an f/5 glass Off-Axis

Parabola (OAP) with a focal length (f_L) of 1.5 m and an off-axis angle of 20°. This configuration allows for the reflection and focusing of the beam to near-diffraction-limited focal spot sizes, approaching approximately 5 µm. The focal spot position within the target chamber is designated as the Target-Chamber-Center (TCC), serving as the primary interaction point for laser-plasma experiments.

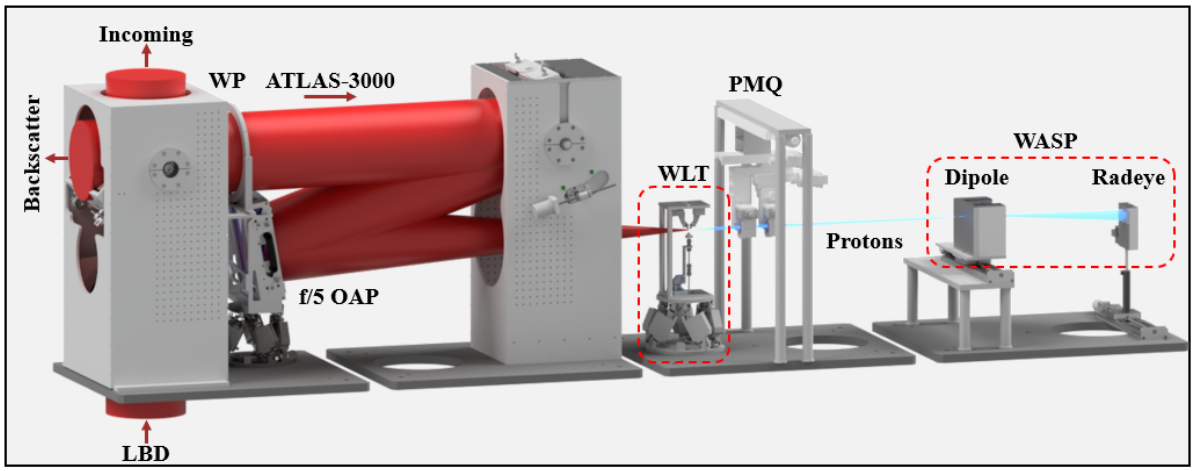

Figure 4.4: Schematic representation of the LION chamber configuration. Key components are labeled: WP (quarter-Wave Plate for polarization control), OAP (Off-Axis Parabola for beam focusing), WLT (Water-Leaf Target), PMQ (Permanent Magnet Quadrupole for potential beam manipulation), and WASP (Wide-Angle SPectrometer for particle diagnostics). For clarity, only a subset of the installed laser diagnostics is shown. The entire experimental apparatus is integrated into a control and data acquisition system, enabling real-time monitoring of laser and plasma parameters, rapid adjustment of experimental conditions, and preliminary processing of acquired data.

To facilitate precise control over the laser polarization state, a removable quarter-wave plate is strategically positioned between the tower mirrors. This optical element enables the conversion of linearly polarized laser light to circular polarization when necessitated by specific experimental protocols, providing flexibility in manipulating the laser-plasma interaction conditions.

The experimental setup also incorporates a Permanent Magnet Quadrupole (PMQ) [177], designed for potential future applications in proton bunch focusing and manipulation. While this component offers promising capabilities for advanced beam control, it is not utilized in the studies presented in this thesis, which focus primarily on the fundamental laser-plasma interaction dynamics and ion acceleration mechanisms.

For comprehensive diagnosis of the accelerated proton bunches, the system employs an automated online Wide-Angle Spectrometer (WASP) [178, 179]. This diagnostic tool consists of a dipole magnet for momentum-based particle separation and a large-area pixelated semiconductor detector (RadEye [180]) for high-resolution particle detection and energy measurement. The WASP system enables spatially-resolved spectral analysis of the accelerated ion beams, providing crucial data on energy distribution, beam divergence, and particle flux. A detailed discussion of the WASP system and its capabilities will be presented in Section 4.2.4.

The experimental setup incorporates a comprehensive suite of laser diagnostics to monitor and characterize both the incident laser parameters and the laser-plasma interaction dynamics. The 'incoming light' diagnostic system can be used to monitor the incident laser pulse energy, focal spot quality, and spectral characteristics. An application of this diagnostic is the continuous monitoring of laser focus drift [181]. A 'backscatter' diagnostic system is implemented to analyze light recollimated from the laser-plasma interaction region. These measurements offer valuable insights into the laser-plasma coupling efficiency and the underlying physical processes occurring during the interaction.

All components are integrated into two control systems at CALA: Zentrale Steuerung (ZS) and Tango [182]. Zentrale Steuerung, which translates to "Central Control," serves as the overarching control system for laser and acceleration operations. It comprises a programmable logic controller interfaced with an extensive network of sensors embedded throughout the building and experimental infrastructure. These sensors monitor critical parameters such as the status of radiation safety doors and other safety devices, target positions, and the operational state of the laser system. By overseeing all subsystems, ZS ensures that defined operating conditions are maintained, thereby enhancing both safety and experimental reproducibility.

Complementing ZS, Tango Controls has been adopted as the primary server infrastructure for supervisory control and data acquisition in recent years [183]. As an open-source software framework, Tango offers significant flexibility in implementation and customization. It provides an abstraction layer for communication protocols, enabling seamless integration across diverse operating systems (Windows, Unix, MacOS) and supporting device implementation through multiple programming languages (e.g., Python, Java, MATLAB, C++). This versatility allows for the incorporation of a wide array of instruments into the control system. At CALA, the Python implementation of Tango, known as PyTango, is predominantly utilized. This choice leverages Python's ease of use and extensive scientific computing libraries, facilitating rapid development and integration of

custom control and analysis routines.

4.2.2 Vacuum microscope

For high-power laser experiments, precise measurement and control of the laser focus is crucial. To measure the attenuated focus in situ, a vacuum-compatible microscope was developed and implemented in the experimental setup, which was described in previous works [184,185]. This setup is compact and less sensitive to alignment compared to other methods like relay imaging of the focal plane outside the vacuum chamber.

The microscope is mounted on a motorized stage, allowing it to be positioned at the TCC or moved away to make room for other equipment like PMQ when needed. It uses a Mitutoyo APO NIR 10x objective with a 20 mm working distance to collect light from the focal plane. Beam splitters then direct this light to different diagnostic tools.

One path leads to a high-magnification (high-mag) camera, which uses a 20 cm focal length tube lens to achieve 10x magnification. This camera defines the plane where the laser focus meets the target. Each pixel on this camera represents 0.53 µm in real space. A second, low-magnification (low-mag) camera provides a wider view, which is useful for the initial alignment of the beam optics.

To protect the cameras and prevent signal saturation, a multi-stage attenuation system is employed. First, an attenuator before the pulse compressor lowers the laser energy by about eight orders of magnitude. Then, filters in the microscope further reduce the energy by another six orders of magnitude. To capture the full intensity range of the focal spot, a series of images is recorded using varying levels of attenuation. These images are then computationally combined to generate a High-Dynamic-Range (HDR) representation. For comparison, a Low-Dynamic-Range (LDR) image is also captured using strong attenuation to ensure minimal pixel saturation. According to [68], this HDR technique can extend the effective dynamic range by up to two orders of magnitude.

Figure 4.5 presents a comparison between the LDR and HDR representations of the laser focus fluence distribution. Both images have been centered and standardized to 120×120 pixels, with the focal point at the image center. The LDR image (Fig. 4.5a) shows a focal spot confined to the central region with a well-defined FWHM of 5.7 µm. In contrast, the HDR image (Fig. 4.5b) reveals a broader distribution of laser light, capturing low-intensity features not visible in the LDR image. Notably, the peak intensity estimated from the HDR image is 1.7 times lower than the intensity estimated from the LDR image, consistent with previous findings [68].

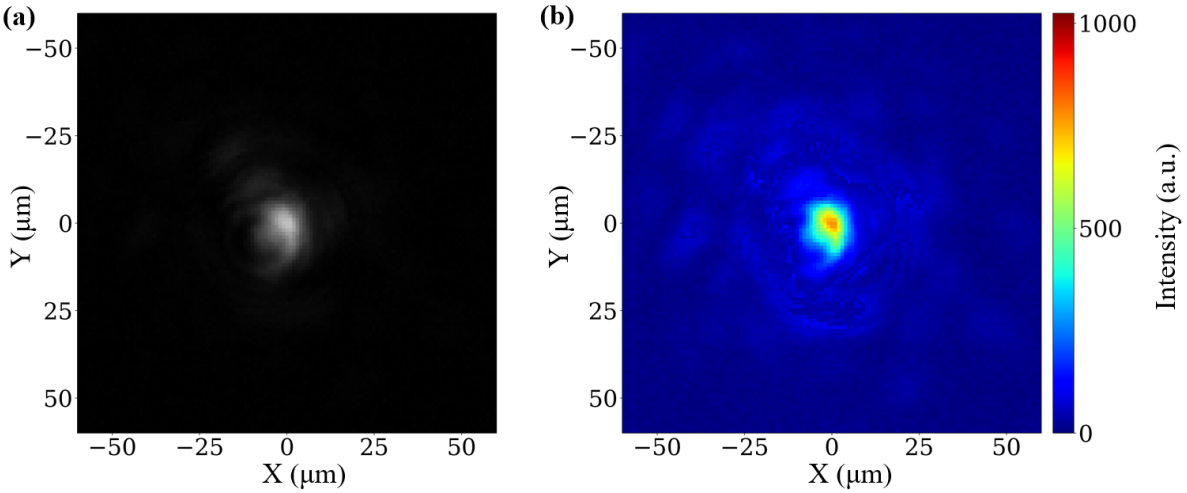

Figure 4.5: Comparison of LDR and HDR focal spot measurements for the ATLAS-3000 laser in the LION chamber. (a) LDR image showing a focal spot with 5.4 µm FWHM. (b) HDR image for accurate peak intensity calculation. Laser parameters: 8.4 J on target, 27 fs pulse duration. Calculated peak intensities: 3.2×10^{20} W/cm^2 ($a_0 \approx 10$) for LDR and 1.9×10^{20} W/cm^2 ($a_0 \approx 8$) for HDR, demonstrating the importance of HDR imaging for precise intensity characterization.

An additional optical path within the microscope system incorporates a wavefront sensor and a near-field camera, enabling precise reconstruction of the wavefront. This information is utilized in a closed-loop feedback system to control a deformable mirror (DM) located in LBD system. This adaptive optics configuration, as described by [186], allows for optimization of the focal spot quality by compensating for optical aberrations in the beam path.

The microscope design also includes auxiliary functionalities facilitated by an additional beam splitter. These include LED illumination for bright-field imaging of targets and the option to connect a fiber-coupled spectrometer for spectral analysis. Besides imaging the focus, an adopted white-light sensor is added to this microscope to measure the target thickness in situ prior to each experimental run.

4.2.3 Cameras

For detailed characterization of the laser-plasma interaction, from initial alignment through to the final stages of particle acceleration, the LION chamber incorporates a comprehensive array of cameras, strategically positioned to capture various aspects of the laser-target interaction and subsequent particle acceleration processes. Figure 4.6

illustrates the layout of these imaging systems within the chamber. Six primary cameras (C1-C6) serve distinct functions in monitoring and diagnostics. Due to the strong EMP generation from laser-plasma interaction, all the cameras have been set up in an EMP-safe housing.

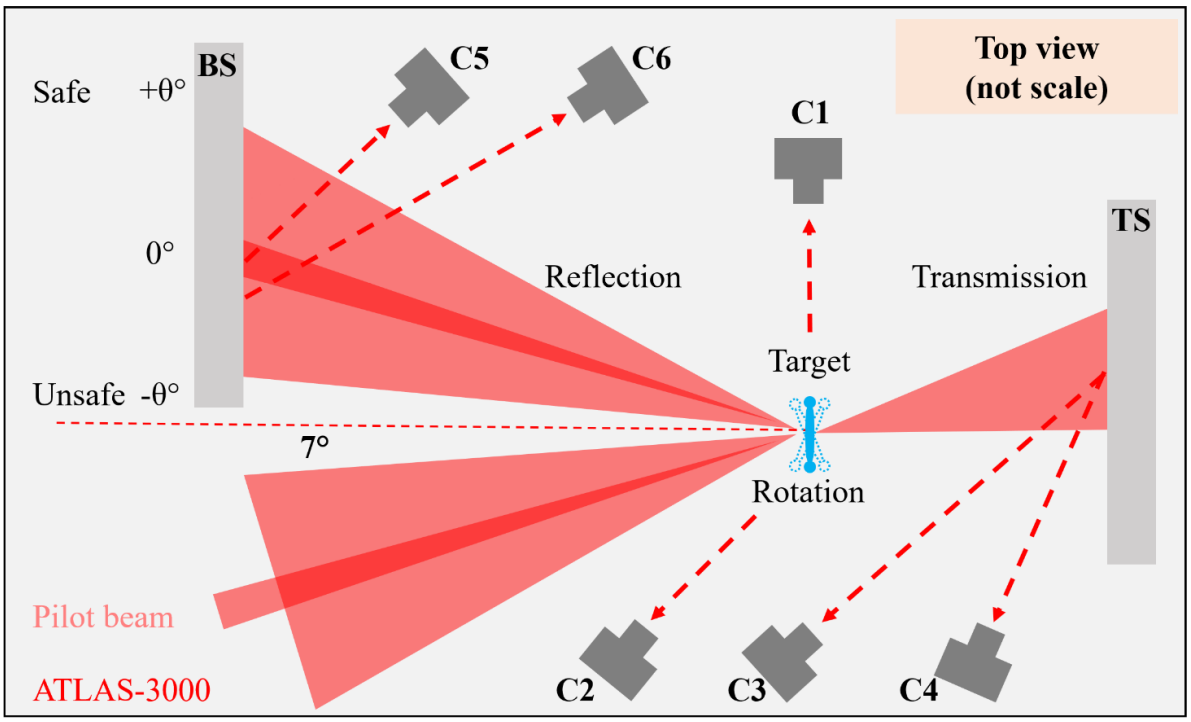

Figure 4.6: Cameras inside LION chamber. Cameras C1 and C2 monitor target alignment with the center of the catcher. Cameras C3 and C4 capture the transmission light with different neutral density (ND) filter settings. Cameras C5 and C6 record the reflection light of ATLAS-3000 and Pilot beam. BS and TS stand for back-reflection screen and transmission screen.

Cameras C1 and C2 are employed for shadowgraphy imaging of the water-leaf target and catcher assembly. These cameras are illuminated by a CW laser operating at a wavelength of 650 nm. To ensure optimal imaging and reduce interference from other light sources (particularly the ATLAS-3000 laser with its 800 nm central wavelength), the cameras are equipped with two FBH650-10 bandpass filters from Thorlabs [187]. These filters have a narrow 10 nm FWHM passband centered at 650 nm, effectively blocking scattered light from the main laser pulse while transmitting the 650 nm illumination light. This configuration allows for continuous monitoring of the target, even during high-power laser shots. Typical shutter times are a few hundred milliseconds (ms), so diagnostics during the shot are not resolved.

Figure 4.7 presents exemplary shadowgraphy images of the water-leaf target captured by cameras C1 and C2. These images provide a crossed view of the target and catcher, offering a three-dimensional perspective of the experimental setup. This visual information is essential for the accurate alignment of the water-leaf target relative to the catcher's center. Such alignment is crucial to ensure proper water drainage from the chamber, preventing target freezing and ensuring optimal experimental conditions.

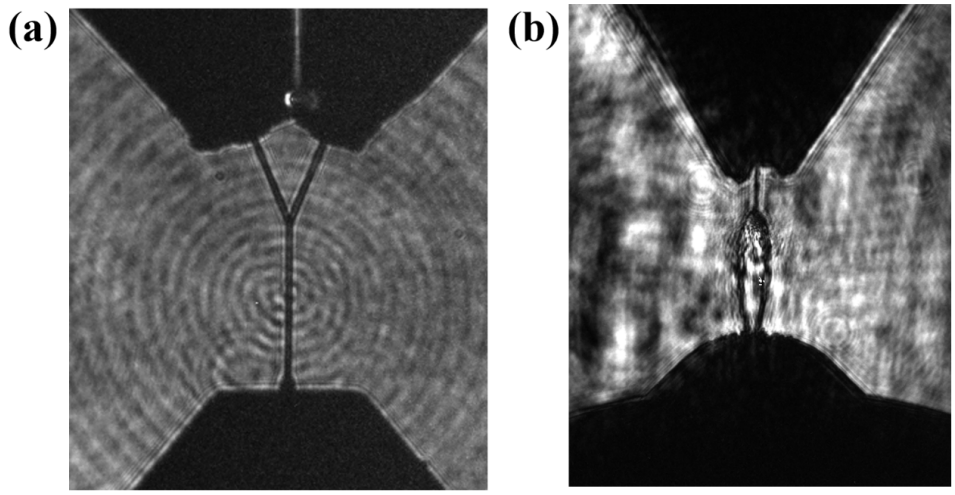

Figure 4.7: Shadowgraphy images of the water-leaf target. (a) View from camera C1, providing a side perspective of the target. (b) Complementary view from camera C2, offering a crossed perspective.

Cameras C3 and C4 are configured to capture transmitted light from the laser-target interaction, each equipped with a specific combination of filters to accommodate a wide range of light intensities. Camera C3, designated for recording transmitted light during laser shots with the target in place, utilizes a lower Neutral Density (ND) filter setup consisting of FELH0700, FBH800-10, NE20A-B, and NE05A-B. This configuration allows C3 to capture higher-intensity transmitted light during actual laser-target interactions with 10 J laser energy on target. In contrast, Camera C4, serving as a reference for calibration by recording empty shots without a target, employs a higher ND filter combination of FELH0700, FBH800-10, NE10A-B, and NE40A-B. Both cameras share identical bandpass filters (FELH0700 and FBH800-10) to eliminate the potential contribution of high harmonic generation during laser-target interactions.

Cameras C5 and C6 are tasked with recording the reflected light from both the high-power ATLAS-3000 laser and the lower-intensity CW Pilot beam. The Pilot beam, following the same optical path as the ATLAS-3000, serves as a constant reference for alignment and target positioning. This setup allows for monitoring the target rotation.

The cameras capture single pictures with a shutter time of hundreds of ms. Currently, images from Camera C5 are used to manually adjust the nozzle position via linear stages, compensating for any detected target rotation and ensuring a consistent laser-target interaction geometry throughout the experiment. Plans are underway to upgrade this process with a self-alignment system.

Furthermore, the combined images from C6 (reflection) and C3 and C4 (transmission) provide a comprehensive picture of the laser-target interaction. Analyzing both reflected and transmitted light can enable the estimate of the energy coupling between the laser and the target, which is relevant for assessing the overall ion acceleration performance.

4.2.4 Wide angle spectrometer

The WASP is the primary diagnostic tool for ion bunch characterization in this study. This apparatus allows for simultaneous and automated online detection of both the energy spectra and angular distribution of laser-accelerated ions. Figure 4.8 presents a schematic overview of the WASP setup. It consists of two main components: a dipole magnet and a RadEye detector [180]. A critical element of the design is a slit positioned in front of the dipole magnet rather than a pinhole. This slit, measuring 200 µm in width and 5 cm in length, samples the proton bunches within an acceptance angle of ±1.5 degrees. This slit width is crucial for adjusting signal of the RadEye detector, and it defines the ion energy resolution. The dipole magnet deflects the proton downward, with the degree of deflection inversely proportional to the proton velocity. Consequently, lower energy protons experience greater deflection and hit the RadEye detector at lower regions.

The RadEye detector consists of four Complementary Metal-Oxide-Semiconductor (CMOS) elements, each referred to as a RadEye1 element, collectively providing a detection area of 10 cm × 5cm with a resolution of 1024 × 2048 pixels. Optimized for visible light detection, each RadEye1 element features a 2 µm active silicon layer supported by a ceramic substrate. Additionally, a 2 µm SiO_2 passivation layer is applied on top of the active silicon layer for protection. The detector's response to ion signals, represented by the pixel value (pv), exhibits a linear relationship with the energy loss (ΔE) of ions within the 2 µm silicon active layer, expressed as [188]:

$$pv = (1.09 \pm 0.12)\Delta E\,[keV]\,. \tag{4.1}$$

It is important to note that the detector can hence detect single protons, responds linearly with the number of particles, and exhibits no significant cross-talk between pixels.

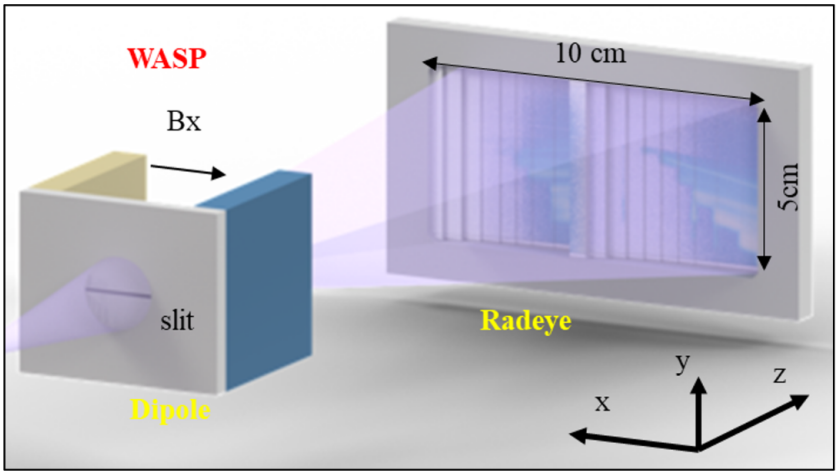

Figure 4.8: Schematic of the wide-angle spectrometer.

The detector's signal is processed by a dedicated Remote RadEye camera system with an Ethernet interface (Teledyne Rad-icon Imaging Corp.), supporting parallel readout of up to four sensors. The pixel values are read out in Analog-to-Digital Units (ADU) with a 12-bit dynamic range (0-4095 ADU) and stored as 14-bit digital images. After readout, the sensor signal is erased for reuse. However, radiation damage can affect how well the sensor works over time, depending on particle flux and dose. For instance, after irradiation with a 20 MeV proton beam at a fluence of 6×10^{10} protons/cm^2, the sensor's dynamic range decreases to approximately 50% of its initial value, while maintaining a linear response to proton fluence [188]. In summary, the RadEye detector is characterized by high sensitivity (capable of detecting single ions), a high dynamic range (up to 400 protons per pixel at 20 MeV), and high spatial resolution ($\sim$50 µm), making it an excellent choice as an online detector for laser-driven ion acceleration experiments.

The large irradiated surface of the detector serves a dual purpose in ion beam characterization: providing a comprehensive view of the ion bunch angular distribution and enabling in-situ calibration of the magnetic deflection. This calibration is crucial due to the inhomogeneous magnetic field resulting from the wide gap of the magnet, which must be accounted for in particle trajectory calculations. To facilitate this calibration, referred to as "Pablone", is positioned in front of the detector. The mask consists of 19 vertical aluminum strips covering the entire active area of the detector, with thicknesses varying along the horizontal axis. The thickness decreases progressively from 5043 µm to 112 µm across the first eight strips, increases to 8104 µm at the ninth strip, and then

decreases to 112 µm for the remaining ten strips.

These strips, with their varying thicknesses, correspond to proton penetration depths ranging from 0.1 mm to 8.1 mm, with associated Proton Penetration Energy (PPE) spanning 3.7 MeV to 42.6 MeV. A schematic representation of the mask is provided in Fig. 4.9, while Table 4.1 offers a detailed overview of the strip positions, aluminum thicknesses, and corresponding proton and O^{8+} Oxygen Penetration Energy (OPE). This mask design enables energy-resolved measurements of the incident ion beam, allowing for precise calibration of the magnetic deflection and accurate reconstruction of the ion energy spectra.

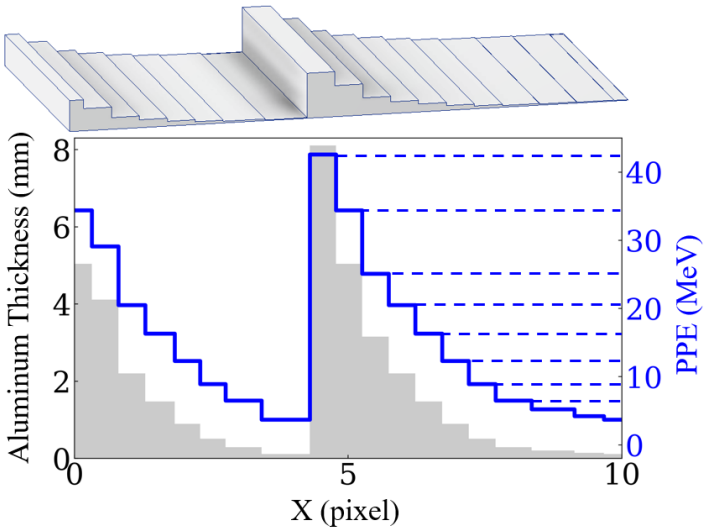

Figure 4.9: Schematic of the aluminum phantom with varying strip thickness from 0.1 mm to 8.1 mm and corresponding PPE from 3.7 MeV to 42.6 MeV.

In the context of ion bunch analysis using the 'Pablone' mask and magnetic deflection, it is important to consider the potential interference from different ion species. While the mask helps filter ions, it does not completely block signals from oxygen ions, particularly for the thinnest strip (0.1 mm thickness). This strip corresponds to a penetration energy of 7.6 MeV/u for O^{8+} ions, as calculated using SRIM. However, the effect of the magnetic field on particle deflection, which is inversely proportional to the Larmor radius ($y_d \propto Bq/mv$), results in distinct vertical positions on the detector for oxygen ions and protons [179]. For protons, the deflection range on the detector spans from 1.5 cm (30 MeV) to 4.31 cm (3.7 MeV) from top to bottom, with higher-energy protons experiencing smaller deflection. In contrast, the maximum deflection for oxygen ions occurs at the highest charge state (O^{8+}) and the lowest energy (7.6 MeV/u). Based on the experimental setup and calculations, the maximum deflection for oxygen ions (O^{8+})

is 1.5 cm. Therefore, there is no contribution from oxygen ions in the proton energy range up to 30 MeV.

xCenter (pixels)	**Thickness (µm)**	**PPE (MeV)**	**OPE (MeV/u)**
33	5043	34.4	70.9
115	4112	29.1	63.3
215	2202	20.5	44.6
320	1472	16.3	35.5
423	892	12.3	26.8
518	512	8.9	19.4
633	292	6.5	13.9
790	112	3.7	7.6
929	8104	42.6	92.7
1027	5043	34.4	70.9
1126	3153	25.1	54.5
1225	2202	20.5	44.6
1325	1472	16.3	35.5
1425	892	12.3	26.8
1525	512	8.9	19.4
1643	292	6.5	13.9
1790	202	5.2	11.1
1925	142	4.2	8.9
2014	112	3.7	7.6

Table 4.1: List of detector aluminum phantom stripes, their positions, their thicknesses, and corresponding proton penetration energy.

Figure 4.10 presents an example sensor image from the RadEye detector, revealing a broad spatial distribution with distinct steps. Those steps correspond to points where ions possess sufficient velocity (or kinetic energy) to penetrate the respective aluminum thicknesses of the Pablone mask. The resulting image exhibits a characteristic staircase structure, reflecting the modulation of the broad proton energy spectrum by the Pablone. By correlating the magnetic deflection $y(E_{kin}, B)$ with the known energy values $E_{kin}(x)$ listed in Table 4.1, a set of points (x, y) in the detector plane coordinates can be established, each associated with discrete proton kinetic energies E_{kin}. These points, represented by red dots in Fig. 4.10, serve as calibration points for the magnetic field.

The magnetic field can be approximated by the following equation [189]:

$$B_x(x) = a(x-d)^4 + b(x-d)^2 + c. \tag{4.2}$$

Here, the x-direction is aligned with the entrance slit. The effective parameters a, b, c,

and d are obtained by fitting this function to the calibration points in Fig. 4.10. Although the magnetic field is inhomogeneous along the propagation direction z, this has minimal impact on the analysis due to the small actual displacement within the magnet. The result of such a fit is overlaid to the sensor image in Fig. 4.10. The solid orange curves of constant proton energy quite accurately follow the red dots and closely resemble the steps in the spatial distribution. This outcome of the Pablone mask eliminates the need for direct magnetic field measurement, which is typically complex and labor-intensive.

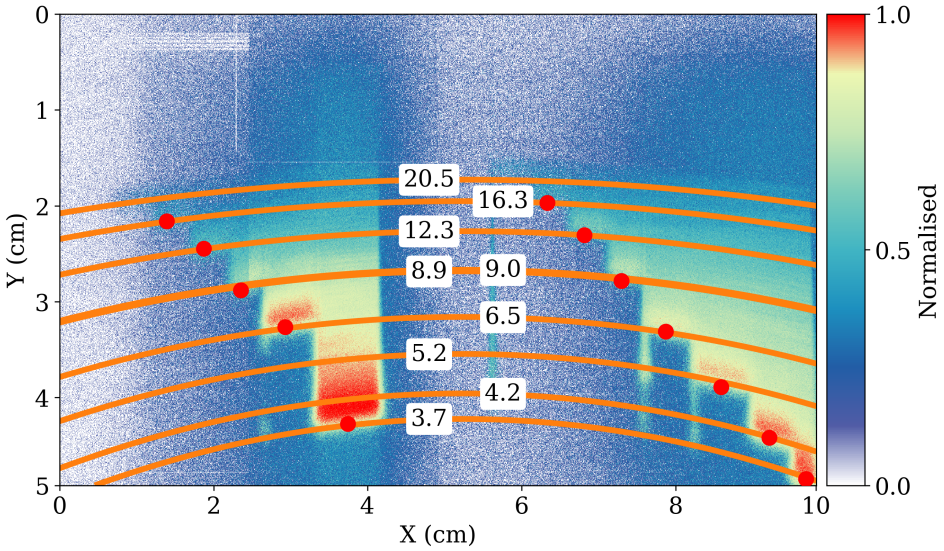

Figure 4.10: Example sensor image. In the horizontal direction, the angular distribution is sampled. The Lorentz force deflects positively charged particles downwards. The red dots indicate the (x, y) position of the support points used for this fit. The orange curves represent the calculated dispersion based on the best fit of the magnetic field distribution model with 4 effective parameters (see text). The values indicate the iso-energy of protons.

Each sensor pixel can now be associated with kinetic energy and angle, creating an energy-angle mesh [190]. The detector is then subdivided into multiple monoenergetic regions, termed macro areas, by assuming that the point source projects the slit aperture onto the detector plane. With a source-to-sensor distance of 1.63 m and the 200 µm slit aperture positioned at 83 cm downstream of the source, the height of the slit projection is 393 µm in the y-dimension. Given the RadEye pixel pitch of 48 µm, 9 pixels were selected for a macro area on the detector along the y-dimension, corresponding to a vertical angular range of 0.27 mrad. For the evaluation, only ±30 pixels around the center pixel of the slab of the aluminum phantom in the horizontal x-direction were utilized. Each macro area therefore covers a solid angle $\Delta\Omega \approx 0.48$ µsr. Using the

magnet dispersion relation, the center kinetic energy E_{kin} in MeV and the kinetic energy width ΔE_{kin} in MeV for each macro-region can be calculated. The spectrum, $N(E_{kin})$ in protons/MeV/msr, can then be determined by combining this information with Eq. 4.1:

$$N(E_{kin}) = \frac{pv}{(1.09 \pm 0.12)\Delta_p \Delta E_{kin} \Delta\Omega} \tag{4.3}$$

where Δ_p is the most probable energy loss in MeV, given by [191]:

$$\Delta_p = \xi \left[ln\frac{2m_e c^2 \beta^2 \gamma^2}{I} + ln\frac{\xi}{I} + 0.200 - \beta^2 - \delta(\beta\gamma) \right] \tag{4.4}$$

Figure 4.11(a) displays a typical recorded image with post-processing for 8.4 J laser energy, where the magnetic field causes protons to deflect downwards. The orange vertical lines mark the positions of the aluminum stripes. An uplifted signal onset indicates thicker aluminum, implying higher penetration energy. The incorporation of the aluminum stripes provides immediate insights into ion performance, particularly concerning the maximum proton energy. For example, in Fig. 4.11(a), it is evident that the maximum proton energy exceeds 20.5 MeV but remains below 25.1 MeV. However, the mask restricts full angular resolution as a trade-off.

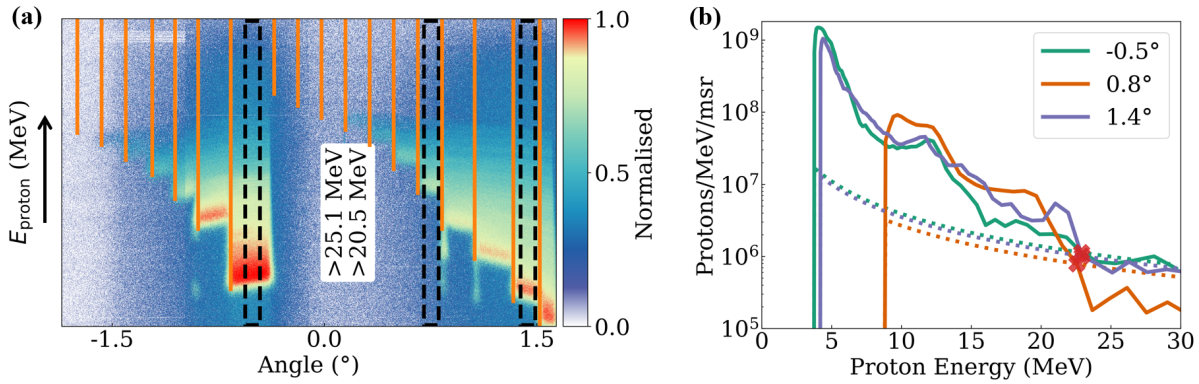

Figure 4.11: (a) Typical stair-like proton spectra obtained from the RadEye detector for 8.4 J laser energy. The columns between orange lines represent the position of an aluminum phantom with varying thicknesses, where uplifted signal onset indicates thicker aluminum, correlating with higher penetrating energy. Three black dashed rectangles correspond to different angular positions, specifically -0.5°, 0.8°, and 1.4°, with the target's normal direction at 0°. (b) Reconstructed spectra for different angular positions (see the figure legend); solid and dotted lines represent spectra and noise levels, respectively.

For spectrum reconstruction, three different angular positions at -0.5°, 0.8°, and 1.4°

are considered, with the target's normal direction at 0°. These positions are represented by the three black dashed rectangles in Fig. 4.11(a). The positions at -0.5° and 1.4° feature the thinnest strips, offering detectable proton energies as low as 3.7 MeV and 4.2 MeV, respectively. The thicker strip positioned in front of the detector at 0.8° significantly reduces background noise, which aids in identifying the maximum proton energy. The calculated spectrum is displayed in Fig. 4.11(b), where solid lines represent the particle flux, reaching up to 1.0×10^9 protons/MeV/msr. The intersection of the spectrum with the noise level (dotted lines) indicates a maximum proton energy of about 23 MeV, in good agreement with the initial estimation based on the mask.

It is important to note that when the ion flux is low enough to ensure sparse irradiation of the pixels, i.e., not exceeding the average fluence of one particle per pixel, individual ions can still be accurately counted. For higher flux levels, where multiple ions hit one pixel, an average energy loss per particle may be assumed, as long as the detector does not reach saturation. This approach, while commonly used, requires careful validation in situations where a few ions hit one pixel, which lies between single-particle and high-flux cases. Further investigation is necessary to determine the validity of this method under such intermediate conditions.

A novel approach, Quantitative Ion Spectrometry (QIS) [179], has recently been introduced to address these calibration challenges, particularly the issues of the dispersion relation and the detector response. This method is based on the energy loss distributions of charged particles traversing thin layers, which serve as the foundation for the Signal Distribution Function (SDF). The SDF is further convolved with a binomial distribution to account for multiple particle hits per pixel, a common occurrence in high-flux experiments. While the method necessitates careful identification and treatment of distinct background sources, it has been demonstrated to perform optimally when the number of particles ranges between one-tenth and ten times the number of pixels in the evaluated macro-pixel region.

QIS enables precise determination of the absolute differential spectrum without requiring prior measurement or simulation of the magnetic field distribution or any prior information about detector response. Figure 4.12 compares proton spectra reconstructed using QIS with those obtained by the original method. Both approaches produce similar spectra, but QIS more clearly identifies a maximum proton energy of 29 MeV.

Since QIS is still in development and undergoing further refinement, the results presented in this thesis are analyzed using the original method, in which spectra are reconstructed based on Eq. 4.1 unless stated otherwise.

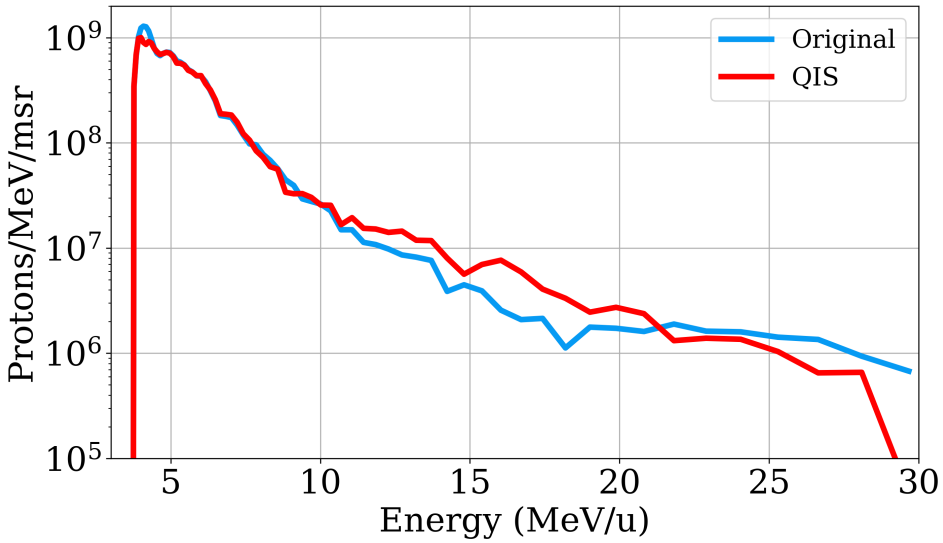

Figure 4.12: Proton spectra reconstruction from different methods.

Chapter 5

Experiments

The experiments were conducted at the CALA in Garching, Germany, using the ATLAS-3000 laser system. All campaigns focused on ultra-intense laser irradiation of water-leaf targets for proton acceleration studies. The first campaign investigated experimental parameter variation, particularly the scaling of maximum proton energy with laser pulse energy. The second campaign focused on shot-to-shot variations of the proton bunch parameters, specifically the maximum energy and particle flux. In the third campaign, the effect of the polarization of the laser pulse on proton acceleration was explored. The results have been submitted for publication [192].

5.1 Variation of experimental parameters

5.1.1 Laser energy scan

The maximum proton energy ($E_{\max}$) was measured as a function of laser energy (E_L), ranging from 1.1 J to 8.4 J on target, achieved by sequentially turning on amplifiers. This corresponded to a peak intensity (I_0) ranging from 1.2×10^{20} W/cm^2 to 9.2×10^{20} W/cm^2, while maintaining the same nominal laser-target interaction position and laser pulse duration. The experiment comprised 65 shots executed in shot-on-demand mode, systematically organized into 6 groups according to the laser energy, as depicted in Table 5.1. The resulting average maximum proton energies (mean) at -0.5°, 0.8°, and 1.4° with standard deviation (std) are also presented in Table. 5.1. The measured average maximum proton energies ranged from 5 MeV to 20 MeV. This dataset served as the basis for power-law fits to establish the relationship between E_{max} and E_L.

	E_L (J)	N_{shot}	E_{max} [$mean \pm std$] (MeV)		
			-0.5°	0.8°	1.4°
Group 1	1.1	6	4.6 ± 0.5	Nan	5.0 ± 0.5
Group 2	1.9	9	8.5 ± 0.9	9.9 ± 0.5	8.4 ± 0.6
Group 3	3.0	20	11.7 ± 1.1	12.8 ± 0.7	11.7 ± 0.8
Group 4	4.9	12	12.4 ± 3.1	14.5 ± 1.9	13.0 ± 1.3
Group 5	6.2	11	13.3 ± 2.6	16.8 ± 0.8	15.4 ± 0.8
Group 6	8.4	7	19.8 ± 3.0	18.8 ± 1.5	19.1 ± 2.4

Table 5.1: Laser energies (E_L) employed during the beamtime on 20230808, along with the corresponding number of shots. The maximum proton energies (E_{max}) are presented as means with standard deviations for -0.5°, 0.8°, and 1.4°.

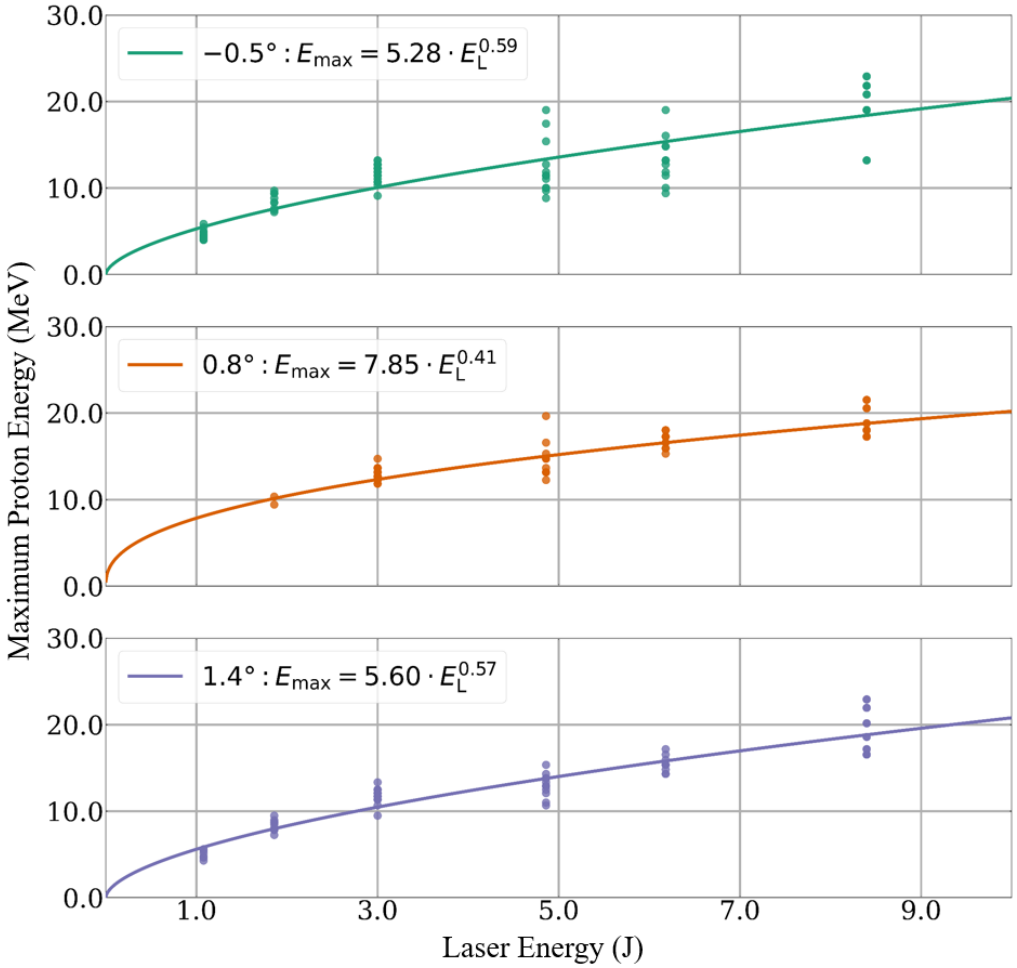

Figure 5.1: Maximum proton energy as a function of the laser energy. The average data points with standard deviation are displayed in blue, green, and purple for -0.5°, 0.8°, and 1.4°, accompanied by power-law fits at each laser energy.

Figure 5.1 displays the average maximum proton energies as a function of laser energy, with power-law fits described by the equation $E_{\max} = a \cdot E_L^b$. The fitting was performed using the "scipy.optimize.curve_fit" function in Python, which also provided the uncertainties of the fitted parameters a and b. The standard deviations or errors of these parameters are calculated as the square roots of the diagonal elements of the covariance matrix. This leads to the scaling relations obtained for angles of -0.5°, 0.8°, and 1.4° are $E_{\max,\ -0.5^\circ} = (5.28 \pm 0.98) \cdot E_L^{0.59\pm0.11}$, $E_{\max,\ 0.8^\circ} = (7.85 \pm 0.39) \cdot E_L^{0.41\pm0.03}$, and $E_{\max,\ 1.4^\circ} = (5.60 \pm 0.54) \cdot E_L^{0.57\pm0.06}$, respectively. For the sake of clarity and to focus on the trend of the scaling, only the scaling relations without errors are displayed in Fig. 5.1: $E_{\max,\ -0.5^\circ} = 5.28 \cdot E_L^{0.59}$, $E_{\max,\ 0.8^\circ} = 7.85 \cdot E_L^{0.41}$, and $E_{\max,\ 1.4^\circ} = 5.60 \cdot E_L^{0.57}$, respectively.

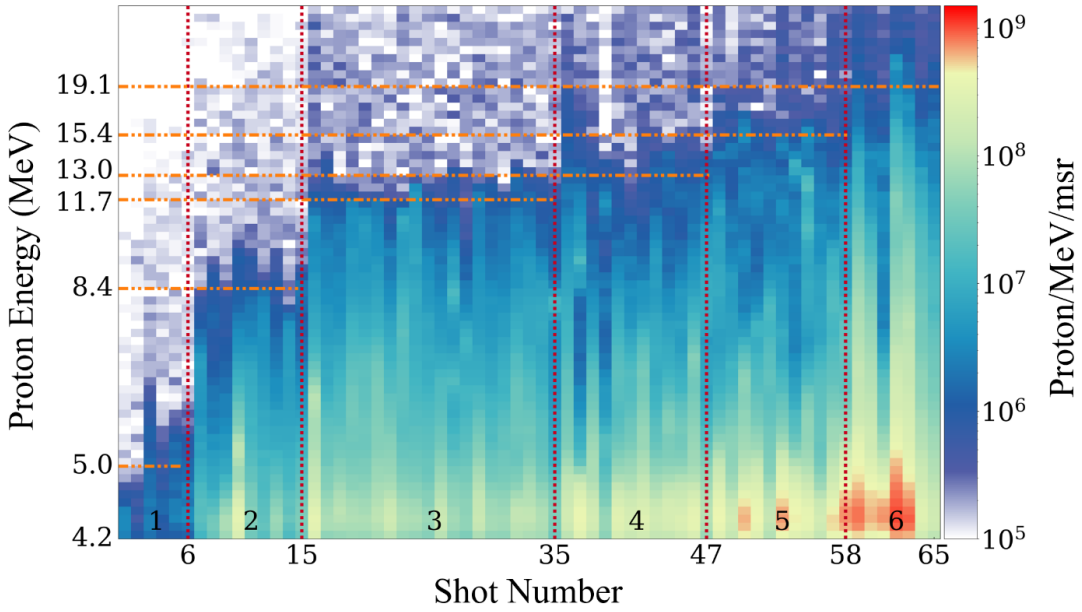

Figure 5.2: Proton spectra of 65 shots at 1.4° with a detectable minimum proton energy of 4.2 MeV. The spectra are sorted into six groups labeled from 1 to 6 (separated by red dotted lines) representing different laser energy settings: 1.1 J, 1.9 J, 3.0 J, 4.9 J, 6.2 J, and 8.4 J, respectively. The orange dash-dotted lines indicate the average maximum proton energy for each laser energy setting with the nonlinear y-axis scale. The color bar represents the differential number of protons in spectra.

In addition to maximum proton energy, it is also interesting to characterize the proton (energy distributions) spectra for all shots corresponding to varying laser energy on target. Figure 5.2 presents example proton spectra at 1.4°. Despite the shot-to-shot variations, the proton spectra exhibit a clear step structure, indicating that both particle flux and

maximum proton energy increase with increasing laser energy. Notably, for group 3 ($E_L = 3.0$ J), the stability of proton bunches seems better than in other groups or at other laser energy.

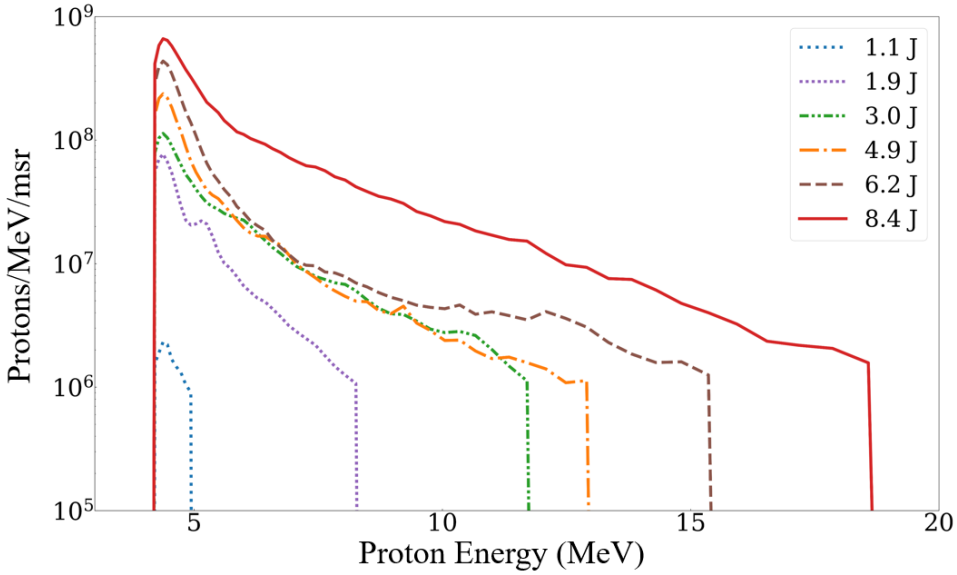

Figure 5.3: Average proton spectra at 1.4° corresponding to different laser energies indicated as color codes and line styles. Each spectrum represents the mean of multiple shots at a specific laser energy.

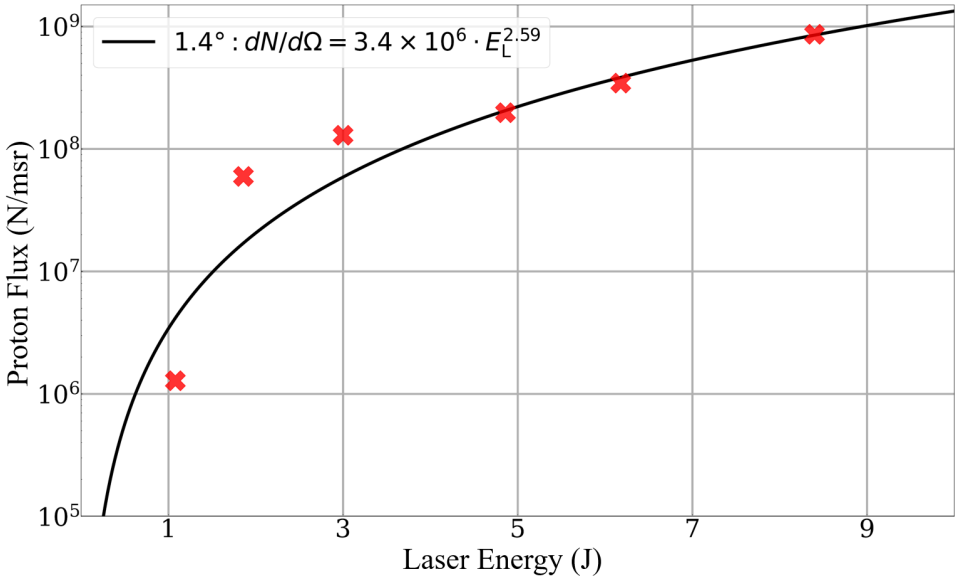

Figure 5.4: Proton flux at 1.4° as a function of the laser energy. The average data points are displayed in red, accompanied by power-law fits at each laser energy.

The average energy spectra shown in Fig. 5.3 highlight the significant rise in particle yield as the laser energy grows, spanning three orders of magnitude—from 10^6 to 10^9 protons/MeV/msr. It is important to point out that the cutoff of the energy spectra is artificial, set in alignment with the average maximum proton energy values from Fig. 5.2 (as indicated by the orange dash-dotted lines). Additionally, a scaling relationship between laser energy and proton flux (integrated across all energies at 1.4°), was identified as $dN/d\Omega = (3.4 \pm 2.03) \times 10^6 \cdot E_L^{2.59\pm0.29}$ and simplified scaling without errors was shown in Fig. 5.4.

5.1.2 Focus and defocus scan

In addition to varying the laser energy, adjusting the target position relative to the focus point also changes the laser intensity on target. The intensity reaches its maximum at the focal point and decreases with increasing distance from the focus. However, accurately identifying the real focal position at full energy presents a significant challenge without an on-shot and full-power diagnostic, as it is typically determined using an attenuated laser beam and is subject to temporal drift. The focus and defocus scan methodology addresses these challenges by systematically varying the target position relative to the nominal focal point. This approach enables the identification of the optimal laser-target interaction position, characterizes the sensitivity of proton acceleration to positional changes, and may reveal unexpected effects related to pre-plasma formation or other intensity-dependent phenomena. By employing this technique, one can optimize experimental parameters and eventually gain added insights into the complex situation in the experiments.

Figure 5.5 presents the schematic of the experimental setup used for the focus and defocus scan. In this configuration, the laser beam position remained fixed while the water-leaf target was moved using a Hexapod, with the 0 position corresponding to the initial measured laser focus position. Upstream positions are defined as negative and downstream positions as positive. The first campaign, conducted during beamtime on 20230915, involved moving the target from 0 to -300 µm (upstream), as this direction yielded better ion performance. For comparison, a second beamtime on 20231115 was conducted with the target position varied within a range of -150 µm (upstream) to 150 µm (downstream). The corresponding results are displayed in Fig. 5.6 and Fig. 5.7.

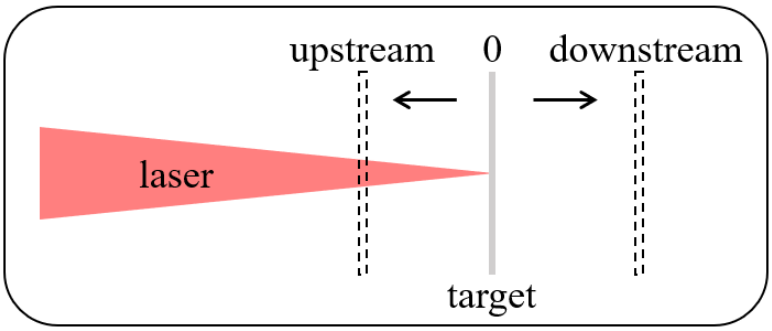

Figure 5.5: Schematic of the experimental setup for the focus and defocus scan.

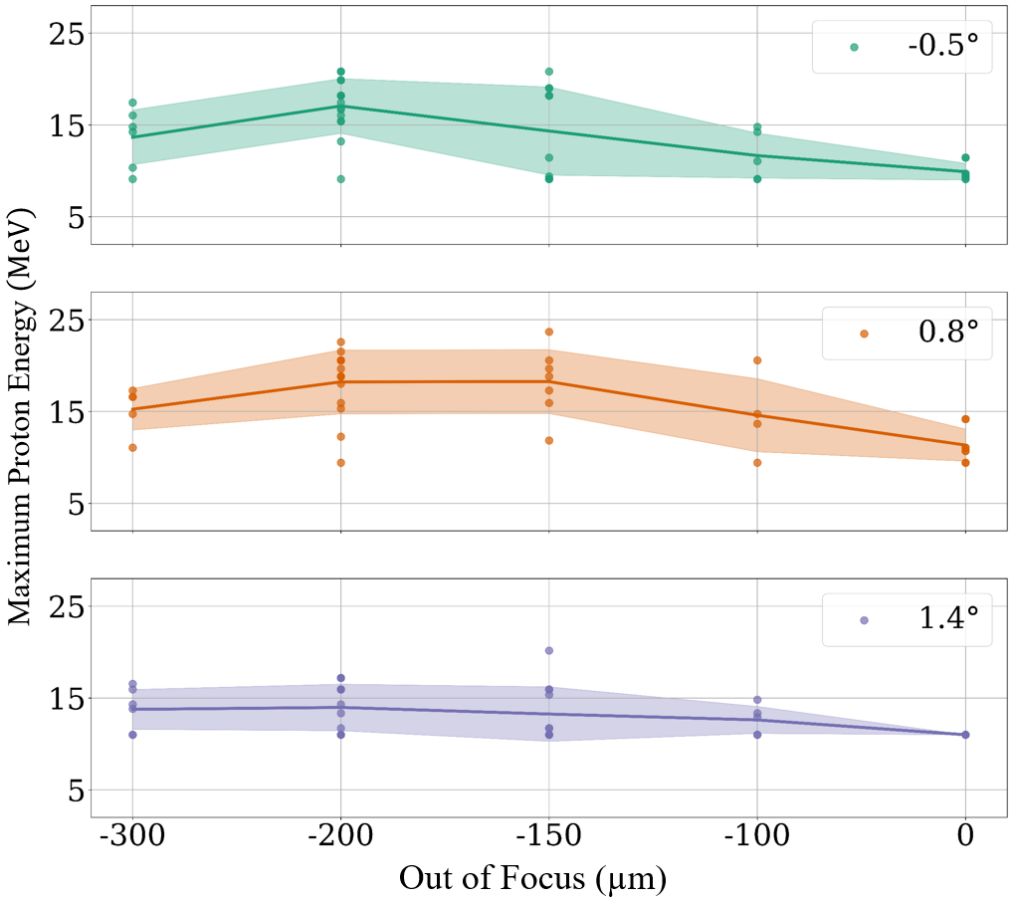

Figure 5.6: Variation of the maximum proton energy as a function of out-of-focus distance for beamtime conducted on 20230915.

Figure 5.6 and Figure 5.7 illustrate the relationship between the maximum proton energy E_{max} and the target's distance from the laser focus (out of focus) for beamtimes on 20230915 and 20231115, respectively. Due to significant shot-to-shot variation, the averaged E_{max} is used for the subsequent analysis. Only shots with E_{max} exceeding the

minimal detectable energy at each angular position are considered, which, along with variations in proton bunch pointing, leads to differing shot counts for angular positions.

Figure 5.6 illustrates that proton acceleration performance is optimized at positions out of focus rather than at the focal plane. For example, the optimal average E_{max} is measured at 17.0 MeV with the target positioned at -200 µm out of focus for $-0.5°$. In contrast, the E_{max} is minimized at the focal plane (0 position), where it reaches only 10.0 MeV. Similar trends are observed across all three angular positions, with the highest E_{max} of 24 MeV recorded at -150 µm out of focus for the angular position of 0.8°. In short, the overall sensitivity of proton acceleration performance to focus position (except for the focal plane) is quite weak, considering that the Rayleigh length is approximately 80 µm and the shot-to-shot variations are large.

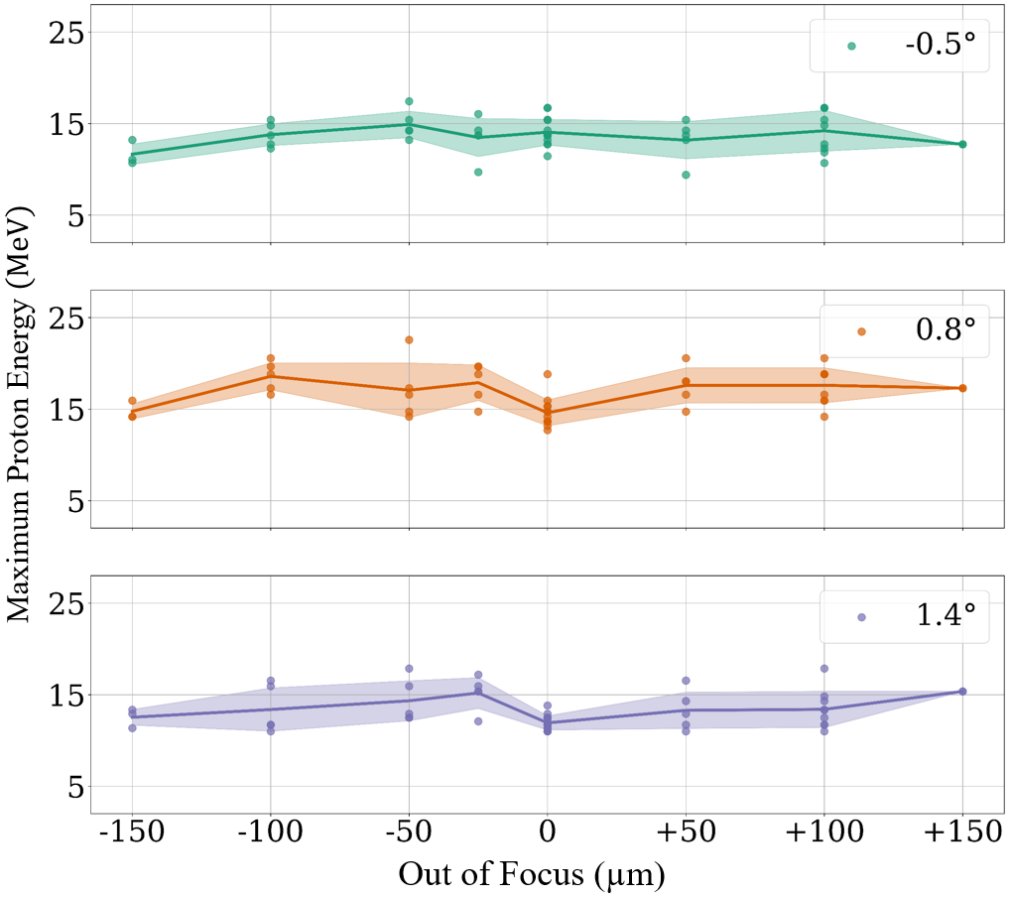

Figure 5.7: Variation of the maximum proton energy as a function of out-of-focus distance for beamtime conducted on 20231115.

The results in Fig. 5.7 underline this observation, as no clear change in proton acceleration performance is noted for target positions between -150 µm and 150 µm,

except for a significant degradation in the proton acceleration performance at the focal plane. All three different angular positions show similar trends. The average E_{max} remains relatively stable across different out-of-focus positions, with an average of 13.0 MeV at $-0.5°$, 17.0 MeV at 0.8°, and 14.0 MeV at 1.4°. The maximum E_{max} reaches 23 MeV at -50 µm out of focus for the angular position of 0.8°.

5.1.3 Thickness scan

Target thickness is a critical parameter in laser-plasma interactions, with an optimal thickness for ion acceleration existing under specific experimental conditions. For this study, the expected optimal thickness is in the sub-micrometer to hundreds of nanometers range. Although the current experiment uses target thicknesses between 2 µm to 20 µm, as shown in Fig. 3.15, investigating the effect of target thickness on proton acceleration remains valuable. Future research should focus on generating thinner targets to match the optimal conditions required by the laser system.

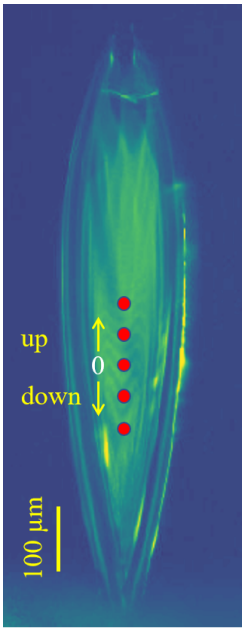

Figure 5.8: Schematic of the target thickness scan setup. The 0 position marks the typical laser-target interaction point, where the target thickness is approximately 5 µm. Red dots indicate possible laser-target interaction positions along the thickness profile. The scale bar represents 100 µm.

The thickness scan can be conveniently performed by vertically adjusting the target position with a hexapod. A schematic of the thickness scan is presented in Fig. 5.8. The

middle segment of the water leaf, with an approximate thickness of 5 µm, was typically selected as the laser-target interaction position.

The first beamtime on 20230918 utilized 10 J of laser energy on target, with the target's relative position adjusted along the vertical axis from -100 µm to +100 µm, spanning thicknesses between 4 µm and 6 µm, as shown in Fig. 3.15. During a subsequent beamtime on 20231115, an 8.2 J laser energy was applied, and the target was scanned in the upward direction over an extended range between 0 and +400 µm, covering thicknesses from 5 µm to 14 µm.

Figure 5.9 and Figure 5.10 illustrate the relationship between maximum proton energy (E_{max}) and the target thickness for beamtimes on 20230918 and 20231115, respectively. For analysis, averaged E_{max} values are used, and only shots with E_{max} above the minimal detectable energy at each angular position are included. This selection, along with variations in proton bunch pointing, results in different shot counts for angular positions.

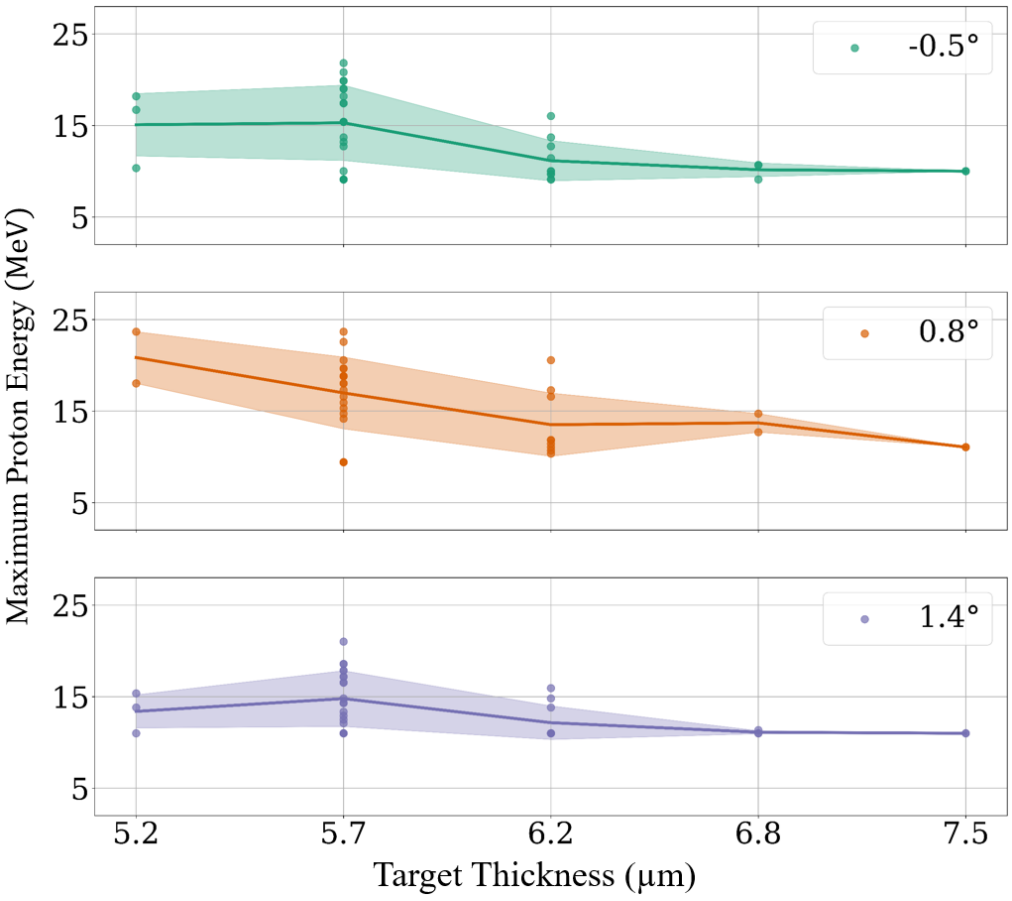

Figure 5.9: Dependence of maximum proton energy (E_{max}) on target thickness for beamtime conducted on 20230918.

Figure 5.9 reveals a clear inverse correlation between E_{max} and increasing target thickness. For instance, at 0.8°, E_{max} declines from 21 MeV to 11 MeV as the target thickness increases from 5.2 µm to 7.5 µm. This decline is more pronounced for target thicknesses below 6.2 µm, whereas for thicknesses greater than 6.2 µm, E_{max} exhibits a relatively stable behavior, fluctuating between 10 MeV and 13 MeV across different angular positions, specifically, 10 ± 0.6 MeV at $-0.5°$, 13 ± 1.5 MeV at 0.8°, and 11 ± 0.1 MeV at 1.4°.

In agreement with the trends observed in Fig. 5.9, further increasing the target thickness from 6.2 µm to 14.3 µm results in minimal changes in E_{max}. As shown in the Fig. 5.10, the average E_{max} remains consistent at 13.7 MeV ± 1.6 MeV for $-0.5°$, 14.9 MeV ± 1.3 MeV for 0.8°, and 12.1 MeV ± 1.1 MeV for 1.4°, respectively.

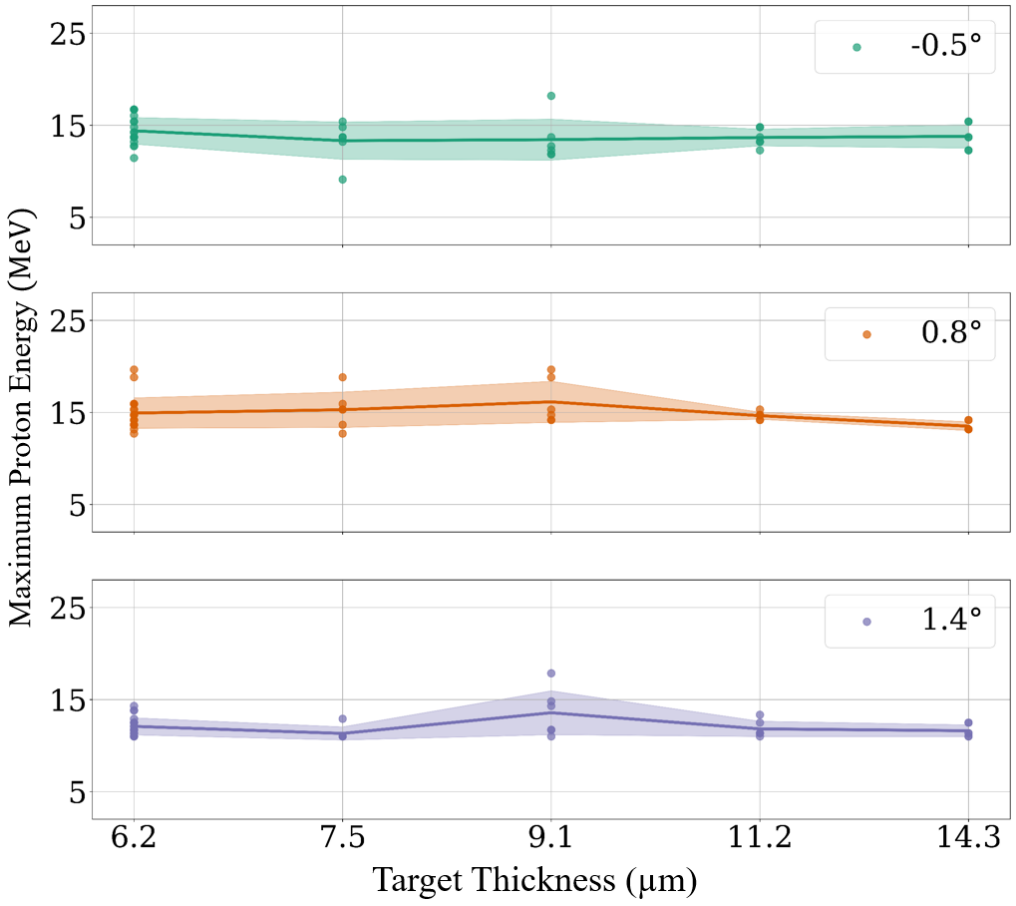

Figure 5.10: Dependence of maximum proton energy (E_{max}) on target thickness for beamtime conducted on 20231115.

5.2 Shot-to-shot variations of the proton bunches

5.2.1 Effect of repetition rate and laser-target interaction position

A beamtime on 20230502 investigated the effects of repetition rate and laser-target interaction position on the stability of ion acceleration. In this campaign, 64 additional shots were recorded at a constant laser energy of 5.1 J, operating in burst mode. The repetition rate was limited to 0.3 Hz due to the readout speed of the RadEye detector. Despite recent updates enabling the RadEye to support over 1 Hz operation, higher repetition rates presented challenges for the data acquisition system. These challenges arose from the large volume of data being saved, including images and laser information, occasionally leading to data loss, particularly for RadEye information.

The shots were categorized by repetition rates as detailed in Table 5.2. Specifically, shots 1 to 9 were conducted at 0.1 Hz, shots 10 to 18 at 0.2 Hz, and shots 19 to 26 at 0.3 Hz. Subsequently, the repetition rate was reduced to 0.2 Hz for shots 27 to 45 and further reduced to 0.1 Hz for shots 46 to 64. For these latter shots, the laser-target interaction point was shifted 150 µm downward to the lower (thinner) segment of the water-leaf target, where the thickness decreased from 5 ± 0.4 µm to 4 ± 0.3 µm.

	Group 1	**Group 2**	**Group 3**	**Group 4**	**Group 5***
Shot Number	1–9	10–18	19–26	27–45	46–64
Repetition Rate (Hz)	0.1	0.2	0.3	0.2	0.1
Thickness (µm)	5	5	5	5	4

Table 5.2: Summary of the repetition rates, shot numbers for each group, and corresponding target thickness in the experiment. *In Group 5, the laser-target interaction position was shifted 150 µm downward to the lower (thinner) segment of the water-leaf target.

Test shots were performed between individual bursts at different repetition rates, as represented by the gaps in Fig. 5.11 but not listed in Table. 5.2. These test shots ensured the proper functioning of hardware components–such as cameras, the RadEye detector, and the target system–and prevented strong back reflections into the laser system. Unfortunately, the campaign was particularly challenging, as the setup was only fully ready at 2:00 am on the second day. The investigation of the impact of repetition rate was not carried out with greater statistical rigor due to the limited time available for the experimental campaign.

Figure 5.11 shows proton spectra extracted at three distinct angular positions (-0.5°,

0.8°, and 1.4°) in a waterfall plot. The data provide an initial indication that the maximum proton energy reaches up to 20 MeV and a peak particle flux at 4 MeV is up to 10^9 protons/MeV/msr at -0.5° position. Notably, the last group (from 57:45 to 60:55) exhibits significant fluctuations. To further evaluate acceleration performance, the analysis concentrated on two critical output parameters: proton energy and flux stability.

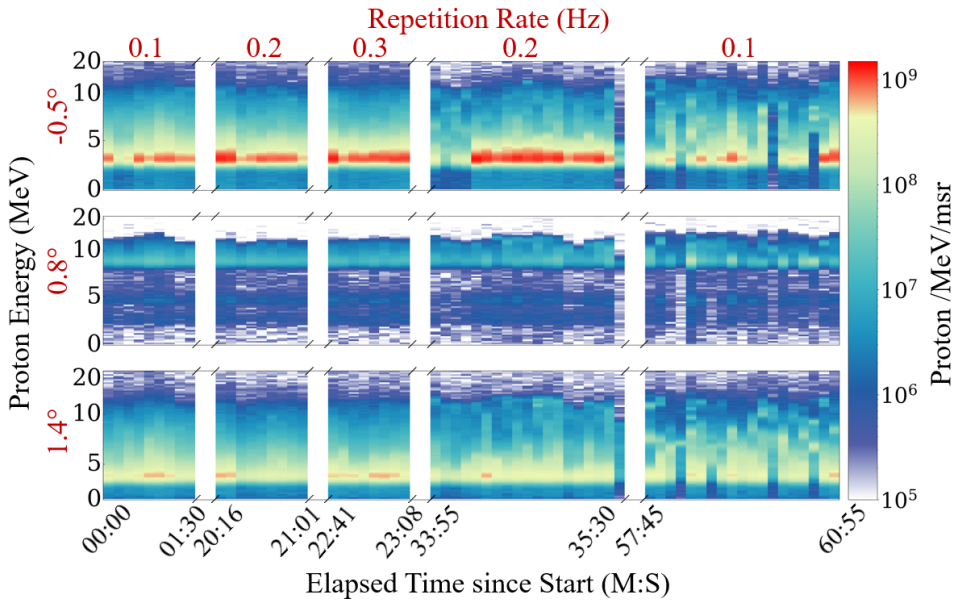

Figure 5.11: Effect of repetition rate and laser-target interaction point on proton stability. Data from 64 shots were collected at a laser energy of 5.1 J. Gaps in the plot represent test shots between bursts.

Data points in Fig. 5.12 represent the maximum proton energy, while those in Fig. 5.13 show the proton flux at 10 MeV for each shot across three angular positions. Shaded areas denote standard deviations ($\pm\sigma$) around the mean (μ), indicated by the dotted line. For the last 19 shots, where proton flux fluctuations exceed two orders of magnitude, the dotted lines represent the median, and the shaded regions reflect the interquartile range (IQR), as shown in Fig. 5.13. The following discussion focuses on averaged values across the three angular positions for simplicity.

For the first 26 shots (Group 1 to Group 3), the average maximum proton energy and standard deviation at three distinct angular positions are as follows: 15.7 MeV ± 1.1 MeV at 0.1 Hz, 14.9 MeV ± 0.6 MeV at 0.2 Hz, and 15.4 MeV ± 0.4 MeV at 0.3 Hz. The following 19 shots (Group 4), operating at 0.2 Hz, exhibit a similar average maximum proton energy of 15.3 MeV but with a larger standard deviation of ± 2.0 MeV. In the final 19 shots (Group 5), although operating at 0.1 Hz, a slight increase in the averaged maximum pro-

ton energy is observed, reaching 16.4 MeV with a similar standard deviation of ±1.4 MeV.

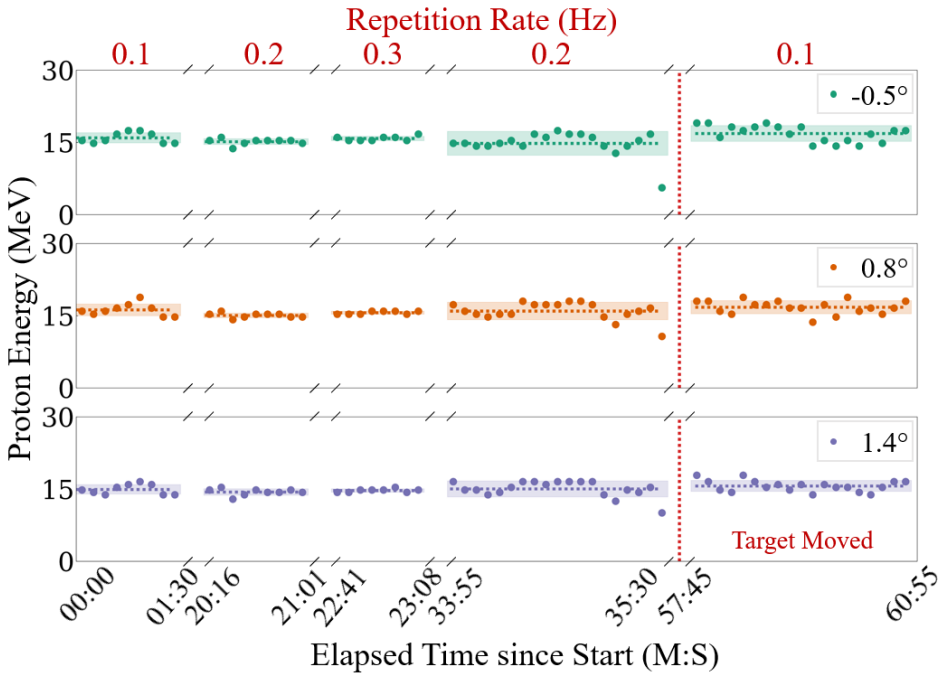

Figure 5.12: Maximum proton energy for all shots, with standard deviations shown as shaded areas around the mean (dotted lines). Red dotted lines indicate shifts of 150 µm downward in the laser-target interaction position, corresponding to a target thickness of 4 ± 0.3 µm.

A similar trend is observed for proton flux at 10 MeV, except for the large fluctuation in the last 19 shots, as shown in Fig. 5.13. For the first 26 shots, the average proton flux at 10 MeV remains stable across repetition rates from 0.1 Hz to 0.3 Hz, with a mean value of approximately $(1.0 \pm 0.2) \times 10^7$ protons/MeV/msr. The following 19 shots, operating at 0.2 Hz, display a similar average proton flux but with an increased standard deviation of $(0.8 \pm 0.4) \times 10^7$ protons/MeV/msr. In the last 19 shots operating at 0.1 Hz, the proton flux varies from 10^6 to 10^8 protons/MeV/msr, with a median of 10^7 protons/MeV/msr and an IQR of 10^7 protons/MeV/msr.

These results depicted in Fig. 5.11, Fig. 5.12, and Fig. 5.13 suggest that the repetition rate is not a limiting factor for stable proton performance. However, targeting the lower (thinner) segment of the water-leaf leads to slightly larger maximum proton energies, in line with the observation during the thickness scan, but also to larger fluctuations of proton yield.

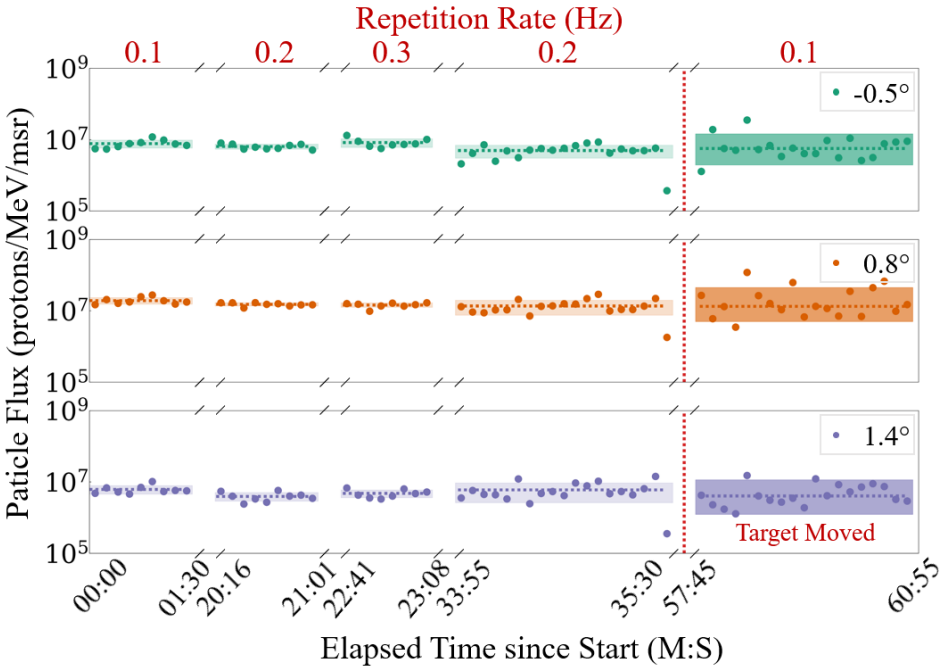

Figure 5.13: Particle flux at 10 MeV for all shots, with standard deviations ($\pm\sigma$) indicated by the shaded areas surrounding the mean (dotted lines). For the last 19 shots, where proton flux fluctuations exceed two orders of magnitude, the dotted lines represent the median, and the shaded regions reflect the interquartile range (IQR).

5.2.2 Consecutive shots

Based on previous tests, over 400 consecutive shots were conducted at a repetition rate of 0.1 Hz on the middle segment of water-leaf targets during the beamtime on 20240808. For this experimental campaign, The total flow rate of water jets was increased to 3.2 ml/min, resulting in a longer target with a thickness of approximately 3 µm (with an uncertainty of ±5%) in this central region. Proton bunches were continuously generated with laser energy between 9.8 J and 10.1 J.

In contrast to the configuration shown in Fig. 3.14(a), the distance between the nozzles was minimized, because this resulted in smaller misalignment of the water-leaf target during shots based on observations. Additionally, reflections of a CW laser, which followed the same optical path as the ATLAS-3000, were monitored from the target. If any detuning was detected, adjustments were made by repositioning the nozzles using linear stages. This compensation process typically took only a few seconds, allowing for consistent 0.1 Hz operation.

The analysis focused on the -0.5° angle, close to the target normal direction, because at

this angle the detectable range of proton energies was broadest. Statistical analyses were conducted on the entire dataset, with the proton spectra presented in a waterfall plot in Fig. 5.14. This setup achieved a maximum proton energy of over 30 MeV and a peak flux of around 10^9 protons/MeV/msr, as depicted in Fig. 5.14. The gaps in the spectral data correspond to manual pauses in laser shooting due to the temporary non-operational state of the camera used for monitoring target alignment. These interruptions did not affect the consistency of the experimental setup or the subsequent data collection.

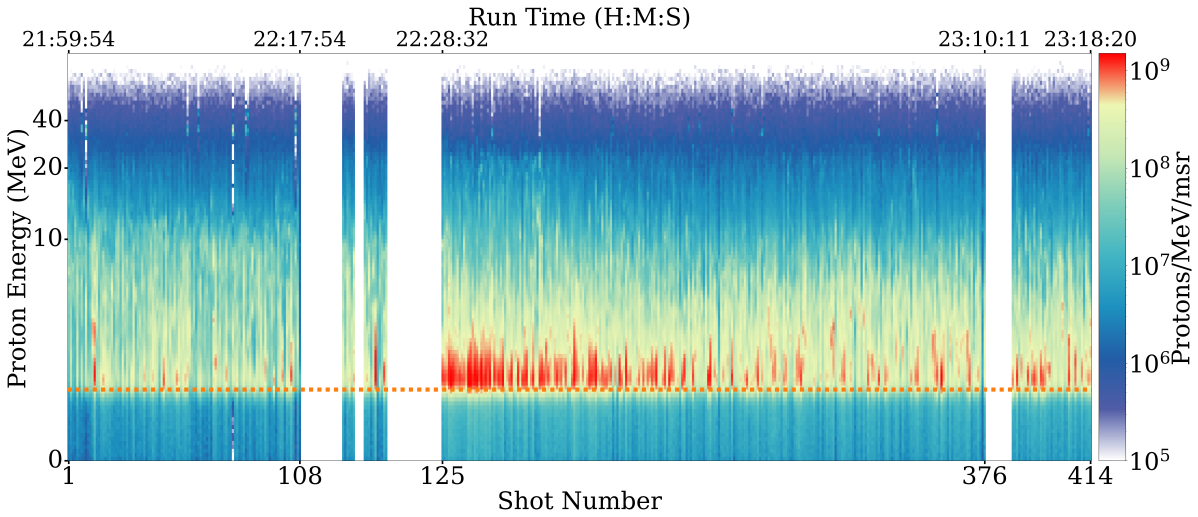

Figure 5.14: Proton spectra obtained from over 400 consecutive shots at a repetition rate of 0.1 Hz, with an average laser energy of 9.9 J, analyzed near the target normal direction (-0.5°). Data were collected over a duration of 1 hour, 18 minutes, and 26 seconds, with a total of 9 minutes and 26 seconds of recorded gaps. The gaps in the spectral data correspond to manual pauses in laser shooting due to the temporary non-operational state of the camera used for monitoring target alignment. The orange solid lines indicate the minimum detectable proton energy of 3.7 MeV, constrained by the presence of a phantom positioned in front of the detector. The maximum proton energy was up to 30 MeV, with a peak flux reaching approximately 10^9 protons/MeV/msr.

Figure 5.15 shows that the maximum proton energy averages to 22.0 MeV $\pm$ 3.1 MeV when taking all shots into account. The proton flux is evaluated at 17 MeV, since all shots delivered energies above this value, resulting in a flux of $(3.5 \pm 1.6) \times 10^6$ protons/MeV/msr. A Pearson correlation analysis was performed to examine the potential relationship between maximum proton energy and the corresponding particle yield at 17 MeV across all 400 shots. A Pearson correlation analysis was performed to examine the potential relationship between maximum proton energy and the corresponding particle

yield at 17 MeV across all 400 shots. The Pearson correlation coefficient was 0.6, indicating that the variations in maximum proton energy do exhibit a modest correlation with the particle flux at 17 MeV.

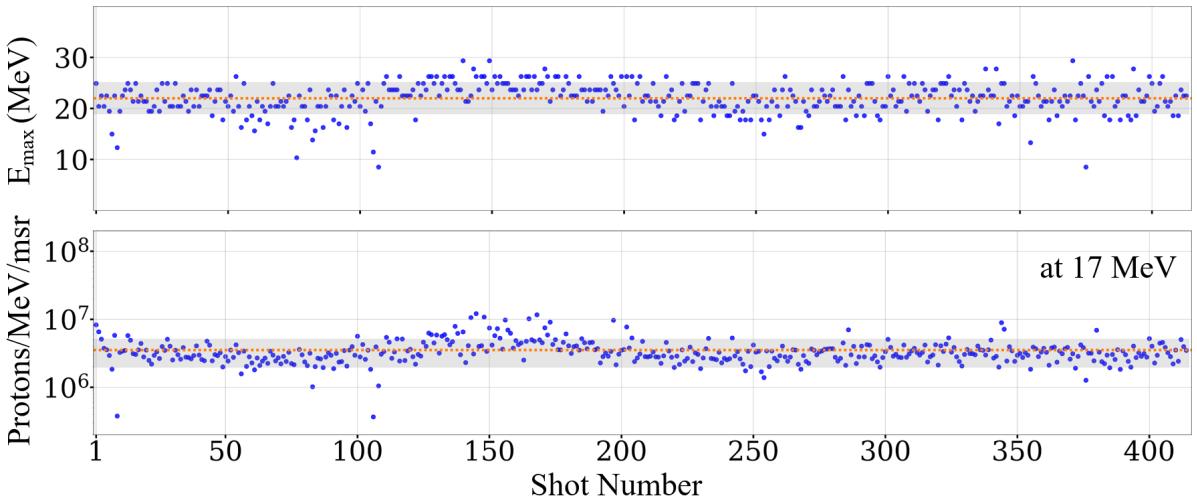

Figure 5.15: Statistical analysis of the maximum proton energy and proton flux at 16 MeV for all shots.

In Fig. 5.15, the particle flux at 17 MeV is highlighted. Further investigation of other selected energies in 1 MeV steps across the broad spectrum is warranted. Figure 5.16 facilitates this analysis through a rain-cloud plot, which provides an overview of the proton spectra variations across over 400 shots at a laser energy of 9.9 J. In this plot, the proton flux at a given energy, such as 10 MeV, is determined for each shot, resulting in data points (rain). The vertical filled curve (cloud) represents the histogram of these data points. Additionally, the data is presented as a boxplot, where the InterQuartile Range (IQR) contains 50% of the data points, serving as a visual indicator of variations in the data distribution. The orange lines within the IQR denote the median, offering insight into the central tendency of the dataset. The medians of the box plots reveal typical exponential energy spectra. Specifically, from 20 MeV to 10 MeV, the particle yield increases from 10^6 to 10^8 protons/MeV/msr.

An increasing trend in the number of shots falling below the detection threshold for higher proton energies is observed. Additionally, the Coefficient of Variation ($CV = \sigma/\mu$) is calculated for each energy and represented by the red solid curve. It ranges from 50% to 100%, with an average of 70%, and is minimal at around 17 MeV, corresponding to 77% of the average E_{max}.

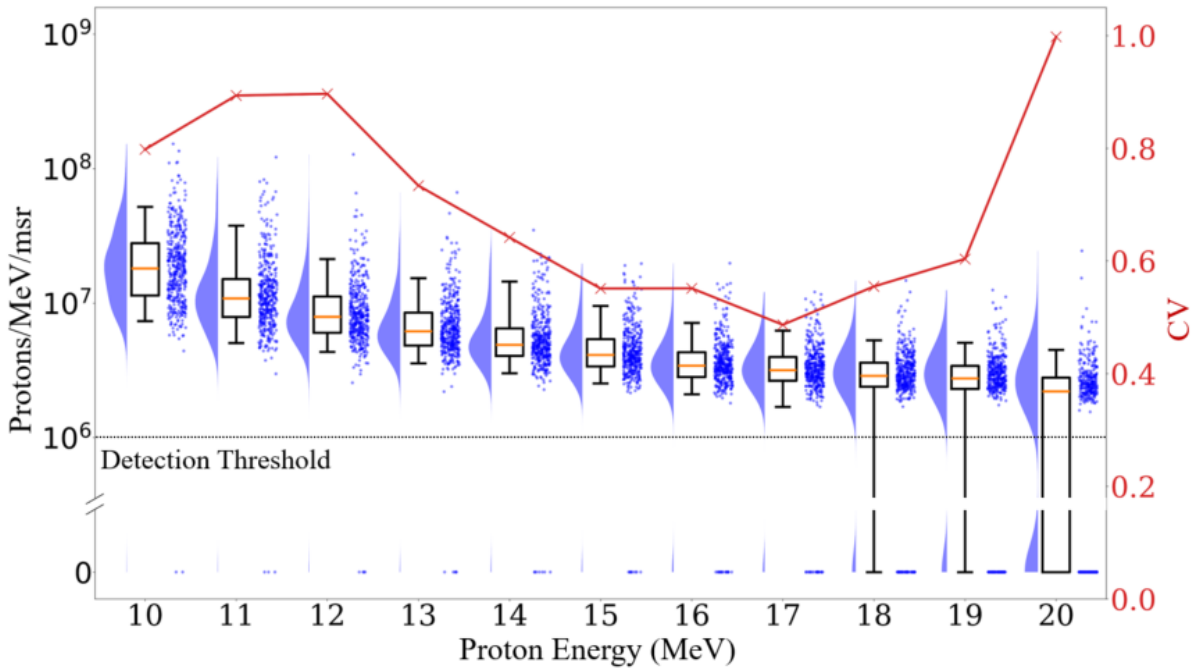

Figure 5.16: Probability density and discrete distribution of proton counts at specific energies across all shots. Rain plots are employed to reduce overlap and enhance the clarity of experimental data visualization. Each set of rain-cloud plots corresponds to the same energy level. The data set is also represented using half-violin (cloud) and box plots for statistical evaluation, with the whiskers of the box plots extending to [5%, 95%] of the data range. The red solid lines depict the coefficient of variation (CV) of the particle yield at specific energies, aligned with the right y-axis. The dotted line marks the detection threshold of the WASP.

5.3 Effect of laser pulse polarization on proton acceleration

The experimental setup, as illustrated in Fig. 4.1, includes a removable quarter WavePlate (WP) positioned between two tower mirrors, enabling the conversion of the linearly polarized laser beam into circular polarization as required. This configuration facilitates the investigation of laser pulse polarization effects on proton acceleration mechanisms. Typically, LP laser pulses accelerate protons predominantly through TNSA, while CP pulses facilitate RPA.

A dedicated beamtime using CP laser pulses was conducted on 20230516 with a laser energy of 6.4 J on target. Results from this experiment were compared with those from an

earlier beamtime on 20230825, which used a laser energy of 4.6 J on target but employed an LP pulse. The laser intensity remained consistent between the two experiments at 4.5×10^{20} W/cm^2, enabling a direct assessment of the influence of laser pulse polarization on proton acceleration.

Figure 5.17 provides a raw data comparison of proton spectra acquired from WASP for LP and CP pulses. Proton spectrum modulation is clearly observed with the CP laser pulse (Fig. 5.17 (a)), in contrast to the typical exponential decay spectrum associated with LP pulses (Fig. 5.17 (b)). This modulation is visible across the full RadEye detector, with the black dashed rectangular regions selected for proton spectrum reconstruction to facilitate further quantitative analysis, as they offer a broad energy detection range.

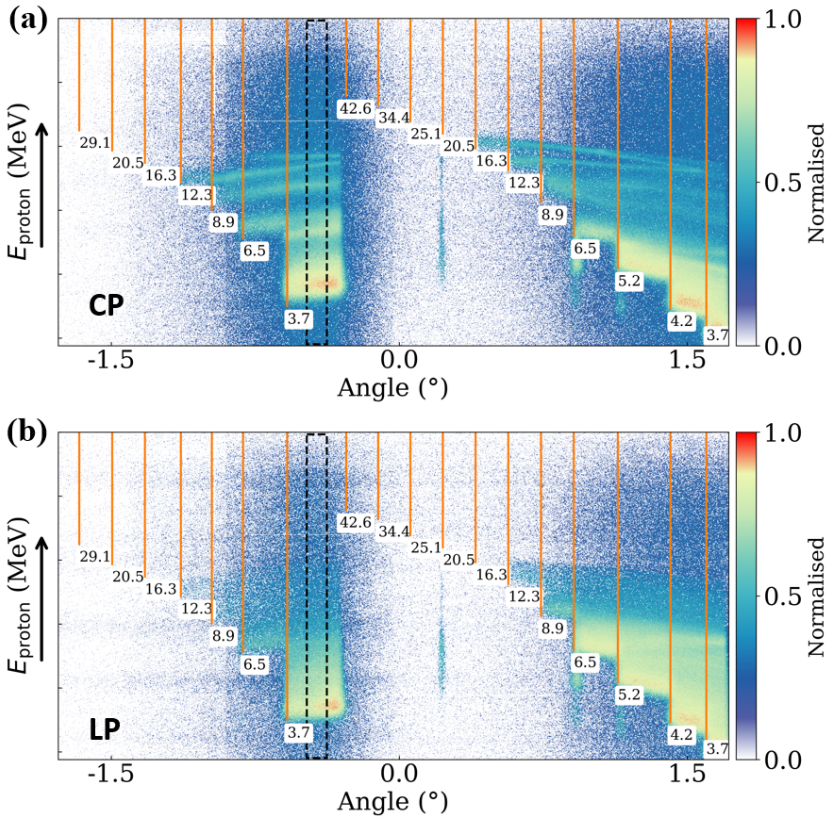

Figure 5.17: Raw WASP data showing proton spectra from interactions of LP and CP laser pulses at an intensity of 4.5×10^{20} W/cm^2 with water-leaf targets. The blue rectangular regions highlight areas used for spectrum reconstruction, with corresponding results presented in Fig. 5.18.

The reconstructed proton spectra are presented in Fig. 5.18. The spectrum generated by the LP laser pulse displays a typical exponential decay characteristic of TNSA, with a cutoff energy of 16 MeV. In contrast, the spectrum from the CP laser pulse exhibits

pronounced modulation with multiple peaks, achieving an order of magnitude higher particle flux at some proton energy values compared to the LP pulse.

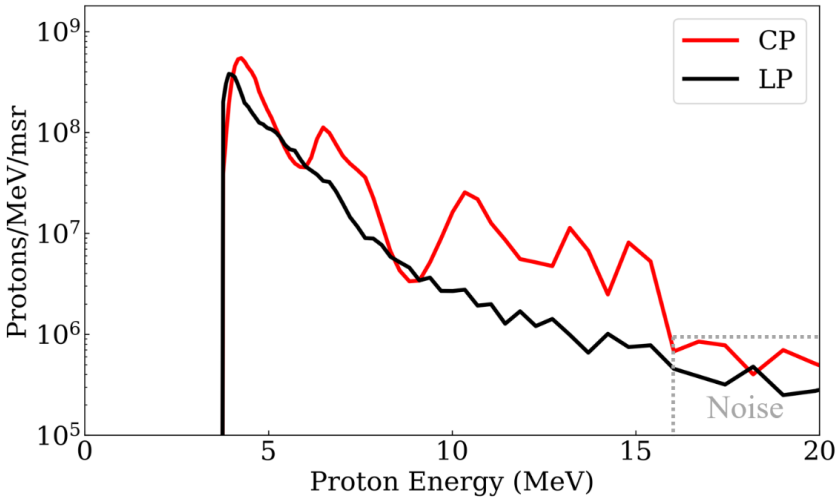

Figure 5.18: Proton spectra generated from the interaction of LP and CP laser pulses with water-leaf targets.

Chapter 6

Discussion

6.1 Target stability

The target system operated robustly in a vacuum for over 10 hours as long as no laser was fired. Laser shots resulted in the detuning of the water leaf. This effect became more pronounced with increasing laser energy but remained manageable and did not represent a fundamental operational limit. This instability can be likely attributed to two primary factors: Electromagnetic Pulse (EMP) effects and flow dynamics.

Electromagnetic Pulse (EMP): The intense laser-plasma interaction generates a strong EMP [193] that can interfere with the motorized stage used to position one of the nozzles near the interaction point. The motor, affected by the EMP, can cause unintended movements of the nozzle, leading to the rotation and instability of the target. Various strategies were explored to mitigate this EMP effect, if responsible, such as:
1) Shielding and Grounding: Attempts were made to shield the motor and other sensitive components from the EMP. Grounding techniques were also employed to dissipate the EMP energy.
2) Mechanical Isolation: Mechanical brakes and dampeners were used to physically stabilize the nozzle and motor assembly.
3) Electronic Filtering: Filters were added to the electronic circuits to block EMP-induced surges. Despite these efforts, the instability persisted, suggesting that the EMP effects were not the sole cause of the instability.

Flow Dynamics: The interaction of the laser pulse with the liquid leaf surface creates plasma, which disrupts the local flow dynamics, and this disruption might propagate to the nozzles. This disruption can lead to instability, particularly at higher laser energies. Two critical aspects were identified:
1) Plasma Formation: When the laser impacts the leaf, part of the energy is absorbed, creating plasma and breaking the flow. A sonic pressure wave is also launched from the interaction, which can propagate along the jets to the nozzles and destabilize the leaf,

especially at higher energies [162].
2) Flow Instability: Flow instability often starts with minor perturbations, including friction between the nozzle and the liquid jet, and grows over time [194, 195]. Even with perfectly symmetrical jets and no pump pulsation, instabilities along the target and turbulence induced by laser shots can significantly affect target stability. The initial setup had the nozzles placed around 2 mm apart, creating a 3 mm free jet. This setup was intended to protect the nozzles from damage but inadvertently contributed to instability. It was observed that the instability was stronger for a larger distance.

To address the flow dynamics issue, the distance between the nozzles was adjusted, allowing the jets to collide close to the exit. This modification significantly suppressed the instability, resulting in a more stable target during shots. Experimental results confirmed the stability of the target under laser shots at the same energy level, and the nozzles functioned more reliable throughout the beamtime.

In conclusion, while the target instability at higher laser energies presents challenges, it does not seem to be an insurmountable limitation. Potential causes of the instability have been identified and the first tests were performed. Future work will focus on refining these solutions to enable high repetition rate operations and further improve target stability. This will likely require dedicated experiments to visualize the shock and plasma and its impact on the nozzles.

6.2 Strategy for optimal proton acceleration

The optimization of proton acceleration in laser-driven experiments involves careful consideration of several key parameters. The dependence of maximum proton energy (E_{max}) on laser intensity (I) follows the relation $E_{max} \propto I^{\alpha}$ ($\alpha \approx 0.5$ for TNSA, $\alpha \approx 1.0$ for RPA). Theoretically, for laser systems with constant pulse energy (E_L) and pulse duration (τ), E_{max} should be optimized when the target is positioned at the laser's focal plane. However, experimental results from focus and defocus scans, as presented in Section 5.1.2, deviate from this expectation, with the highest average E_{max} consistently achieved at out-of-focus positions.

Two reasons are proposed to explain this deviation. First, inaccuracies in determining the laser focal plane using an attenuated pulse may persist even after compensating for attenuation effects. Second, the self-focusing effect induced by preplasma formation could play a significant role, with E_{max} potentially maximized when the intense laser pulse focuses near the critical density (n_c) of the preplasma formed ahead of the target.

A thorough understanding of the underlying cause would require the implementation of advanced, on-shot diagnostics.

Despite the unresolved underlying mechanism, the optimal target position for maximizing proton energy can still be identified through focus and defocus scans prior to each experimental run. This method remains effective regardless of uncertainties related to focus determination or preplasma effects. This means, that E_{max} can be optimized for applications. The physical reason for the optimal position remains unclear though.

Target-thickness is another critical parameter in laser-driven proton acceleration. Thickness scan results demonstrate a clear trend of higher maximum proton energies achieved with thinner targets. These findings align with previous studies suggesting the existence of an optimal target thickness for ion acceleration under specific experimental conditions. Based on the current laser parameters and results, the optimal thickness is anticipated to be in the sub-micron range or hundreds of nanometers.

The model presented by Hasson and Peck [146] offers several methods to achieve a thinner target. Increasing the flow rate can extend the target length, allowing the interaction to occur at a lower segment of the target, effectively reducing the target thickness by increasing the parameter r in Eq. 3.11. However, this approach has drawbacks: a longer or larger target increases surface area, enhancing vapor evaporation and placing additional strain on the vacuum pump system. Additionally, a higher flow rate increases the Reynolds number (Re), potentially reducing target stability. Interactions with targets at lower segments have been observed to exhibit poor stability in proton acceleration performance.

A more practical approach to achieving thinner targets involves using nozzles with smaller inner diameters, despite the increased alignment precision required and the potential for clogging. Previous research has demonstrated the successful generation of a 200 nm water sheet using a pair of nozzles with a 10-micrometer diameter [165].

6.3 Scaling law

The angular resolution provided by the WASP facilitated an examination of energy scaling at different angles relative to the target normal. The analysis included angles of -0.5°, 0.8°, and 1.4°, as shown in Fig. 5.1. The scaling relationship at -0.5° $E_{\max} = 5.28 \cdot E_L^{0.59}$, aligns well with the scaling at 1.4° $E_{\max} = 5.60 \cdot E_L^{0.57}$, indicating a broader overall proton divergence. These results closely match the empirical scaling law proposed by Zimmer, $E_L^{0.59}$ [196]. However, at 0.8°, the energy scaling deviates, following $E_{\max} = 7.85 \cdot E_L^{0.41}$.

This discrepancy is likely an artifact and due to the presence of an aluminum phantom in front of the detector.

The thicknesses of the aluminum strips are 112 µm, 512 µm, and 142 µm at -0.5°, 0.8°, and 1.4°, respectively, corresponding to proton energy thresholds of 3.7 MeV, 8.9 MeV, and 4.2 MeV. The thicker aluminum strips at 0.8° increase the detectable energy threshold, filtering out lower-energy proton bunches, especially for lower laser energies. This can result in systematic errors. For example, at 0.8°, the RadEye detector could only detect protons with energies exceeding 8.9 MeV. As a result, no data was recorded for a laser energy of 1.1 J, and for 1.9 J, only two shots with proton energies exceeding 9 MeV were detected. This led to an artificially high average maximum proton energy (9.9 MeV) for the lower laser energies, resulting in a weaker energy scaling compared to the other two angular positions. Despite this systematic error, the thicker aluminum strip at 0.8° effectively reduced background noise, resulting in a smaller standard deviation of ± 0.03.

Larger fluctuations in maximum proton energy and flux were observed at laser energies exceeding 3 J, despite the experiment being conducted in shot-on-demand mode with consistent target conditions and stable laser energy (maintained to within 1%). These fluctuations were primarily attributed to stochastic shot-to-shot variations in the laser system, likely influenced by unaccounted parameters such as contrast, focus drift, and wavefront distortions.

It is of interest to discuss the scaling law in terms of not only the laser energy but also focus spot size, as laser peak intensity is an integrated parameter given by $I_0 = 0.83 E_L / t_{FWHM} \cdot d_{FWHM}^2$. Figure 6.1 illustrates this relationship, presenting the scaling laws derived from the energy scan ($E_{max} \propto I_0^{0.57} \propto E_L^{0.57}$) and out-of-focus scan ($E_{max} \propto I_0^{0.25} \propto d_{FWHM}^{-0.50}$) represented by blue and pink solid lines, respectively. These relationships show good agreement with the empirical scaling law proposed by Zimmer et al. [196], $E_{max} \propto E_L^{0.59} \cdot d_{FWHM}^{-0.58}$.

Note that E_{max} does not scale equally with the components of peak intensity, as expected by the scaling exponents (0.57 for laser energy and -0.50 for focus spot size). This difference depends on how intensity was varied and suggests a complex interplay between laser parameters and proton acceleration mechanisms. This difference may be attributed to varying plasma conditions and proton acceleration processes as the laser focus changes. When the laser energy increases at a fixed spot size, the plasma density, temperature, and sheath field likely scale differently compared to when the spot size is varied at constant energy. These distinctions could lead to different optimal conditions

for proton acceleration.

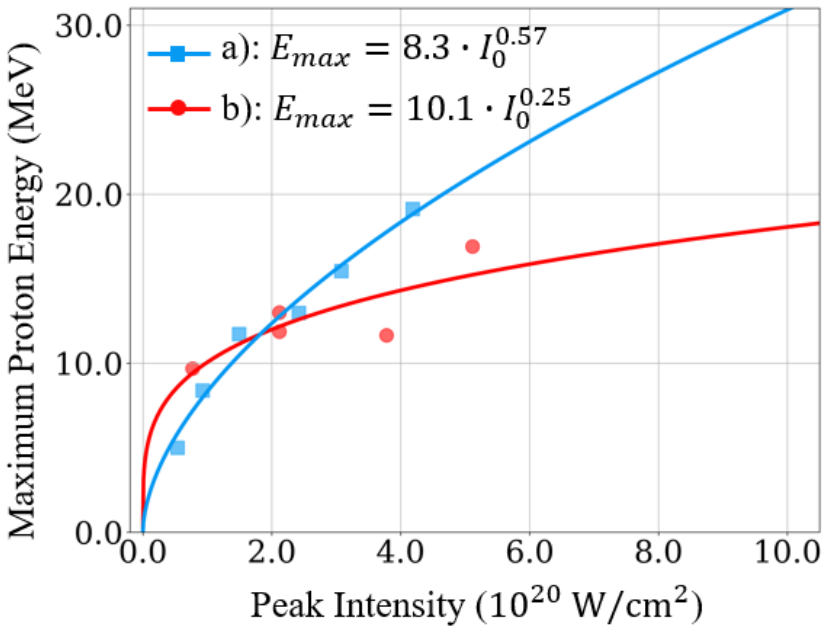

Figure 6.1: Maximum proton energy as a function of peak laser intensity. (a) Variation in intensity achieved by varying laser energy (E_L from 1.1 J to 8.4 J on target) with a fixed focus spot size on target (d_{FWHM} = 5.4 µm). (b) Variation in intensity achieved by adjusting focus spot size (d_{FWHM} from 5.4 µm to 14.1 µm), by positioning the target at different out-of-focus locations with constant laser energy (E_L = 10.3 J on target). Both scenarios were analyzed at 1.4°.

The weaker dependence on intensity in the out-of-focus scan might indicate a transition between different acceleration regimes or a saturation effect in the TNSA mechanism. As the laser spot size increases, the interaction area expands, potentially allowing for a larger number of protons to be accelerated. However, this expansion comes at the cost of reduced peak intensity, which may limit the maximum energy gain per proton.

In addition to comparing the scaling of maximum proton energy under variations in laser energy and target positioning at different out-of-focus positions, the scaling of total proton flux across all energies and the proton flux at 10 MeV was also investigated, as shown in Fig. 6.2. The results reveal a similar trend, where the dependence on laser energy is significantly stronger.

Interestingly, the intersections of all scalings in Fig. 6.1 and Fig. 6.2 (maximum proton energy, proton flux across all energies, and proton flux at 10 MeV) are at a peak intensity of approximately 2×10^{20} W/cm^2. This corresponds to positioning the target out of

focus at ±100 µm, near the Rayleigh length of 80 µm. These findings indicate that the scaling of maximum proton energy and proton flux with peak laser intensity is dominated by laser energy outside the Rayleigh length and by focal spot size within the Rayleigh length.

These observed scaling laws have important implications for optimizing laser-driven proton sources. While increasing laser energy provides a more direct path to higher proton energies, the results suggest that careful control of the focal spot size could offer an alternative method for fine-tuning the proton beam characteristics. This could be particularly useful in scenarios where increasing laser energy is not feasible or cost-effective.

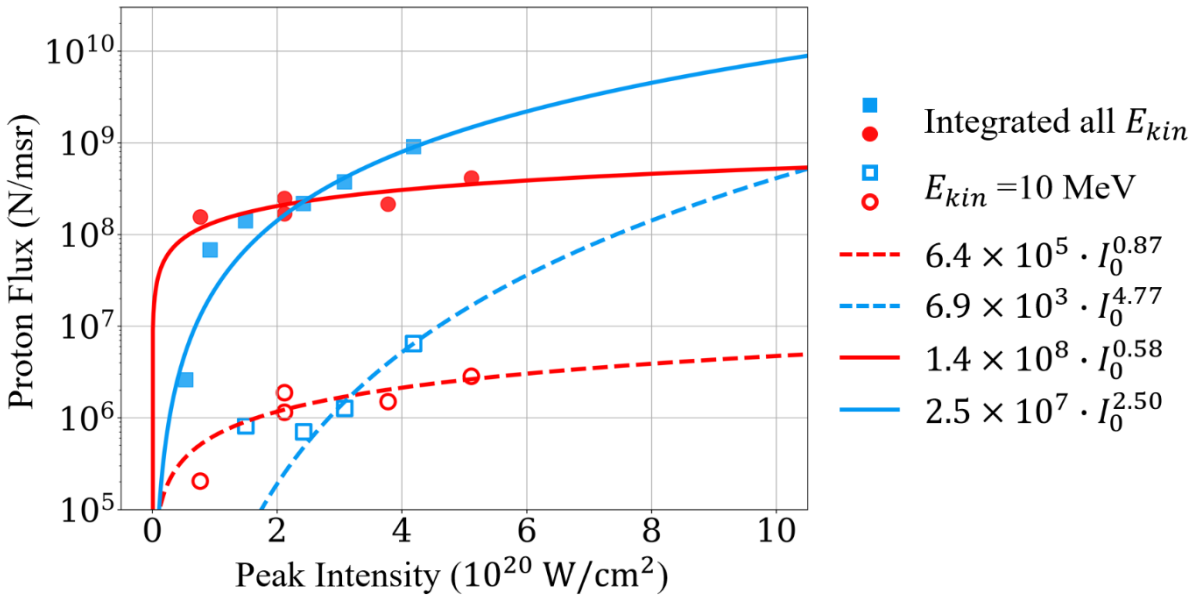

Figure 6.2: Proton flux as a function of peak laser intensity. Solid symbols represent the total proton flux integrated across all energies, while empty symbols indicate the proton flux specifically at 10 MeV, both as functions of peak laser intensity. The blue color corresponds to intensity variation achieved by varying laser energy (E_L from 1.1 J to 8.4 J on target) with a fixed focus spot size on target (d_{FWHM} = 5.4 µm). In contrast, the red color depicts intensity variations achieved by adjusting focus spot size (d_{FWHM} from 5.4 µm to 19.0 µm), by positioning the target at different out-of-focus locations with constant laser energy (E_L = 10.3 J on target). Both scenarios were analyzed at 1.4°.

6.4 Shot-to-shot variations

During the experimental campaign of shot-to-shot variations, proton bunch performance remained stable when targeting the middle segment of the water leaf with variations in repetition rate having no significant impact on the proton bunches. This stability is likely due to the 0.3 Hz operation rate being well below the resonance frequency of the water leaf [165], insufficient to induce substantial fluctuations in the position of the water leaf. However, the stability of proton flux degrades significantly relocating the laser-target interaction point to the lower (thinner) segment of the water leaf. This change increases the curvature of the target and decreases its horizontal size [165]. With a $\pm$ 10 µm jittering focus, the laser is more likely to interact with the thicker target rim, potentially causing fluctuations. Another potential reason for the fluctuations could be attributed to the growth instability along the water-leaf target or instability induced by turbulent hydrodynamics near the top of the catcher during laser shots. While targeting the lower segment of the water leaf is a straightforward method that allows expanding investigations to thinner targets, it comes with substantial fluctuations. Conversely, targeting the middle segment with higher laser pulse energy provides a viable alternative, offering improved stability and quality of the proton bunches.

To this end, a series of 400 shots were recorded at 0.1 Hz with an average laser energy of 9.9 J incident onto the middle of the water-leaf target, achieving higher proton maximum energy, enhanced particle flux, and improved shot-to-shot stability. The experiment was limited to over 400 shots solely due to time constraints as the campaign extended late into the evening. Remarkably, a maximum proton energy of 30 MeV was achieved, approximately one order of magnitude higher than previously reported with similar target assemblies [55–57]. For experimental designs requiring 4 MeV, the measured proton flux was approximately 1000 times higher than those reported in previous studies [56, 57]. Most importantly, Neither Puyuelo-Valdes et al [56] nor Treffert et al [57] observed protons at application-relevant energies, such as 17 MeV.

Table 6.1 highlights a comparison of key quantities of laser-proton acceleration using similar targets and tape-drive targets. For example, Puyuelo-Valdes et al [56] demonstrated 3.5 MeV protons with a laser pulse energy of 4 J, duration of 30 fs, and a focal spot size of 20 µm. Treffert et al [57] reported 4.4 MeV deuterons with a laser pulse energy of 5.5 J, duration of 45 fs, and a tight focus of 1.8 µm, i.e., an intensity exceeding 10^{21} W/cm^2. This suggests a complicated dependency, where the smallest focal spot and highest intensity may not necessarily yield the maximum ion energies.

The laser pulse energy appears to play the more important role [197]. The increase in maximum proton energy from 4 MeV to 30 MeV represents an increase in penetration depth in water from 0.3 mm to 8 mm, significantly expanding the range of potential applications. The realization of these advancements is not only a matter of increasing the laser energy but also of facing the technical challenges that come with it. These challenges include mitigating the interference from stronger electromagnetic pulses during laser-plasma interactions [193] and managing the increased sonic pressure that impacts target stability [162]. Despite these hurdles, the reproducibility and reliability of a proton source capable of long-term operation are demonstrated.

Reference	Dover et al. [198]	Puyuelo et al. [56]	Treffert et al. [57]	This work
Target	reeled tape	water leaf	heavy water leaf	water leaf
Ions	protons	protons	deuterons	protons
E_L (J)	10	4.0	5.5	9.9
d_{fwhm} (µm)	1.5	19.5	1.8	5.3
τ_{fwhm} (fs)	40	30	45	27
I_{peak} (W/cm^2)	5.0×10^{21}	4.0×10^{19}	1.2×10^{21}	1.1×10^{21}
l (µm)	5	5 ± 1 & 1 ± 0.5	5 ± 1	3 ± 0.2
E_{max} [Avg.] (MeV)	30 [26]	4.0 [3.5]	4.4 [N/A]	30 [22]
N/MeV/msr [4 MeV]	N/A	$\sim 10^6$	$\sim 10^6$	$\sim 10^9$
N/MeV/msr [17 MeV]	$\sim 10^6$	N/A	N/A	5×10^6
Consecutive shots	> 30	60	60	> 400

Table 6.1: Comparison of experimental parameters and results with previous studies

It is well established that thinner targets can increase proton energies and flux for a given laser pulse, with the minimum usable thickness determined by laser contrast. Achieving very thin targets presents significant challenges for tape-driven systems, which are prone to tearing. Although Dover et al. [198] reported similar results to our work, reliably shooting targets thinner than 5 µm with a tape system seems difficult. In contrast, the thickness of water-leaf targets can be reduced to 200 nm [165], presenting substantial advantages for more efficient ion acceleration mechanisms such as Radiation Pressure Acceleration (RPA) [118, 120, 122].

Another question arises regarding shot-to-shot variations in proton energy. If the variation of maximum energy $dE_{\max}$ was solely due to fluctuations of laser energy dE_L according to the established scaling, one would expect that $dE_{\max}/E_{\max} = 0.57 \cdot dE_L/E_L$. However, the observed relative variation of maximum proton energy, reaching up to 14% as shown in Fig. 5.15, exceeds what would be expected from the mere 0.5% variation in laser energy. This discrepancy suggests the influence of additional, yet unidentified

factors that warrant further investigation. Despite these variations, the maximum proton energy remained consistent throughout the experiment, underscoring the robustness and reproducibility of proton bunch generation, even under fluctuating laser system conditions and other so far uncontrollable parameters that typically degrade performance. However, the particle flux, particularly near the maximum proton energy, proved more sensitive to these degradations. This sensitivity often led to an increasing number of shots falling below the detection threshold for higher proton energies, causing the trend towards greater variation at higher proton energies as reflected by the CV value in Fig. 5.16. Based on the current findings, optimal performance and stability are likely to be achieved by selecting proton energies corresponding to 70% to 80% of average maximum energy E_{max}, where the CV is minimized. This strategy would help mitigate the impact of shot-to-shot variations and ensure more consistent output for practical applications.

6.5 Proton spectrum modulation

When changing the laser pulse from LP to CP, the proton spectrum displayed strong modulation. This experimental observation could be attributed to the presence of multiple ion species in the HB-RPA mechanism. When a CP laser pulse irradiates the target's front surface, the $\mathbf{v} \times \mathbf{B}$ force has no oscillating component and pushes electrons "gently" into the target. These electrons accumulate in a compressed layer, creating a charge-separation region and generating a localized spike in the electrostatic field that restrains them. This electrostatic field subsequently accelerates ions, eventually catching up with the compressed electron layer [124]. Macchi et al. [120] derived the maximum velocity $v_{max} = 2v_{i,HB}$ and acceleration time τ_i for this process:

$$\frac{v_{i,HB}}{c} = \sqrt{\frac{Z}{A}\frac{m_e}{m_i}\frac{n_c}{n_e}}a \quad \text{and} \quad \tau_i \simeq \frac{1}{\omega_L a}\sqrt{\frac{A}{Z}\frac{m_i}{m_e}}, \tag{6.1}$$

where $v_{i,HB}$ is ion velocity of HB-RPA. This relationship indicates that ions with varying charge-to-mass (Z/A) ratios exhibit distinct responses to the electrostatic field, leading to spatial separation. Protons, having the highest Z/A ratio, are accelerated first and attain the highest velocities, followed by O^{8+}, O^{7+}, O^{6+}, and so on. Additionally, the motion of adjacent heavy ion species generates Coulomb pistons, which further accelerate protons, resulting in a proton spectrum with multiple peaks.

The observed strong modulations in the proton spectrum are linked to the presence of ions with different charge states during radiation-pressure-assisted acceleration. Oxygen

ions with varying charge states sit at the dips in the proton spectrum in sequence (assumed to range from O^{3+} to O^{6+}), as shown in Fig. 6.3. A linear relationship between the charge state of oxygen ions and their corresponding kinetic energy was identified, $E_{o^{q+},\,max} = 2.9 \cdot q - 2.4$. While this relationship appears qualitatively consistent (linear) with Eq. 6.1, it does not align quantitatively, likely due to the challenges in accurately determining the realistic electron density distribution. At the same time, with a maximum proton energy of 16 MeV observed in Fig. 6.3, Eq. 6.1 predicts a maximum energy of only 6 MeV/u for O^{6+}, significantly lower than the experimentally observed value of 14 MeV. This hints at more complex acceleration mechanisms and warrants further investigation.

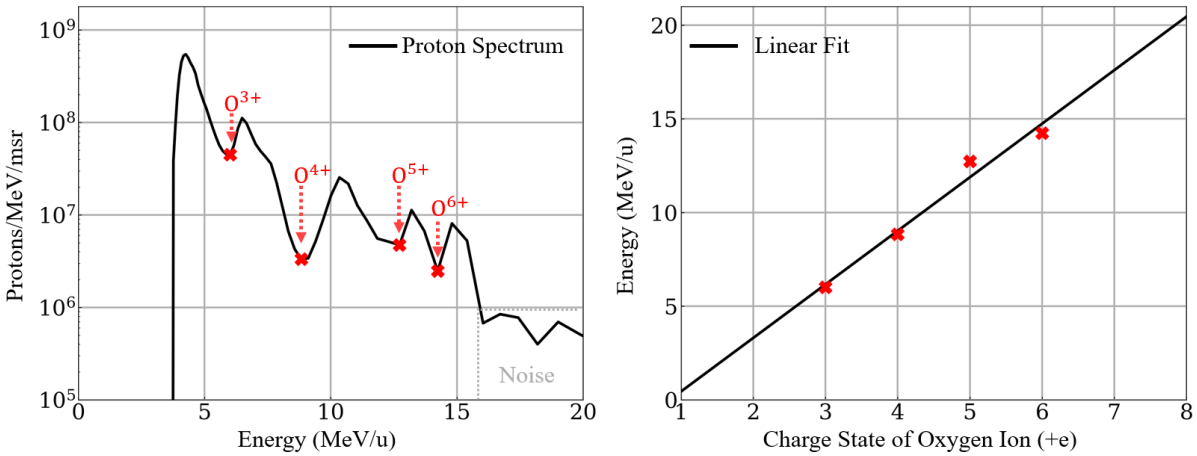

Figure 6.3: Proton spectrum modulations using CP Laser. (a) The modulated proton spectrum is attributed to oxygen ions with different charge states (assumed to range from O^{3+} to O^{6+}). (b) The relationship between the charge state of oxygen ions and their corresponding kinetic energy is displayed by a linear fit.

The WASP used in this study is limited to detecting only protons, leaving oxygen ions only for very large energies observable. To overcome this constraint and gain a more comprehensive understanding of the acceleration process, a Thomson Parabola Spectrometer (TPS) would be necessary to directly observe the energy modulation of various ion charge state, providing crucial validation of the HB-RPA mechanism and its effects on proton spectrum modulation. Furthermore, comparing these experimental results with detailed Particle-In-Cell (PIC) simulations could provide a more comprehensive understanding of the underlying physics. Such simulations could help identify the relative contributions of different acceleration mechanisms, such as HB-RPA, TNSA, and Coulomb explosion, and the role of multiple ion species in shaping the final proton spectrum.

Chapter 7

Summary and Outlook

7.1 Results of the thesis

In this thesis, a high-repetition-rate water-leaf target has been developed and integrated into the laser-ion acceleration end station of CALA. A comprehensive set of experiments was performed to study the behaviour under realistic experimental conditions and deepen the understanding of the underlying physics of laser-driven ion acceleration. These experiments demonstrate the feasibility of operating proton sources with continuously replenishing targets, achieving proton energy levels applicable to a broad spectrum of scientific and industrial applications.

A key result of this thesis is the successful demonstration of operating a water-leaf target system in a vacuum environment, with background pressures ranging from 1.0×10^{-4} to 1.0×10^{-3} mbar, for durations exceeding 10 hours. The target system exhibited a high degree of positional control, enabling precise adjustments prior to each shot. This facilitated comprehensive scans of the target position, including axial movements along the laser beam, vertical adjustments to vary the target thickness (ranging from 2 µm to 20 µm), and corrections for rotational misalignments between shots. In particular, the misalignment after shots warrants further investigation.

Such flexibility played a crucial role in identifying the optimal interaction position that resulted in large proton energy, particle yield, and stable operation. A detailed experimental investigation using the ATLAS-3000 laser system demonstrated promising performance, yielding proton bunches comparable to that achieved with plastic foil targets of several hundred nanometers in thickness.

The maximum proton energy, an essential quantity for optimizing state-of-the-art laser-ion acceleration follows the empirical model proposed by Zimmer et al. [196]. The experimental results demonstrate that with 300 TW-class ultrashort pulse lasers and micron-thick targets, proton bunches can be accelerated to energies of up to 30 MeV. As a conservative estimate, the observed scaling implies the potential to generate over

60 MeV protons with the full ATLAS-3000 energy of 60 J on target, assuming identical target thickness and focal spot size. Recent advancements demonstrated with plastic targets suggest that further improvements in proton energy and stronger scaling could be realized through optimized target thickness [19].

Besides aiming for higher kinetic energies, the challenge of generating reproducible ion bunches and transitioning from singular proof-of-principle investigations to sustainable, repetitive operation remains a limitation for all applications of laser-driven ion acceleration. The experiments discussed in Section 5.2 address such shot-to-shot variations in proton bunch generation. The experimental findings demonstrate that repetition rate is not a limiting factor for achieving stable proton output. However, details matter, e.g., targeting the lower segment of the water-leaf target introduced fluctuations in the stability of the proton bunches. For example, the overall target stability was significantly improved by decreasing the distance between the nozzles. The most significant achievement is the reproducible, high-repetition-rate generation of proton bunches from a water-leaf target, achieving maximum proton energies of up to 30 MeV (average at 22 MeV) with 10 J of laser energy on target.

In addition to this technical milestone, the effect of laser pulse polarization on proton acceleration was investigated experimentally. This study provides comprehensive investigation of the relationship between spatial separation of multiple ion species and the formation of multiple peaks in the proton spectrum during the HB-RPA stage. This phenomenon has been corroborated through both experimental results and an analytical model, offering a novel insight into the complex dynamics of laser-driven ion acceleration.

7.2 Future perspectives

7.2.1 Enhanced proton acceleration via controlled prepulse

The generation of laser-driven proton acceleration for radiotherapy applications requires increasing the proton energy to E_{max}>200 MeV. Despite the anticipated full energy utilization of advanced laser systems like ATLAS 3000, existing scaling laws suggest that this threshold remains challenging to achieve. However, modifying key parameters such as target thickness, laser pulse characteristics, and pre-plasma conditions may alter these scaling relationships, potentially leading to more efficient acceleration mechanisms. Recent research demonstrates that micrometer-scale pre-plasmas generated in front of the target can significantly enhance proton acceleration [199–204]. Notably, a threefold

increase in proton cut-off energy has been achieved by introducing a micrometer scale-length pre-plasma via a low-energy femtosecond pre-pulse [204]. The plasma gradient at the vacuum-target interface plays a critical role in this enhancement, as it strongly influences the laser absorption dynamics and subsequently shapes the energy distribution of the heated electrons, which in turn generate the accelerating field for ions.

Future experiments should focus on controllable prepulse conditions to further optimize this process. The experimental setup will utilize a beam splitter to create a prepulse, with adjustable time delay, intensity, and mode, as illustrated in Fig. 7.1. Of particular interest is the introduction of a Laguerre-Gaussian (LG) prepulse using a vortex retarder or spiral phase plate [205], which can produce an isolated water-leaf target surrounded by an annular plasma. This configuration resembles a mass-limited target scenario [206], potentially significantly enhancing proton acceleration while simultaneously protecting the nozzles from laser shot effects and suppressing target detuning. By carefully controlling these pre-plasma conditions, it may be possible to enhance the energy coupling between the laser pulse and the target, ultimately improving the maximum attainable proton energies close to the requirements of proton therapy.

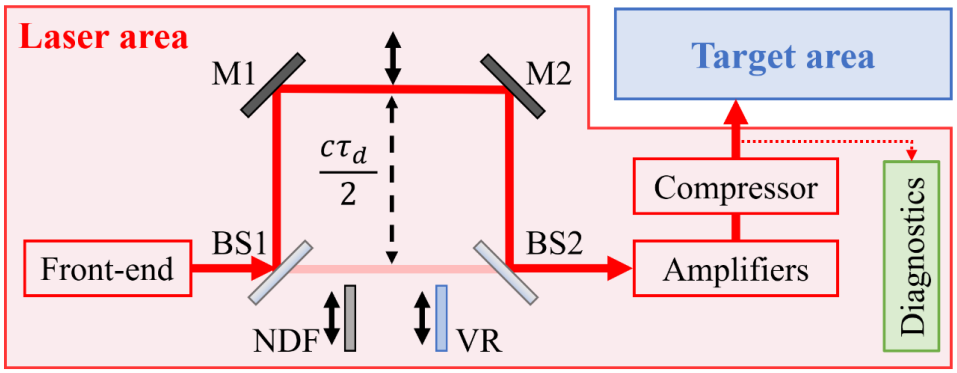

Figure 7.1: Schematic of controlled prepulse generation. A Beam Splitter (BS1) transmits a small fraction of the pulse energy, while the majority is reflected and directed to the beam combiner (BS2) for subsequent amplification, compression, and delivery to the target area. The time delay τ_d is adjusted using a motorized delay stage where mirrors (M1 and M2) are installed. The intensity and mode of prepulse are varied by inserting neutral density filters (NDFs) to control energy, and a vortex retarder (VR) to produce a LG prepulse. The laser area is highlighted in light red, the target region in light blue, and the diagnostic area in green. The diagnostics include measurements of the laser pulse duration, temporal contrast, and spectral map.

7.2.2 Proton acceleration optimization via machine learning

Optimizing laser-plasma interactions requires a thorough understanding of the underlying physics and accurate modeling of the complex plasma response to applied laser pulses. This task is challenging due to the highly nonlinear, multi-scale, and multi-physics nature of laser-plasma dynamics. Recent advances in high-repetition-rate laser operation and targetry now allow the generation of extensive datasets, enabling the application of data-driven models. These models can complement traditional theoretical and empirical approaches, offering fresh insights into the intricate dynamics of laser-plasma interactions. Machine learning techniques have become valuable tools in this field, allowing for the efficient analysis of large datasets and the development of predictive models. By utilizing these data-driven approaches, researchers can address some of the limitations of traditional modeling, resulting in enhanced optimization strategies for laser-plasma accelerators. Figure 7.2 illustrates an example of a machine-learning workflow applicable to general laser-plasma interaction configurations, with a more detailed review provided in [207].

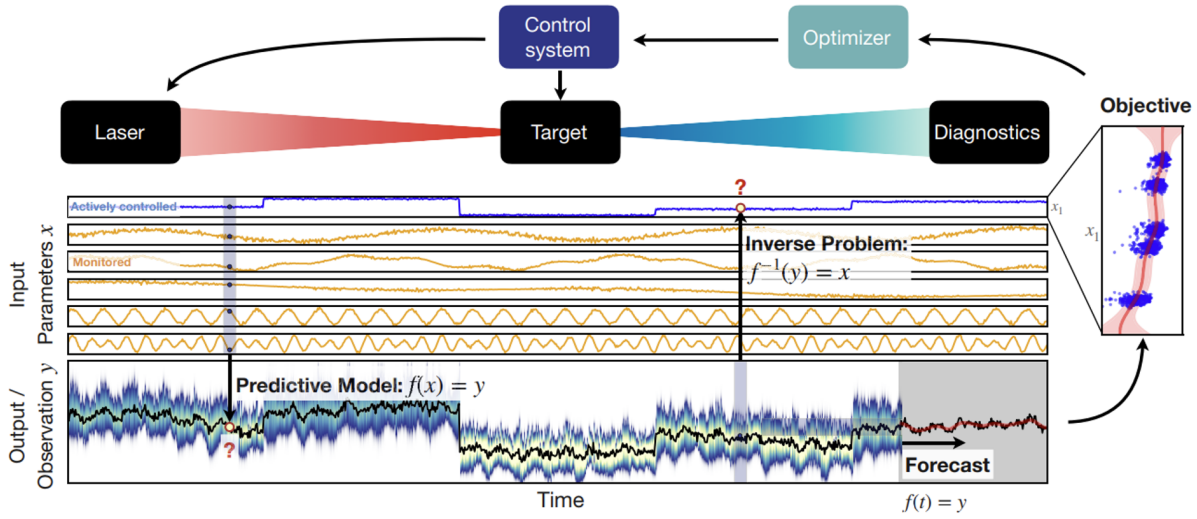

Figure 7.2: Machine-learning workflow applicable to general laser-plasma interaction configurations. Predictive models use known input parameters x to estimate output values y. In certain cases, deriving initial conditions from target outputs is required (inverse problem), while in others, tracking the system's temporal evolution may be of interest (forecast). Outputs generated from observations or models are used to optimize specific objectives, which are then fed back into the control system to refine input parameters. The figure is copied from Döpp et al. [207] and licensed under the *Creative Commons CC-BY-NC-ND.*

A promising direction for future research in proton bunch optimization is the development of auto-optimized laser systems and self-aligning target systems based on machine learning techniques. This capability would exploit the increased repetition rate offered by modern laser systems and pave the way for the integration of feedback loops and fine-tuning of laser and target parameters to meet proton bunch performance requirements for applications. Achieving this optimization requires establishing correlations between proton bunch characteristics (output) and target and laser parameters (input) through the use of real-time, full-power diagnostics. This integrated approach combining advanced diagnostics, machine learning, and optimization techniques holds significant potential for advancing the field of laser-plasma accelerators in general and ion acceleration in particular.

7.2.3 Potential of water-leaf targets

The potential of thin liquid leaf targets in vacuum environments is an emerging area of research with significant promise. Although these targets are not yet highly efficient for proton acceleration, their refreshing nature provides a crucial advantage in experimental setups where frequent target replacement is required. This continuous surface renewal makes them particularly suitable for high-repetition-rate laser-plasma interactions, enabling stable operation over extended periods without interruptions.

Their unique properties extend their applicability beyond proton acceleration. Thin liquid leaf targets hold significant promise for a wide range of applications, including neutron generation, X-ray and terahertz spectroscopy, High Harmonic Generation (HHG), and their use as plasma mirrors. These capabilities highlight their versatility and potential for advancing laser-plasma research.

The findings presented in this thesis aim to contribute to the growing understanding of thin liquid leaf systems and their potential in advanced laser-plasma experiments. By offering insights into the design, operation, and optimization of these targets, this work seeks to support researchers in developing their own systems and exploring innovative applications.

Publications and Conference Contributions

1 Peer-Reviewed Publications

1. **L. R. He**, M. Bachhammer, F. Balling, S. Biswas, L. Doyle, S. Gerlach, I. Hofrichter, M. Kharbedia, J. Liese, M. De Marco, T. Pohle, A. Praßelsperger, A.-K. Schmidt, F. Schweiger, M. F. Kling, S. Karsch, and J. Schreiber. "Variability Assessment of a 300 TW Laser-Driven Water-Leaf Proton Source." *Submitted to Physical Review X*, 2024.

2 Conference Contributions

1. **Oral:** Experimental Study of Proton Acceleration using Water Leaf Targets. *37th European Conference on Laser Interaction with Matter (ECLIM)*, Lisbon (Portugal), 2024.

2. **Poster:** Laser-Driven Proton Acceleration from Water-Leaf Targets at CALA. *10th International Conference on Ultrahigh Intensity Lasers (ICUIL)*, island of Cozumel (Mexico), 2024.

3. **Poster:** Enroute to Automated Optimization of Laser-Ion Acceleration. *LPA Special Workshop on Intelligent Systems*, Oxford (United Kingdom), 2025. *(co-author)*

4. **Poster:** Laser-driven Ion Acceleration at the Centre for Advanced Laser Applications. *LPA Special Workshop on Intelligent Systems*, Oxford (United Kingdom), 2025. *(co-author)*

5. **Oral:** Development of a thin liquid jet for ultrafast spectroscopy. *5th Targetry for High Repetition Rate Laser-Driven Sources Workshop (TARG)*, Dresden (Germany), 2021. *(co-author)*

Bibliography

[1] Vladimir I Veksler. Coherent principle of acceleration of charged particles. *Proc. CERN Symp. of High Energy Accelerators and Pion Physics (Geneva, Switzerland)*, 1:80–83, 1956. DOI: 10.1007/BF01491001.

[2] Theodore H Maiman et al. Stimulated optical radiation in ruby. *Nature*, 187:493–494, 1960. DOI: 10.1038/187493a0.

[3] John Nuckolls, Lowell Wood, Albert Thiessen, and George Zimmerman. Laser compression of matter to super-high densities: Thermonuclear (ctr) applications. *Nature*, 239(5368):139–142, 1972. DOI: 10.1038/239139a0.

[4] DR Bach, DE Casperson, DW Forslund, SJ Gitomer, PD Goldstone, A Hauer, JF Kephart, JM Kindel, R Kristal, GA Kyrala, et al. Intensity-dependent absorption in 10.6-μm laser-illuminated spheres. *Physical review letters*, 50(26):2082, 1983. DOI: 10.1103/PhysRevLett.50.2082.

[5] SJ Gitomer, RD Jones, F Begay, AW Ehler, JF Kephart, and R Kristal. Fast ions and hot electrons in the laser-plasma interaction. *The Physics of fluids*, 29(8):2679–2688, 1986. DOI: 10.1063/1.865510.

[6] Donna Strickland and Gerard Mourou. Compression of amplified chirped optical pulses. *Optics communications*, 55(6):447–449, 1985. DOI: 10.1016/0030-4018(85)90120-8.

[7] Nobuhiko Sarukura, Yuzo Ishida, and Hidetoshi Nakano. Generation of 50-fsec pulses from a pulse-compressed, cw, passively mode-locked Ti: sapphire laser. *Optics letters*, 16(3):153–155, 1991. DOI: 10.1364/OL.16.000153.

[8] Thomas Brabec, Ch Spielmann, PF Curley, and Ferenc Krausz. Kerr lens mode locking. *Optics letters*, 17(18):1292–1294, 1992. DOI: 10.1364/OL.17.001292.

[9] Peter F Moulton. Spectroscopic and laser characteristics of Ti: Al_2O_3. *JOSA B*, 3(1):125–133, 1986. DOI: 10.1364/JOSAB.3.000125.

[10] Colin N Danson, Constantin Haefner, Jake Bromage, Thomas Butcher, Jean-Christophe F Chanteloup, Enam A Chowdhury, Almantas Galvanauskas, Leonida A Gizzi, Joachim Hein, David I Hillier, et al. Petawatt and exawatt class lasers worldwide. *High Power Laser Science and Engineering*, 7:e54, 2019. DOI: 10.1017/hpl.2019.36.

[11] National Academies of Sciences, Engineering, and Medicine and Division on Engineering and Physical Sciences and Board on Physics and Astronomy and Committee on Opportunities in the Science, Applications, and Technology of Intense Ultrafast Lasers. *Opportunities in Intense Ultrafast Lasers: Reaching for the Brightest Light*. National Academies Press, 2018. Link: books?id=2f5JDwAAQBAJ.

[12] ELI. https://www.eli-beams.eu/research/ultrahigh-intensity-interactions/, accessed: 2024-10-01.

[13] Yuxing Han, Zhaoyang Li, Yibin Zhang, Fanyu Kong, Hongchao Cao, Yunxia Jin, Yuxin Leng, Ruxin Li, and Jianda Shao. 400nm ultra-broadband gratings for near-single-cycle 100 petawatt lasers. *Nature Communications*, 14(1):3632, 2023. DOI: 10.1038/s41467-023-39164-3.

[14] A Dubietis, G Jonušauskas, and A Piskarskas. Powerful femtosecond pulse generation by chirped and stretched pulse parametric amplification in bbo crystal. *Optics Communications*, 88(4-6):437–440, 1992. DOI: 10.1016/0030-4018(92)90070-8.

[15] AP Fews, PA Norreys, FN Beg, AR Bell, AE Dangor, CN Danson, P Lee, and SJ Rose. Plasma ion emission from high intensity picosecond laser pulse interactions with solid targets. *Physical review letters*, 73(13):1801, 1994. DOI: 10.1103/PhysRevLett.73.1801.

[16] RA Snavely, MH Key, SP Hatchett, TE Cowan, Markus Roth, TW Phillips, MA Stoyer, EA Henry, TC Sangster, MS Singh, et al. Intense high-energy proton beams from petawatt-laser irradiation of solids. *Physical review letters*, 85(14):2945, 2000. DOI: 10.1103/PhysRevLett.85.2945.

[17] F Wagner, O Deppert, C Brabetz, P Fiala, A Kleinschmidt, P Poth, VA Schanz, A Tebartz, B Zielbauer, M Roth, et al. Maximum proton energy above 85 mev from the relativistic interaction of laser pulses with micrometer thick CH_2 targets. *Physical review letters*, 116(20):205002, 2016. DOI: 10.1103/PhysRevLett.116.205002.

[18] Adam Higginson, RJ Gray, Martin King, RJ Dance, SDR Williamson, NMH Butler, Robbie Wilson, Rémi Capdessus, Chris Armstrong, JS Green, et al. Near-100 mev protons via a laser-driven transparency-enhanced hybrid acceleration scheme. *Nature communications*, 9(1):724, 2018. DOI: 10.1038/s41467-018-03063-9.

[19] Tim Ziegler, Ilja Göthel, Stefan Assenbaum, Constantin Bernert, Florian-Emanuel Brack, Thomas E Cowan, Nicholas P Dover, Lennart Gaus, Thomas Kluge, Stephan Kraft, et al. Laser-driven high-energy proton beams from cascaded acceleration regimes. *Nature Physics*, pages 1–6, 2024. DOI: 10.1038/s41567-024-02505-0.

[20] J. Schreiber. *Ion Acceleration driven by High-Intensity Laser Pulses*. PhD thesis, Ludwig-Maximilians-Universität München, 2006.

[21] EL Clark, K Krushelnick, JR Davies, Matthew Zepf, M Tatarakis, FN Beg, A Machacek, PA Norreys, MIK Santala, I Watts, et al. Measurements of energetic proton transport through magnetized plasma from intense laser interactions with solids. *Physical Review Letters*, 84(4):670, 2000. DOI: 10.1103/PhysRevLett.84.670.

[22] Anatoly Maksimchuk, Shaoting Gu, Kirk Flippo, Donald Umstadter, and V Yu Bychenkov. Forward ion acceleration in thin films driven by a high-intensity laser. *Physical Review Letters*, 84(18):4108, 2000. DOI: 10.1103/PhysRevLett.84.4108.

[23] K Krushelnick, EL Clark, Matthew Zepf, JR Davies, FN Beg, A Machacek, MIK Santala, M Tatarakis, I Watts, PA Norreys, et al. Energetic proton production from relativistic laser interaction with high density plasmas. *Physics of Plasmas*, 7(5):2055–2061, 2000. DOI: 10.1063/1.874027.

[24] TE Cowan, J Fuchs, H Ruhl, A Kemp, P Audebert, M Roth, R Stephens, I Barton, A Blazevic, E Brambrink, et al. Ultralow emittance, multi-mev proton beams from a laser virtual-cathode plasma accelerator. *Physical review letters*, 92(20):204801, 2004. DOI: 10.1103/PhysRevLett.92.204801.

[25] Brendan Dromey, M Coughlan, Lovisa Senje, Mark Taylor, S Kuschel, B Villagomez-Bernabe, R Stefanuik, G Nersisyan, L Stella, J Kohanoff, et al. Picosecond metrology of laser-driven proton bursts. *Nature communications*, 7(1):10642, 2016. DOI: 10.1038/ncomms10642.

[26] Marco Borghesi, J Fuchs, SV Bulanov, AJ Mackinnon, PK Patel, and M Roth. Fast ion generation by high-intensity laser irradiation of solid targets and applications. *Fusion science and technology*, 49(3):412–439, 2006. DOI: 10.13182/FST06-A1159.

[27] Hiroyuki Daido, Mamiko Nishiuchi, and Alexander S Pirozhkov. Review of laser-driven ion sources and their applications. *rpp*, 75(5):056401, 2012. DOI: 10.1088/0034-4885/75/5/056401.

[28] Andrea Macchi, Marco Borghesi, and Matteo Passoni. Ion acceleration by superintense laser-plasma interaction. *Reviews of Modern Physics*, 85(2):751, 2013. DOI: 10.1103/RevModPhys.85.751.

[29] Jörg Schreiber, PR Bolton, and K Parodi. Invited review article:"hands-on" laser-driven ion acceleration: A primer for laser-driven source development and potential applications. *Review of Scientific Instruments*, 87(7), 2016. DOI: 10.1063/1.4959198.

[30] M Roth, D Jung, K Falk, N Guler, O Deppert, M Devlin, A Favalli, J Fernandez, D Gautier, M Geissel, et al. Bright laser-driven neutron source based on the relativistic transparency of solids. *Physical review letters*, 110(4):044802, 2013. DOI: 10.1103/PhysRevLett.110.044802.

[31] YL Yao, SK He, Z Lei, T Ye, Y Xie, ZG Deng, B Cui, W Qi, L Yang, SP Zhu, et al. High-flux neutron generator based on laser-driven collisionless shock acceleration. *Physical Review Letters*, 131(2):025101, 2023. DOI: 10.1103/PhysRevLett.131.025101.

[32] Paul K Chu, JY Chen, LP Wang, and Nan Huang. Plasma-surface modification of biomaterials. *Materials Science and Engineering: R: Reports*, 36(5-6):143–206, 2002. DOI: 10.1016/S0927-796X(02)00004-9.

[33] M Barberio, M Scisciò, S Vallières, F Cardelli, SN Chen, G Famulari, T Gangolf, G Revet, A Schiavi, M Senzacqua, et al. Laser-accelerated particle beams for stress testing of materials. *Nature communications*, 9(1):372, 2018. DOI: 10.1038/s41467-017-02675-x.

[34] Walid Redjem, Ariel J Amsellem, Frances I Allen, Gabriele Benndorf, Jianhui Bin, Stepan Bulanov, Eric Esarey, Leonard C Feldman, Javier Ferrer Fernandez, Javier Garcia Lopez, et al. Defect engineering of silicon with ion pulses from laser acceleration. *Communications Materials*, 4(1):22, 2023. DOI: 10.1038/s43246-023-00349-4.

[35] M Roth, TE Cowan, MH Key, SP Hatchett, C Brown, W Fountain, J Johnson, DM Pennington, RA Snavely, SC Wilks, et al. Fast ignition by intense

laser-accelerated proton beams. *Physical review letters*, 86(3):436, 2001. DOI: 10.1103/PhysRevLett.86.436.

[36] OA Hurricane, PK Patel, R Betti, DH Froula, SP Regan, SA Slutz, MR Gomez, and MA Sweeney. Physics principles of inertial confinement fusion and us program overview. *Reviews of Modern Physics*, 95(2):025005, 2023. DOI: 10.1103/RevModPhys.95.025005.

[37] TM Ostermayr, C Kreuzer, FS Englbrecht, J Gebhard, J Hartmann, A Huebl, D Haffa, P Hilz, K Parodi, J Wenz, et al. Laser-driven x-ray and proton microsource and application to simultaneous single-shot bi-modal radiographic imaging. *Nature communications*, 11(1):6174, 2020. DOI: 10.1038/s41467-020-19838-y.

[38] A Prasselsperger, M Coughlan, N Breslin, M Yeung, C Arthur, H Donnelly, S White, M Afshari, M Speicher, R Yang, et al. Real-time electron solvation induced by bursts of laser-accelerated protons in liquid water. *Physical Review Letters*, 127(18):186001, 2021. DOI: 10.1103/PhysRevLett.127.186001.

[39] Marie-Catherine Vozenin, Jean Bourhis, and Marco Durante. Towards clinical translation of flash radiotherapy. *Nature Reviews Clinical Oncology*, 19(12):791–803, 2022. DOI: 10.1038/s41571-022-00697-z.

[40] Florian Kroll, Florian-Emanuel Brack, Constantin Bernert, Stefan Bock, Elisabeth Bodenstein, Kerstin Brüchner, Thomas E Cowan, Lennart Gaus, René Gebhardt, Uwe Helbig, et al. Tumour irradiation in mice with a laser-accelerated proton beam. *Nature Physics*, 18(3):316–322, 2022. DOI: 10.1038/s41567-022-01520-3.

[41] Jianhui Bin, Lieselotte Obst-Huebl, Jian-Hua Mao, Kei Nakamura, Laura D Geulig, Hang Chang, Qing Ji, Li He, Jared De Chant, Zachary Kober, et al. A new platform for ultra-high dose rate radiobiological research using the bella pw laser proton beamline. *Scientific reports*, 12(1):1484, 2022. DOI: 10.1038/s41598-022-05181-3.

[42] YF Li, XF Shen, YL Yao, SZ Wu, A Pukhov, and B Qiao. Laser-driven time-limited light-sail acceleration of protons for tumor radiotherapy. *Physical Review Research*, 5(1):L012038, 2023. DOI: 10.1103/PhysRevResearch.5.L012038.

[43] Pankaj Chaudhary, Giuliana Milluzzo, Hamad Ahmed, Boris Odlozilik, Aaron McMurray, Kevin M Prise, and Marco Borghesi. Radiobiology experiments with

ultra-high dose rate laser-driven protons: methodology and state-of-the-art. *Frontiers in Physics*, 9:624963, 2021. DOI: 10.3389/fphy.2021.624963.

[44] Alessandro Maffini, Francesco Mirani, Marta Galbiati, Kevin Ambrogioni, Francesco Gatti, Maria Sole Galli De Magistris, Davide Vavassori, Davide Orecchia, David Dellasega, Valeria Russo, et al. Towards compact laser-driven accelerators: exploring the potential of advanced double-layer targets. *EPJ Techniques and Instrumentation*, 10(1):15, 2023. DOI: 10.1140/epjti/s40485-023-00102-8.

[45] V Ospina-Bohórquez, C Salgado-López, M Ehret, S Malko, M Salvadori, T Pisarczyk, T Chodukowski, Z Rusiniak, M Krupka, P Guillon, et al. Laser-driven ion and electron acceleration from near-critical density gas targets: Towards high-repetition rate operation in the 1 pw, sub-100 fs laser interaction regime. *Physical Review Research*, 6(2):023268, 2024. DOI: 10.1103/PhysRevResearch.6.023268.

[46] Simon Vallières, Martina Salvadori, Alexander Permogorov, Giada Cantono, Kristoffer Svendsen, Z Chen, S Sun, Fabrizio Consoli, E d'Humières, C-G Wahlström, et al. Enhanced laser-driven proton acceleration using nanowire targets. *Scientific Reports*, 11(1):2226, 2021. DOI: 10.1038/s41598-020-80392-0.

[47] Florian Lindner. *Laser-driven heavy ion acceleration.* PhD thesis, Ludwig-Maximilians-Universität München, 2021.

[48] PL Poole, CD Andereck, DW Schumacher, RL Daskalova, S Feister, KM George, C Willis, KU Akli, and EA Chowdhury. Liquid crystal films as on-demand, variable thickness (50–5000 nm) targets for intense lasers. *Physics of Plasmas*, 21(6), 2014. DOI: 10.1063/1.4885100.

[49] Ying Gao, Jianhui Bin, Daniel Haffa, Christian Kreuzer, Jens Hartmann, Martin Speicher, Florian H Lindner, Tobias M Ostermayr, Peter Hilz, Thomas F Rösch, et al. An automated, 0.5 hz nano-foil target positioning system for intense laser plasma experiments. *High Power Laser Science and Engineering*, 5:e12, 2017. DOI: 10.1017/hpl.2017.10.

[50] P McKenna, KWD Ledingham, I Spencer, T McCany, RP Singhal, C Ziener, PS Foster, EJ Divall, CJ Hooker, D Neely, et al. Characterization of multiterawatt laser-solid interactions for proton acceleration. *Review of scientific instruments*, 73(12):4176–4184, 2002. DOI: 10.1063/1.1516855.

[51] Lieselotte Obst, Sebastian Göde, Martin Rehwald, Florian-Emanuel Brack, João Branco, Stefan Bock, Michael Bussmann, Thomas E Cowan, Chandra B Curry, Frederico Fiuza, et al. Efficient laser-driven proton acceleration from cylindrical and planar cryogenic hydrogen jets. *Scientific reports*, 7(1):10248, 2017. DOI: 10.1038/s41598-017-10589-3.

[52] M Gauthier, CB Curry, Sebastian Göde, F-E Brack, JB Kim, MJ MacDonald, J Metzkes, L Obst, M Rehwald, C Rödel, et al. High repetition rate, multi-mev proton source from cryogenic hydrogen jets. *Applied Physics Letters*, 111(11), 2017. DOI: 10.1063/1.4990487.

[53] Andreas Thoss, M Richardson, G Korn, M Faubel, H Stiel, Ulrich Vogt, and Thomas Elsaesser. Kilohertz sources of hard x rays and fast ions with femtosecond laser plasmas. *JOSA B*, 20(1):224–228, 2003. DOI: 10.1364/JOSAB.20.000224.

[54] Maria Ekimova, Wilson Quevedo, Manfred Faubel, Philippe Wernet, and Erik TJ Nibbering. A liquid flatjet system for solution phase soft-x-ray spectroscopy. *Structural Dynamics*, 2(5), 2015. DOI: 10.1063/1.4928715.

[55] John T Morrison, Scott Feister, Kyle D Frische, Drake R Austin, Gregory K Ngirmang, Neil R Murphy, Chris Orban, Enam A Chowdhury, and WM Roquemore. Mev proton acceleration at khz repetition rate from ultra-intense laser liquid interaction. *New Journal of Physics*, 20(2):022001, 2018. DOI: 10.1088/1367-2630/aaa8d1.

[56] P Puyuelo-Valdes, D de Luis, J Hernandez, JI Apiñaniz, A Curcio, JL Henares, M Huault, JA Pérez-Hernández, L Roso, G Gatti, et al. Implementation of a thin, flat water target capable of high-repetition-rate mev-range proton acceleration in a high-power laser at the clpu. *Plasma Physics and Controlled Fusion*, 64(5):054003, 2022. DOI: 10.1088/1361-6587/ac5643.

[57] F Treffert, CB Curry, H-GJ Chou, CJ Crissman, DP DePonte, F Fiuza, GD Glenn, RC Hollinger, R Nedbailo, J Park, et al. High-repetition-rate, multi-mev deuteron acceleration from converging heavy water microjets at laser intensities of 10^21 w/cm^2. *Applied Physics Letters*, 121(7), 2022. DOI: 10.1063/5.0098973.

[58] Yang Hwan Kim, Hyeon Kim, Seong Cheol Park, Yongjin Kwon, Kyunghoon Yeom, Wosik Cho, Taeyong Kwon, Hyeok Yun, Jae Hee Sung, Seong Ku Lee,

et al. High-harmonic generation from a flat liquid-sheet plasma mirror. *Nature communications*, 14(1):2328, 2023. DOI: 10.1038/s41467-023-38087-3.

[59] Zhengxuan Cao, Ziyang Peng, Yinren Shou, Jiarui Zhao, Shiyou Chen, Ying Gao, Jianbo Liu, Pengjie Wang, Zhusong Mei, Zhuo Pan, et al. Vibration and jitter of free-flowing thin liquid sheets as target for high-repetition-rate laser-ion acceleration. *Frontiers in Physics*, 11:1172075, 2023. DOI: 10.3389/fphy.2023.1172075.

[60] K Osvay, L Stuhl, P Varmazyar, T Gilinger, Z Elekes, A Fenyvesi, K Hideghethy, RE Szabo, M Füle, B Biró, et al. Towards a 10^10 n/s neutron source with khz repetition rate, few-cycle laser pulses. *The European Physical Journal Plus*, 139(7):574, 2024. DOI: 10.1140/epjp/s13360-024-05338-1.

[61] I Prencipe, J Fuchs, S Pascarelli, DW Schumacher, RB Stephens, NB Alexander, R Briggs, M Büscher, MO Cernaianu, A Choukourov, et al. Targets for high repetition rate laser facilities: needs, challenges and perspectives. *High Power Laser Science and Engineering*, 5:e17, 2017. DOI: 10.1017/hpl.2017.18.

[62] Muhammad Noaman-ul Haq, Hamad Ahmed, Thomas Sokollik, Lule Yu, Zezhou Liu, Xiaohui Yuan, Fang Yuan, Mohammad Mirzaie, Xulei Ge, Liming Chen, et al. Statistical analysis of laser driven protons using a high-repetition-rate tape drive target system. *Physical Review Accelerators and Beams*, 20(4):041301, 2017. DOI: 10.1103/PhysRevAccelBeams.20.041301.

[63] S Ter-Avetisyan, B Ramakrishna, R Prasad, M Borghesi, PV Nickles, S Steinke, M Schnürer, KI Popov, L Ramunno, NV Zmitrenko, et al. Generation of a quasi-monoergetic proton beam from laser-irradiated sub-micron droplets. *Physics of Plasmas*, 19(7), 2012. DOI: 10.1063/1.4731712.

[64] Paul Gibbon. *Short Pulse Laser Interactions with Matter: An Introduction*. World Scientific, 2005. DOI: 10.1142/p116.

[65] Andrea Macchi. *A Superintense Laser-Plasma Interaction Theory Primer*. Springer Science & Business Media, 2013. DOI: 10.1007/978-94-007-6125-4.

[66] William Kruer. *The Physics Of Laser Plasma Interactions*. crc Press, 1 edition, 2003. First Edition. DOI: 10.1080/09500348914550481.

[67] John David Jackson. *Classical Electrodynamics*. Wiley, New York, 3 edition, 1999. Third Edition. Link: john-david-jackson-classical-electrodynamics-wiley-1999.

[68] Jens Hartmann, Daniel Haffa, Martin Speicher, Jianhui Bin, Peter Hilz, Christian Kreuzer, Tobias Ostermayr, Sebastian Lehrack, and Jörg Schreiber. The spatial contrast challenge for intense laser-plasma experiments. In *Journal of Physics: Conference Series*, volume 1079, page 012003. IOP Publishing, 2018. DOI: 10.1088/1742-6596/1079/1/012003.

[69] John David Lawson. Lasers and accelerators. *IEEE Transactions on Nuclear Science*, 26(3):4217–4219, 1979. DOI: 10.1109/TNS.1979.4330749.

[70] PM Woodward. A method of calculating the field over a plane aperture required to produce a given polar diagram. *Journal of the Institution of Electrical Engineers-Part IIIA: Radiolocation*, 93(10):1554–1558, 1946. DOI: 10.1049/ji-3a-1.1946.0262.

[71] Martin Speicher. *Optical probing of laser-induced expansion of levitating microspheres*. PhD thesis, Ludwig-Maximilians-Universität München, 2022.

[72] Albert Gold and H Barry Bebb. Theory of multiphoton ionization. *Physical Review Letters*, 14(3):60, 1965. DOI: 10.1103/PhysRevLett.14.60.

[73] Charles K Rhodes. Multiphoton ionization of atoms. *Science*, 229(4720):1345–1351, 1985. DOI: 10.1126/science.229.4720.1345.

[74] G Mainfray and G Manus. Multiphoton ionization of atoms. *Reports on progress in physics*, 54(10):1333, 1991. DOI: 10.1088/0034-4885/54/10/002.

[75] Paul B Corkum. Plasma perspective on strong field multiphoton ionization. *Physical review letters*, 71(13):1994, 1993. DOI: 10.1103/PhysRevLett.71.1994.

[76] M Protopapas, Christoph H Keitel, and Peter L Knight. Atomic physics with super-high intensity lasers. *Reports on Progress in Physics*, 60(4):389, 1997. DOI: 10.1088/0034-4885/60/4/001.

[77] Joseph H Eberly, Juka Javanainen, and Kazimierz Rzazewski. Above-threshold ionization. *Physics reports*, 204(5):331–383, 1991. DOI: 10.1016/0370-1573(91)90131-5.

[78] Pierre Agostini, F Fabre, Gérard Mainfray, Guillaume Petite, and N Ko Rahman. Free-free transitions following six-photon ionization of xenon atoms. *Physical Review Letters*, 42(17):1127, 1979. DOI: 10.1103/PhysRevLett.42.1127.

[79] L. V. Keldysh. Ionization in the field of a strong electromagnetic wave. *Soviet Physics JETP*, 20(5):1307–1314, 1965.

[80] Eric Mevel, Pierre Breger, Rusty Trainham, Guillaume Petite, Pierre Agostini, Arnold Migus, Jean-Paul Chambaret, and Andre Antonetti. Atoms in strong optical fields: evolution from multiphoton to tunnel ionization. *Physical review letters*, 70(4):406, 1993. DOI: 10.1103/PhysRevLett.70.406.

[81] AM Perelomov, VS Popov, and MV Terent'Ev. Ionization of atoms in an alternating electric field. *Sov. Phys. JETP*, 23(5):924–934, 1966.

[82] Maxim V Ammosov, Nikolai B Delone, and Vladimir P Krainov. Tunnel ionization of complex atoms and of atomic ions in an alternating electromagnetic field. *Soviet Journal of Experimental and Theoretical Physics*, 64(6):1191, 1986.

[83] AM Zheltikov. Keldysh parameter, photoionization adiabaticity, and the tunneling time. *Physical Review A*, 94(4):043412, 2016. DOI: 10.1103/PhysRevA.94.043412.

[84] AI Baz. Lifetime of intermediate states. *Yadern. Fiz.*, 4, 1966. Link: biblio/4514306.

[85] VF Rybachenko. Time of particle penetrating through barrier. *Yadern. Fiz., 5: 895-901 (Apr. 1967).*, 1967. Link: biblio/4390649.

[86] M Büttiker and R Landauer. Traversal time for tunneling. *Physical Review Letters*, 49(23):1739, 1982. DOI: 10.1103/PhysRevLett.49.1739.

[87] Eugene P Wigner. Lower limit for the energy derivative of the scattering phase shift. *Physical Review*, 98(1):145, 1955. DOI: 10.1103/PhysRev.98.145.

[88] Eli Pollak and William H Miller. New physical interpretation for time in scattering theory. *Physical review letters*, 53(2):115, 1984. DOI: 10.1103/PhysRevLett.53.115.

[89] Steeve Augst, Donna Strickland, David D Meyerhofer, See-Leang Chin, and Joseph H Eberly. Tunneling ionization of noble gases in a high-intensity laser field. *Physical review letters*, 63(20):2212, 1989. DOI: 10.1103/PhysRevLett.63.2212.

[90] Wolfgang Lotz. An empirical formula for the electron-impact ionization cross-section. *Zeitschrift für Physik*, 206(2):205–211, 1967. DOI: 10.1007/BF01325928.

[91] Wolfgang Lotz. Electron-impact ionization cross-sections and ionization rate coefficients for atoms and ions from hydrogen to calcium. *Zeitschrift für Physik*, 216(3):241–247, 1968. DOI: 10.1007/BF01392963.

[92] T Ditmire, T Donnelly, AM Rubenchik, RW Falcone, and MD Perry. Interaction of intense laser pulses with atomic clusters. *Physical Review A*, 53(5):3379, 1996. DOI: 10.1103/PhysRevA.53.3379.

[93] T Ditmire, T Donnelly, RW Falcone, and MD Perry. Strong x-ray emission from high-temperature plasmas produced by intense irradiation of clusters. *Physical review letters*, 75(17):3122, 1995. DOI: 10.1103/PhysRevLett.75.3122.

[94] Francis F Chen et al. *Introduction to plasma physics and controlled fusion*, volume 1. Springer, 1984. DOI: 10.1007/978-3-319-22309-4.

[95] José A Bittencourt. *Fundamentals of plasma physics*. Springer Science & Business Media, 2013. DOI: 10.1007/978-1-4757-4030-1.

[96] Scott C Wilks and William L Kruer. Absorption of ultrashort, ultra-intense laser light by solids and overdense plasmas. *IEEE Journal of Quantum Electronics*, 33(11):1954–1968, 1997. DOI: 10.1109/3.641310.

[97] Peter Mulser and Dieter Bauer. *High power laser-matter interaction*, volume 238. Springer Science & Business Media, 2010. DOI: 10.1007/978-3-540-46065-7.

[98] F Brunel. Not-so-resonant, resonant absorption. *Physical review letters*, 59(1):52, 1987. DOI: 10.1103/PhysRevLett.59.52.

[99] K Krushelnick, EL Clark, Z Najmudin, Marco Salvati, MIK Santala, M Tatarakis, AE Dangor, Victor Malka, D Neely, R Allott, et al. Multi-mev ion production from high-intensity laser interactions with underdense plasmas. *Physical review letters*, 83(4):737, 1999. DOI: 10.1103/PhysRevLett.83.737.

[100] DW Forslund and CR Shonk. Formation and structure of electrostatic collisionless shocks. *Physical Review Letters*, 25(25):1699, 1970. DOI: 10.1103/PhysRevLett.25.1699.

[101] DW Forslund and JP Freidberg. Theory of laminar collisionless shocks. *Physical Review Letters*, 27(18):1189, 1971. DOI: 10.1103/PhysRevLett.27.1189.

[102] Luís O Silva, Michael Marti, Jonathan R Davies, Ricardo A Fonseca, Chuang Ren, Frank S Tsung, and Warren B Mori. Proton shock acceleration in laser-plasma interactions. *Physical Review Letters*, 92(1):015002, 2004. DOI: 10.1103/PhysRevLett.92.015002.

[103] SV Bulanov, DV Dylov, T Zh Esirkepov, FF Kamenets, and DV Sokolov. Ion acceleration in a dipole vortex in a laser plasma corona. *Plasma physics reports*, 31:369–381, 2005. DOI: 10.1134/1.1925787.

[104] SV Bulanov and T Zh Esirkepov. Comment on "collimated multi-mev ion beams from high-intensity laser interactions with underdense plasma". *Physical review letters*, 98(4):049503, 2007. DOI: 10.1103/PhysRevLett.98.049503.

[105] Tatsufumi Nakamura, Sergei V Bulanov, Timur Zh Esirkepov, and Masaki Kando. High-energy ions from near-critical density plasmas via magnetic vortex acceleration. *Physical review letters*, 105(13):135002, 2010. DOI: 10.1103/PhysRevLett.105.135002.

[106] Lin Yin, BJ Albright, BM Hegelich, and JC Fernández. Gev laser ion acceleration from ultrathin targets: The laser break-out afterburner. *Laser and Particle Beams*, 24(2):291–298, 2006. DOI: 10.1017/S0263034606060459.

[107] L Yin, BJ Albright, BM Hegelich, Kevin J Bowers, KA Flippo, TJT Kwan, and JC Fernández. Monoenergetic and gev ion acceleration from the laser breakout afterburner using ultrathin targets. *Physics of plasmas*, 14(5), 2007. DOI: 10.1063/1.2436857.

[108] BJ Albright, L Yin, Kevin J Bowers, BM Hegelich, KA Flippo, TJT Kwan, and JC Fernandez. Relativistic buneman instability in the laser breakout afterburner. *Physics of Plasmas*, 14(9), 2007. DOI: 10.1063/1.2768933.

[109] L Yin, BJ Albright, KJ Bowers, D Jung, JC Fernández, and BM Hegelich. Three-dimensional dynamics of breakout afterburner ion acceleration<? format?> using high-contrast short-pulse laser and nanoscale targets. *Physical review letters*, 107(4):045003, 2011. DOI: 10.1103/PhysRevLett.107.045003.

[110] Erik Lefebvre and Guy Bonnaud. Transparency/opacity of a solid target illuminated by an ultrahigh-intensity laser pulse. *Physical review letters*, 74(11):2002, 1995. DOI: 10.1103/PhysRevLett.74.2002.

[111] S Guerin, P Mora, JC Adam, A Héron, and G Laval. Propagation of ultraintense laser pulses through overdense plasma layers. *Physics of Plasmas*, 3(7):2693–2701, 1996. DOI: 10.1063/1.871526.

[112] M Tushentsov, A Kim, F Cattani, D Anderson, and M Lisak. Electromagnetic energy penetration in the self-induced transparency regime of relativistic laser-plasma interactions. *Physical review letters*, 87(27):275002, 2001. DOI: 10.1103/PhysRevLett.87.275002.

[113] Andreas Henig, Daniel Kiefer, K Markey, DC Gautier, KA Flippo, S Letzring, RP Johnson, T Shimada, L Yin, BJ Albright, et al. Enhanced laser-driven ion acceleration in the relativistic transparency regime. *Physical review letters*, 103(4):045002, 2009. DOI: 10.1103/PhysRevLett.103.045002.

[114] Stephen P Hatchett, Curtis G Brown, Thomas E Cowan, Eugene A Henry, Joy S Johnson, Michael H Key, Jeffrey A Koch, A Bruce Langdon, Barbara F Lasinski, Richard W Lee, et al. Electron, photon, and ion beams from the relativistic interaction of petawatt laser pulses with solid targets. *Physics of Plasmas*, 7(5):2076–2082, 2000. DOI: 10.1063/1.874030.

[115] SC Wilks, AB Langdon, TE Cowan, M Roth, M Singh, S Hatchett, MH Key, D Pennington, A MacKinnon, and RA Snavely. Energetic proton generation in ultra-intense laser–solid interactions. *Physics of plasmas*, 8(2):542–549, 2001. DOI: 10.1063/1.1333697.

[116] Patrick Mora. Plasma expansion into a vacuum. *Physical Review Letters*, 90(18):185002, 2003. DOI: 10.1103/PhysRevLett.90.185002.

[117] Jörg Schreiber, F Bell, F Grüner, U Schramm, Michael Geissler, M Schnürer, S Ter-Avetisyan, Björn Manuel Hegelich, J Cobble, E Brambrink, et al. Analytical model for ion acceleration by high-intensity laser pulses. *Physical review letters*, 97(4):045005, 2006. DOI: 10.1103/PhysRevLett.97.045005.

[118] T Esirkepov, Marco Borghesi, SV Bulanov, G Mourou, and T Tajima. Highly efficient relativistic-ion generation in the laser-piston regime. *Physical review letters*, 92(17):175003, 2004. DOI: 10.1103/PhysRevLett.92.175003.

[119] George Marx. Interstellar vehicle propelled by terrestrial laser beam. *Nature*, 211(5044):22–23, 1966. DOI: 10.1038/211022a0.

[120] Andrea Macchi, Federica Cattani, Tatiana V Liseykina, and Fulvio Cornolti. Laser acceleration of ion bunches at the front surface of overdense plasmas. *Physical review letters*, 94(16):165003, 2005. DOI: 10.1103/PhysRevLett.94.165003.

[121] SC Wilks, WL Kruer, M Tabak, and AB Langdon. Absorption of ultra-intense laser pulses. *Physical review letters*, 69(9):1383, 1992. DOI: 10.1103/PhysRevLett.69.1383.

[122] Andrea Macchi, Silvia Veghini, and Francesco Pegoraro. "light sail" acceleration reexamined. *Physical review letters*, 103(8):085003, 2009. DOI: 10.1103/PhysRevLett.103.085003.

[123] Bin Qiao, Matthew Zepf, Marco Borghesi, Brendan Dromey, Michael Geissler, A Karmakar, and Paul Gibbon. Radiation-pressure acceleration of ion beams from nanofoil targets: The leaky light-sail regime. *Physical review letters*, 105(15):155002, 2010. DOI: 10.1103/PhysRevLett.105.155002.

[124] Bin Qiao, Matthew Zepf, Marco Borghesi, and Michael Geissler. Stable gev ion-beam acceleration from thin foils by circularly polarized laser pulses. *Physical review letters*, 102(14):145002, 2009. DOI: 10.1103/PhysRevLett.102.145002.

[125] APL Robinson, Paul Gibbon, M Zepf, S Kar, RG Evans, and C Bellei. Relativistically correct hole-boring and ion acceleration by circularly polarized laser pulses. *Plasma Physics and Controlled Fusion*, 51(2):024004, 2009. DOI: 10.1088/0741-3335/51/2/024004.

[126] O Klimo, J Psikal, J Limpouch, and VT Tikhonchuk. Monoenergetic ion beams from ultrathin foils irradiated by ultrahigh-contrast circularly polarized laser pulses. *Physical Review Special Topics—Accelerators and Beams*, 11(3):031301, 2008. DOI: 10.1103/PhysRevSTAB.11.031301.

[127] SV Bulanov, T Zh Esirkepov, J Koga, and T Tajima. Interaction of electromagnetic waves with plasma in the radiation-dominated regime. *Plasma Physics Reports*, 30:196–213, 2004. DOI: 10.1134/1.1687021.

[128] Charlotte AJ Palmer, NP Dover, I Pogorelsky, M Babzien, GI Dudnikova, M Ispiriyan, MN Polyanskiy, Jörg Schreiber, P Shkolnikov, V Yakimenko, et al. Monoenergetic proton beams accelerated by a radiation pressure driven shock. *Physical review letters*, 106(1):014801, 2011. DOI: 10.1103/PhysRevLett.106.014801.

[129] Andreas Henig, S Steinke, M Schnürer, T Sokollik, Rainer Hörlein, D Kiefer, D Jung, Jörg Schreiber, BM Hegelich, XQ Yan, et al. Radiation-pressure acceleration of

ion beams driven by circularly polarized laser pulses. *Physical Review Letters*, 103(24):245003, 2009. DOI: 10.1103/PhysRevLett.103.245003.

[130] C Scullion, D Doria, L Romagnani, A Sgattoni, K Naughton, DR Symes, P McKenna, A Macchi, M Zepf, S Kar, et al. Polarization dependence of bulk ion acceleration from ultrathin foils irradiated by high-intensity ultrashort laser pulses. *Physical review letters*, 119(5):054801, 2017. DOI: 10.1103/PhysRevLett.119.054801.

[131] S Kar, KF Kakolee, B Qiao, A Macchi, M Cerchez, D Doria, M Geissler, P McKenna, D Neely, J Osterholz, et al. Ion acceleration in multispecies targets driven by intense laser radiation pressure. *Physical Review Letters*, 109(18):185006, 2012. DOI: 10.1103/PhysRevLett.109.185006.

[132] Norman Dombrowski and Reginald Percy Fraser. A photographic investigation into the disintegration of liquid sheets. *Philosophical Transactions of the Royal Society of London. Series A, Mathematical and Physical Sciences*, 247(924):101–130, 1954. DOI: 10.1098/rsta.1954.0014.

[133] JD Naber and Rolf D Reitz. Modeling engine spray/wall impingement. *SAE transactions*, pages 118–140, 1988. DOI: stable/44547362.

[134] Akira Watanabe, Hiroshi Saito, Yuzo Ishida, Masafumi Nakamoto, and Tatsuo Yajima. A new nozzle producing ultrathin liquid sheets for femtosecond pulse dye lasers. *Optics Communications*, 71(5):301–304, 1989. DOI: 10.1016/0030-4018(89)90012-6.

[135] Christophe Clanet. Waterbells and liquid sheets. *Annu. Rev. Fluid Mech.*, 39(1):469–496, 2007. DOI: 10.1146/annurev.fluid.39.050905.110317.

[136] Nicolas Bremond and Emmanuel Villermaux. Atomization by jet impact. *Journal of Fluid Mechanics*, 549:273–306, 2006. DOI: 10.1017/S0022112005007962.

[137] Geoffrey Taylor. Formation of thin flat sheets of water. *Proceedings of the Royal Society of London. Series A. Mathematical and Physical Sciences*, 259(1296):1–17, 1961. DOI: 10.1098/rspa.1960.0207.

[138] Jonathan Charles Tobit Barnard. *X-ray generation from, and spectroscopy of, a thin liquid sheet*. PhD thesis, Imperial College London, 2021.

[139] A Kebriaee, A Abdehkakha, H Dolatkhahi, and S Kashanj. The liquid sheet shape and thickness predictions in two impinging jets based on minimum energy principle. *arXiv preprint arXiv:2108.09852*, 2021. DOI: 10.48550/arXiv.2108.09852.

[140] Y-B Shen and D Poulikakos. Thickness variation of a liquid sheet formed by two impinging jets using holographic interferometry. *Journal of Fluids Engineering*, 1998. DOI: 10.1115/1.2820688.

[141] N Dombrowski Dombrowski and PC Hooper. A study of the sprays formed by impinging jets in laminar and turbulent flow. *Journal of fluid mechanics*, 18(3):392–400, 1964. DOI: 10.1017/S0022112064000295.

[142] Xiaodong Chen, Dongjun Ma, Vigor Yang, and Stephane Popinet. High-fidelity simulations of impinging jet atomization. *Atomization and sprays*, 23(12), 2013. DOI: 10.1615/AtomizSpr.2013007619.

[143] Xiaodong Chen and Vigor Yang. Thickness-based adaptive mesh refinement methods for multi-phase flow simulations with thin regions. *Journal of Computational Physics*, 269:22–39, 2014. DOI: 10.1016/j.jcp.2014.02.035.

[144] WE Ranz. Some experiments on the dynamics of liquid films. *Journal of Applied Physics*, 30(12):1950–1955, 1959. DOI: 10.1063/1.1735095.

[145] K Dexter Miller. Distribution of spray from impinging liquid jets. *Journal of Applied Physics*, 31(6):1132–1133, 1960. DOI: 10.1063/1.1735772.

[146] David Hasson and Ralph E Peck. Thickness distribution in a sheet formed by impinging jets. *AIChE Journal*, 10(5):752–754, 1964. DOI: 10.1002/aic.690100533.

[147] EA Ibrahim and AJ Przekwas. Impinging jets atomization. *Physics of Fluids A: Fluid Dynamics*, 3(12):2981–2987, 1991. DOI: 10.1063/1.857840.

[148] John WM Bush and Alexander E Hasha. On the collision of laminar jets: fluid chains and fishbones. *Journal of fluid mechanics*, 511:285–310, 2004. DOI: 10.1017/S002211200400967X.

[149] Li-jun Yang, Fei Zhao, Qing-fei Fu, and Kun-da Cui. Liquid sheet formed by impingement of two viscous jets. *Journal of Propulsion and Power*, 30(4):1016–1026, 2014. DOI: 10.2514/1.B35105.

[150] Sina Kashanj and Azadeh Kebriaee. Liquid sheet of two impinging jets, 2020. Link: https://gfm.aps.org/meetings/dfd-2020/5f5c0684199e4c091e67bc8c, accessed: 2024-08-02. Licensed under Creative Commons Attribution-NonCommercial 4.0 International License.

[151] Marcus F Heidmann, Richard J Priem, and Jack C Humphrey. A study of sprays formed by two impinging jets. Technical report, NACA, Washington, DC, USA, 1957. Link: 19930084568/downloads/19930084568.pdf.

[152] Norman Dombrowski and WR Johns. The aerodynamic instability and disintegration of viscous liquid sheets. *Chemical Engineering Science*, 18(3):203–214, 1963. DOI: 10.1016/0009-2509(63)85005-8.

[153] Ri Li and Nasser Ashgriz. Characteristics of liquid sheets formed by two impinging jets. *Physics of fluids*, 18(8), 2006. DOI: 10.1063/1.2338064.

[154] Joseph Snyder, John Morrison, Scott Feister, Kyle Frische, Kevin George, Manh Le, Christopher Orban, Gregory Ngirmang, Enam Chowdhury, and William Roquemore. Background pressure effects on mev protons accelerated via relativistically intense laser-plasma interactions. *Scientific Reports*, 10(1):18245, 2020. DOI: 0.1038/s41598-020-75061-1.

[155] Jan Hendrik DEBOER. *The dynamical character of adsorption*, volume 76(2). Wolters Kluwer Health, Inc., 1953.

[156] Frank E Jones. *Evaporation of water with emphasis on applications and measurements*. CRC Press, 2018. DOI: 10.1201/9781351071963.

[157] Gediminas Galinis, Jergus Strucka, Jonathan CT Barnard, Avi Braun, Roland A Smith, and Jon P Marangos. Micrometer-thickness liquid sheet jets flowing in vacuum. *Review of Scientific Instruments*, 88(8), 2017. DOI: 10.1063/1.4990130.

[158] Jake D Koralek, Jongjin B Kim, Petr Bruža, Chandra B Curry, Zhijiang Chen, Hans A Bechtel, Amy A Cordones, Philipp Sperling, Sven Toleikis, Jan F Kern, et al. Generation and characterization of ultrathin free-flowing liquid sheets. *Nature communications*, 9(1):1353, 2018. DOI: 10.1038/s41467-018-03696-w.

[159] Byunghang Ha, Daniel P DePonte, and Juan G Santiago. Device design and flow scaling for liquid sheet jets. *Physical Review Fluids*, 3(11):114202, 2018. DOI: 10.1103/PhysRevFluids.3.114202.

[160] Christopher J Crissman, Mianzhen Mo, Zhijiang Chen, Jie Yang, Diego A Huyke, Siegfried H Glenzer, Kathryn Ledbetter, J Pedro F Nunes, May Ling Ng, Hengzi Wang, et al. Sub-micron thick liquid sheets produced by isotropically etched glass nozzles. *Lab on a Chip*, 22(7):1365–1373, 2022. DOI: 10.1039/D1LC00757B.

[161] Y-J Choo and B-S Kang. The velocity distribution of the liquid sheet formed by two low-speed impinging jets. *Physics of fluids*, 14(2):622–627, 2002. DOI: 10.1063/1.1429250.

[162] David J Hoffman, Tim B Van Driel, Thomas Kroll, Christopher J Crissman, Elizabeth S Ryland, Kacie J Nelson, Amy A Cordones, Jake D Koralek, and Daniel P DePonte. Microfluidic liquid sheets as large-area targets for high repetition xfels. *Frontiers in molecular biosciences*, 9:1048932, 2022. DOI: 10.3389/fmolb.2022.1048932.

[163] KM George, JT Morrison, S Feister, GK Ngirmang, JR Smith, AJ Klim, J Snyder, D Austin, W Erbsen, KD Frische, et al. High-repetition-rate (khz) targets and optics from liquid microjets for high-intensity laser–plasma interactions. *High Power Laser Science and Engineering*, 7:e50, 2019. DOI: 10.1017/hpl.2019.35.

[164] Masato Kondoh and Masaaki Tsubouchi. Liquid-sheet jets for terahertz spectroscopy. *Optics express*, 22(12):14135–14147, 2014. DOI: 10.1364/OE.22.014135.

[165] M Füle, AP Kovács, T Gilinger, M Karnok, P Gaál, S Figul, G Marowsky, and K Osvay. Development of an ultrathin liquid sheet target for laser ion acceleration at high repetition rates in the kilohertz range. *High Power Laser Science and Engineering*, 12:e37, 2024. DOI: 10.1017/hpl.2024.19.

[166] University of Texas at Austin. Phase diagram of water. Link: https://ch302.cm.utexas.edu/physEQ/physical/selector.php?name=phase-diag, accessed: 2024-08-06.

[167] M Faubel, S Schlemmer, and JP Toennies. A molecular beam study of the evaporation of water from a liquid jet. *Zeitschrift für Physik D Atoms, Molecules and Clusters*, 10:269–277, 1988. DOI: 10.1007/BF01384861.

[168] DP DePonte, Uwe Weierstall, Kevin Schmidt, J Warner, DHSJC Starodub, JCH Spence, and RB Doak. Gas dynamic virtual nozzle for generation of microscopic droplet streams. *Journal of Physics D: Applied Physics*, 41(19):195505, 2008. DOI: 10.1088/0022-3727/41/19/195505.

[169] Ludwig-Maximilians-Universität München. Atlas-3000. Link: *LMU Atlas-3000 Research Page*, accessed: 2024-08-20.

[170] Jens Osterhoff. *Stable, ultra-relativistic electron beams by laser-wakefield acceleration.* PhD thesis, Ludwig-Maximilians-Universität München, 2009.

[171] Frederic Verluise, Vincent Laude, Z Cheng, Ch Spielmann, and Pierre Tournois. Amplitude and phase control of ultrashort pulses by use of an acousto-optic programmable dispersive filter: pulse compression and shaping. *Optics letters*, 25(8):575–577, 2000. DOI: 10.1364/OL.25.000575.

[172] JE Murray and WH Lowdermilk. Nd: YAG regenerative amplifier. *Journal of Applied Physics*, 51(7):3548–3556, 1980. DOI: 10.1063/1.328194.

[173] Thomas Oksenhendler, D Kaplan, P Tournois, GM Greetham, and F Estable. Intracavity acousto-optic programmable gain control for ultra-wide-band regenerative amplifiers. *Applied Physics B*, 83:491–494, 2006. DOI: 10.1007/s00340-006-2231-0.

[174] Fastlite. Wizzler, 2024. Link: Wizzler, accessed: 2024-08-20.

[175] Swamp Optics. GRENOUILLE, 2024. Link: GRENOUILLE, accessed: 2024-08-30.

[176] Ultrafast Innovations. Tundra, 2024. Link: TUNDRA, accessed: 2024-08-30.

[177] Thomas F Rösch, Masoud Afshari, Felix Balling, Leonard Doyle, Sonja Gerlach, Jens Hartmann, Alexander Prasselsperger, Stuart Morris, and Jörg Schreiber. Transverse emittance growth of proton sources from laser-irradiated sub-μ m-thin planar targets. *Physical Review E*, 109(2):025201, 2024. DOI: 10.1103/PhysRevE.109.025201.

[178] Daniel Jung, L Yin, BJ Albright, DC Gautier, Rainer Hörlein, Daniel Kiefer, Andreas Henig, R Johnson, S Letzring, S Palaniyappan, et al. Monoenergetic ion beam generation by driving ion solitary waves with circularly polarized laser light. *Physical Review Letters*, 107(11):115002, 2011. DOI: 10.1103/PhysRevLett.107.115002.

[179] Jens Hartmann. *Quantitative Ion Spectrometry and first laser-ion acceleration results at the Centre for Advanced Laser Applications.* PhD thesis, Ludwig-Maximilians-Universität München, 2022.

[180] S Reinhardt, W Draxinger, Jörg Schreiber, and W Assmann. A pixel detector system for laser-accelerated ion detection. *Journal of Instrumentation*, 8(03):P03008, 2013. DOI: 10.1088/1748-0221/8/03/P03008.

[181] C.E. Frank. Development of an optical setup to verify the temporal beam drift of an ultrashort pulse petawatt laser system. Bachelor's thesis, Ludwig-Maximilians-Universität München, Munich, August 2021.

[182] Tango. https://www.tango-controls.org/, accessed: 2024-10-16.

[183] Nils Weiße, Leonard Doyle, Johannes Gebhard, Felix Balling, Florian Schweiger, Florian Haberstroh, Laura D Geulig, Jinpu Lin, Faran Irshad, Jannik Esslinger, et al. Tango controls and data pipeline for petawatt laser experiments. *High Power Laser Science and Engineering*, 11:e44, 2023. DOI: 10.1017/hpl.2023.17.

[184] M. Kögler. Construction of a vacuum microscope. Bachelor's thesis, Ludwig-Maximilians-Universität München, Munich, April 2014.

[185] Kreuzer Christian. *Technological Developments for Laser Ion Acceleration.* PhD thesis, Ludwig-Maximilians-Universität München, 2018.

[186] Doyle Leonard. Implementation of an adaptive optics system for focus optimization at the centre for advanced laser applications. Master's thesis, Ludwig-Maximilians-Universität München, Munich, March 2019.

[187] Thorlabs. Fbh650-10 bandpass filter. Available online at Thorlabs product page, accessed: 2024-10-21.

[188] S. Reinhardt. *Detection of laser-accelerated protons.* PhD thesis, Ludwig-Maximilians-Universität München, 2012.

[189] P.A. Kühnemann. Development of a self-calibrating energy measurement template for laser-driven protons. Bachelor's thesis, Ludwig-Maximilians-Universität München, Munich, March 2018.

[190] F Lindner. Online diagnostics for laser accelerated ions and electrons. Master's thesis, Ludwig-Maximilians-Universität München, 2015.

[191] Hans Bichsel. Straggling in thin silicon detectors. *Reviews of Modern Physics*, 60(3):663, 1988. DOI: 10.1103/RevModPhys.60.663.

[192] Lianren He et al. Variability assessment of a 300 tw laser-driven water-leaf proton source. *Physical Review X*, 2024. (*submitted*).

[193] Fabrizio Consoli, Vladimir T Tikhonchuk, Matthieu Bardon, Philip Bradford, David C Carroll, Jakub Cikhardt, Mattia Cipriani, Robert J Clarke, Thomas E Cowan, Colin N Danson, et al. Laser produced electromagnetic pulses: generation, detection and mitigation. *High Power Laser Science and Engineering*, 8:e22, 2020. DOI: 10.1017/hpl.2020.13.

[194] Pierre-Gilles Gennes, Françoise Brochard-Wyart, David Quéré, et al. *Capillarity and wetting phenomena: drops, bubbles, pearls, waves*. Springer, 2004. DOI: 10.1007/978-0-387-21656-0.

[195] Jens Eggers. Nonlinear dynamics and breakup of free-surface flows. *Reviews of modern physics*, 69(3):865, 1997. DOI: 10.1103/RevModPhys.69.865.

[196] M Zimmer, S Scheuren, T Ebert, G Schaumann, B Schmitz, J Hornung, V Bagnoud, C Rödel, and M Roth. Analysis of laser-proton acceleration experiments for development of empirical scaling laws. *Physical Review E*, 104(4):045210, 2021. DOI: 10.1103/PhysRevE.104.045210.

[197] J Schreiber, F Bell, and Z Najmudin. Optimization of relativistic laser–ion acceleration. *High Power Laser Science and Engineering*, 2:e41, 2014. DOI: 10.1017/hpl.2014.46.

[198] NP Dover, M Nishiuchi, H Sakaki, Ko Kondo, HF Lowe, MA Alkhimova, EJ Ditter, OC Ettlinger, A Ya Faenov, M Hata, et al. Demonstration of repetitive energetic proton generation by ultra-intense laser interaction with a tape target. *High Energy Density Physics*, 37:100847, 2020. DOI: 10.1016/j.hedp.2020.100847.

[199] Y Sentoku, V Yu Bychenkov, K Flippo, Anatoly Maksimchuk, K Mima, G Mourou, ZM Sheng, and Donald Umstadter. High-energy ion generation in interaction. of short laser pulse with high-density plasma. *Applied Physics B*, 74:207–215, 2002. DOI: 10.1007/s003400200796.

[200] Malte Kaluza, Jörg Schreiber, Marko IK Santala, George D Tsakiris, Klaus Eidmann, Jürgen Meyer-ter Vehn, and Klaus J Witte. Influence of the laser prepulse on proton acceleration in thin-foil experiments. *Physical review letters*, 93(4):045003, 2004. DOI: 10.1103/PhysRevLett.93.045003.

[201] P McKenna, DC Carroll, Olle Lundh, F Nürnberg, Keith Markey, S Bandyopadhyay, D Batani, RG Evans, R Jafer, Saty Kar, et al. Effects of front surface plasma

expansion on proton acceleration in ultraintense laser irradiation of foil targets. *Laser and Particle Beams*, 26(4):591–596, 2008. DOI: 10.1017/S0263034608000657.

[202] Saurabh Kumar, Krishna Gopal, and Devki Nandan Gupta. Proton acceleration from overdense plasma target interacting with shaped laser pulses in the presence of preplasmas. *Plasma Physics and Controlled Fusion*, 61(8):085001, 2019. DOI: 10.1088/1361-6587/ab216e.

[203] Julien Ferri, Evangelos Siminos, and Tünde Fülöp. Enhanced target normal sheath acceleration using colliding laser pulses. *Communications Physics*, 2(1):40, 2019. DOI: 10.1038/s42005-019-0140-x.

[204] Leonida A Gizzi, Elisabetta Boella, Luca Labate, Federica Baffigi, Pablo J Bilbao, Fernando Brandi, Gabriele Cristoforetti, Alberto Fazzi, Lorenzo Fulgentini, Dario Giove, et al. Enhanced laser-driven proton acceleration via improved fast electron heating in a controlled pre-plasma. *Scientific reports*, 11(1):13728, 2021. DOI: 10.1038/s41598-021-93011-3.

[205] Ying Gao, Pengjie Wang, Bin Liu, Shirui Xu, Shiyou Chen, Yinren Shou, Jianbo Liu, Zhusong Mei, Zhengxuan Cao, Tianqi Xu, et al. All-optical method for generating transient microstructured targets in laser ion acceleration. *Physical Review Research*, 6(4):L042031, 2024. DOI: 10.1103/PhysRevResearch.6.L042031.

[206] S Buffechoux, J Psikal, M Nakatsutsumi, L Romagnani, A Andreev, K Zeil, M Amin, P Antici, T Burris-Mog, A Compant-La-Fontaine, et al. Hot electrons transverse refluxing in ultraintense laser-solid interactions. *Physical review letters*, 105(1):015005, 2010. DOI: 10.1103/PhysRevLett.105.015005.

[207] Andreas Döpp, Christoph Eberle, Sunny Howard, Faran Irshad, Jinpu Lin, and Matthew Streeter. Data-driven science and machine learning methods in laser-plasma physics. *High Power Laser Science and Engineering*, 11:e55, 2023. DOI: 10.1017/hpl.2023.47.

Acknowledgments

As I pen these words, countless thoughts and emotions fill my heart—gratitude, joy, and nostalgia, but I find it difficult to put them all into words! Looking back, every step I have taken has been meaningful, and every experience has shaped this journey. This dissertation is not only the culmination of my research and efforts over the past few years but also a testament to the unwavering support and encouragement I have received from my supervisor, colleagues, collaborators, friends, and loved ones. I extend my heartfelt thanks to each of them!

First and foremost, I want to express my deepest gratitude to my supervisor, **Prof. Dr. Jörg Schreiber**. His unwavering support, patient guidance, and inspiring mentorship have been instrumental in every step of my PhD journey. His vast knowledge and encouragement helped shape this research and my growth as a scientist. As the Chinese saying goes, "Once a teacher, always a father." Being far from home, I will always remember and appreciate the warmth and care he extended to me, far beyond the academic realm.

I am sincerely thankful to **Prof. Dr. Jianhui Bin** for serving as the second referee of my PhD thesis. His thoughtful discussions and genuine support were invaluable to me. I deeply appreciate his kindness and am glad for the friendship we've built over these years.

I want to thank **Prof. Dr. Bernhard Mayer**, **Prof. Dr. Armin Scrinzi**, **Prof. Dr. Joachim Rädler** and **Prof. Dr. Jochen Weller** for their kindness and willingness to serve on my defense committee.

I owe a huge debt of gratitude to my colleagues in our research group for their camaraderie, encouragement, and hard work. My heartfelt thanks go to **Michael Bachhammer**, **Lenny Doyle**, **Ina Hofrichter**, **Julia Liese**, **Timo Pohle**, **Alexander Praßelsperger**, **Anna-Katharina Schmidt**, **Florian Schweiger**, and **Vignesh Vaidyanathan**. The long hours we spent during laser beamtimes together became some of the most unforgettable moments of my PhD. I am especially grateful to **Lenny Doyle** for his expertise and generous support, whether in optics, electronics, or software, and to **Michael Bachhammer** for taking over and maintaining the water-leaf target system so reliably. Sharing this journey with such talented and dedicated people has been an incredibly enriching experience.

To the former members of AG Schreiber, including **Dr. Masoud Afshari**, **Dr. Flex Balling**, **Dr. Ying Gao**, **Dr. Johannes Gebhard**, **Dr. Sonja Gerlach**, **Dr. Jens Hartmann**, **Dr. Thomas Rösch**, and **Dr. Martin Speicher**, I am profoundly grateful. I particularly thank **Dr. Masoud Afshari** for introducing me to PIC simulation, and **Dr. Ying Gao** for guiding me during my first steps in the group. I would also like to thank **Dr. Thomas Rösch** for his valuable input and encouragement and **Dr. Flex Balling** and **Dr. Sonja Gerlach** for patiently teaching me how to operate the laser system. Flex's advice during my defense preparation was especially appreciated.

I am thankful to my colleagues in the HF group: **Laura Geulig**, **Max Weiser**, and **Erin Grace Fitzpatrick**, and, of course, **Prof. Dr. Peter Thirolf**. Their engaging discussions helped expand my perspective and introduced me to ideas beyond my immediate field of research.

I am also grateful to the team around **Prof. Dr. Stefan Karsch** and **Dr. Andreas Döpp**, especially **Dr. Jinpu Lin**, **Dr. Moritz Foerster**, **Dr. Mathias Krüger**, and **Dr. Katinka von Grafenstein**, for their help with laser-related questions. A special thanks goes to **Nikolce Gjotev** and **Oliver Gosau**, who were always there to assist with vacuum systems and optics, and to **Florian Saran** and **Dr. Hans-Friedrich Wirth**, whose tireless efforts keep the CALA facility running. I am deeply thankful to our "laser god," **Gregor Schilling**, for his support and for always being available when I needed help. My gratitude also extends to **Rolf Öhm** and the mechanical workshop for their precision in crafting prototypes, as well as the engineering design group, **Dr. Johannes Wulz**, **Klaus Wirgler**, and **Christoph Rahm**, for their expertise in CAD design. Special thanks to **Katharina Adler**, **Dr. Martin L. Groß**, and the accounting team for their administrative support.

My sincere appreciation also goes to the members of the Medical Physics Chair under **Prof. Dr. Katia Parodi** for their fruitful collaboration, in particular **Prof. Dr. Marco Riboldi**, **Dr. Jona Bortfeld**, **Dr. Felix Rauscher**, **Romy Knab**, **Andrea Leinthaler**, **Petra Glier**, and **Eileen Helm**.

To my collaborators, I am truly thankful for your contributions and insights. My thanks go to **Dr. Shubhadeep Biswas** and **Prof. Dr. Matthias Kling** for offering me the opportunity to begin this journey, and to **Dr. Massimo De Marco** and **Dr. Mikheil Kharbedia** for their outstanding collaboration and dedication. I also deeply appreciate the discussions and shared knowledge with **Prof. Dr. Enam Chowdhury**, **Dr. Pilar Puyuelo-Valdes**, **Prof. Dr. Giancarlo Gatti**, **Prof. Dr. Gabriel Schaumann**, **Dr. Zhengxuan Cao**, **Prof. Dr. Wenjun Ma**, and **Zhuojie Sui**.

I am deeply grateful for all the shared work, enlightening discussions, and joyful moments with my Chinese friends, **Chenying Liu**, **Sining Chen**, **Fan Fan**, **Huihui Tao**, and **Xiang Chen**. These memories will remain with me forever. I also want to extend my heartfelt thanks to all the friends who crossed my path, even if I cannot mention everyone individually here. It was truly a wonderful time filled with laughter, friendship, and unforgettable experiences.

Last, but not least, I owe everything to my family for their unwavering love, encouragement, and support. To my parents and sister, your belief in me has carried me through every challenge. And to my dearest **Zhuojie Sui**, your constant encouragement and strength have been my anchor. Thank you for being by my side through every high and low of this journey.